HIGH TO ULTRA-HIGH TEMPERATURE CONTACT METAMORPHISM AND DRY PARTIAL MELTING OF THE TASIUYAK PARAGNEISS, NORTHERN LABRADOR: A PETROGRAPHIC, THERMOBAROMETRIC AND PHASE EQUILIBRIA MODELING STUDY

RHEA KATHERINE MITCHELL

High to Ultra-high Temperature Contact Metamorphism and Dry Partial Melting of the Tasiuyak Paragneiss, Northern Labrador:

A Petrographic, Thermobarometric and Phase Equilibria Modeling Study

by

© Rhea Katherine Mitchell, B.Sc.

A thesis submitted to the School of Graduate Studies
in partial fulfilment of the requirements for
the degree of Master of Science

Department of Earth Science
Memorial University
St. John's, Newfoundland and Labrador

September 2011

ABSTRACT:

Contact aureoles of the anorthositic to granitic plutons of the Mesoproterozoic Nain Plutonic Suite, Labrador, are particularly well developed in the Paleoproterozoic, regionally metamorphosed, granulite-facies, migmatitic Tasiuyak paragneiss. Regional metamorphism formed the assemblage Qtz–Kfs–Pl–Grt–Sil±Bt±Liquid. Phase equilibria modeling yields a minimum peak of 8.3 kbars and 852°C for this event, consistent with the conditions necessary for biotite dehydration melting. These rocks underwent a significant melt loss event(s), removing much of the hydrous material, leaving behind relatively dry compositions. Rocks within the contact aureoles were statically overprinted by lower P, but higher T mineral assemblages and by textures related to a second partial melting event. Samples collected within multiple contact aureoles, near Anaktalik Brook, west of Nain, Labrador are categorized into five main sample types based on textures and mineralogy: A: Spl–Crd domains (Sil pseudomorphs) and Opx–Crd (Grt pseudomorphs) within a quartzofeldspathic domain, B: interwoven Pl-rich and Crd-rich domains with Spl–Crd and Opx–Crd regions, similar to type A samples, C: complex arrangements of Spl–Crd domains, rounded Pl–Crd domains, interstitial Pl–Opx domains, very fine-grained intergrowths of Ksp–Qtz–Crd–Opx (Osm pseudomorphs) and coarse-grained domains of Ksp–Qtz–Crd–Opx (neosome), D: Sil-rich and Fa-rich (Grt pseudomorphs) domains within quartzofeldspathic matrix, and E: garnetiferous domains (Opx or Grt pseudomorphs), amoeboid Spl-Pl domains (Sil pseudomorphs) and coarse-grained Ksp–Qtz–Opx domains enclosed in a quartzofeldspathic matrix. Type A and C samples contain a very fine- to medium-grained geometric intergrowth of Crd–Qtz interpreted to have formed during melt-production during the dissolution of Bt and feldspars in the presence of melt. Evidence for partial melting includes: (i) lobate Ksp and Qtz pseudomorphs after former melt films and pockets (locally enclosing euhedral, idiomorphic cordierite) within and around plagioclase grains exhibiting corrosion along contact with films; (ii) in-filling of fractures in Ksp by Pl, Pl–Qtz symplectites and Qtz; (iii) thin films of Ab-rich Pl on matrix Pl; and (iv) Bt–Qtz symplectic rims around Bt coronae around Ilm. The formation of textures and minerals during the contact metamorphism was controlled by the textures and mineralogy of the regional metamorphic assemblage. UHT conditions are supported by: (i) >900°C high P/T gradient solidus estimated for all samples, coupled with extensive textural evidence for contact-related partial melting (ii) pseudomorphs after the UHT mineral osumilite, (iii) Ti–in–Qtz thermobarometry indicating contact metamorphism at temperatures of at least 700-980°C, (iv) high Al orthopyroxenes, (v) Zn- and Cr- bearing spinel and other common UHT textures involving Spl, Qtz, Crd, Opx and/or Crn locally replacing Grt or Sil).

ACKNOWLEDGEMENTS:

This work was supported by NSERC through grants supplied to Dr. Aphrodite Indares. I would like to thank my advisors Dr. Aphrodite Indares and Mr. Bruce Ryan for their encouragement, lively discussion and support throughout this project. I would like to thank Bruce Ryan for the collection of the sample set which made this project possible and for taking care of these beautiful rocks for 25 years. Thank you to those who assisted me in all of my analytical work; Mike Schaffer at Memorial University for his help during my SEM work and Peter Jones for his help during electron microprobe work at Carleton University. Thank you to my fabulous office mate, sounding board and friend, Stephanie Lasalle, for her hours of good conversation, good ideas, THERMOCALC troubleshooting and belief in me. Thank you to my friends and family who have always supported and believed in me from the beginning and who were always there to make me smile or to listen to my jargon-filled science-y frustrations. I would like to also thank Chad Lundrigan for keeping me strong, sane and motivated from the beginning.

TABLE OF CONTENTS

CHAPTER 5: PHASE EQUILIBRIA MODELING

LIST OF FIGURES

LIST OF TABLES

LIST OF ABBREVATIONS

Mineral Names (after Kretz 1983)

Bt	Biotite
Crd	Cordierite
Crn	Corundum
Fa	Fayalite
Gr	Graphite
Grt	Garnet
Ilm	Ilmenite
Ksp	K-feldspar
Ms	Muscovite
Oam	Orthoamphibole
Opx	Orthopyroxene
Osm	Osumilite
Pl	Plagioclase
Po	Pyrrhotite
Qtz	Quartz
Sil	Sillimanite
Spl	Spinel

Mineral Chemistry

X_{An}	Molar fraction of anorthite
X_{Ab}	Molar fraction of albite
X_{Kfs}	Molar fraction of K-feldspar
X_{Fs}	Molar fraction of ferrosilite
X_{Alm}	Molar fraction of almandine
X_{Grs}	Molar fraction of grossular
X_{Prp}	Molar fraction of pyrope
X_{Sps}	Molar fraction of spessartine
X_{Fe}	Fe/(Fe+Mg)
X_{Mg}	Mg/(Fe + Mg)
$X^{qtz}{}_{Ti}$	Molar fraction of Ti in Quartz
a_{TiO_2}	Activity of Ti in the system

Terminology

Very fine-grained	<50 μm
Fine-grained	51–100 μm
Medium-grained	0.1–2.0 mm
Coarse-grained	>2.0 mm

CHAPTER 1: INTRODUCTION

1.1 General Background and Aim of Thesis

Contact aureoles of the anorthositic to granitic plutons of the Mesoproterozoic Nain Plutonic Suite (NPS), located in northern Labrador, are particularly well developed in the Paleoproterozoic, regionally metamorphosed, granulite-facies, migmatitic Tasiuyak paragneiss. These contact aureoles represent a rare case of a polymetamorphic environment which has twice reached granulite-facies conditions and partial melting. Regional metamorphism took place during the development of the Torngat orogeny ca. 1.8 Ga (Bertrand *et al.,* 1993) during which pelitic rocks developed the assemblage Bt + Sil + Qtz + Pl + Grt + Ksp ± Liquid (Tettelaar & Indares, 2007; mineral abbreviations after Kretz, 1983). These rocks underwent significant melt loss, leaving behind H_2O-depleted, relatively dry, bulk compositions.

Contact metamorphism related to the intrusion of the NPS, ca. 1.3 Ga (Ryan, 2000), affected those rocks which were adjacent to the intrusions and led to the progressive transformation of garnet and sillimanite porphyroblasts to Opx–Crd and Spl–Crd, respectively (Berg, 1977a; Lee, 1987; MacFarlane *et al.,* 2003; Tettelaar, 2004). In addition, Tettelaar and Indares (2007) observed scarce, fine scale microstructures, such as pools and thin films of quartz found at triple junctions between feldspars and grain boundaries between cordierite, orthopyroxene and/or K-feldspar, which they attributed to partial melting during the contact metamorphism. The most texturally complex rocks in these aureoles contain the ultra-high temperature mineral osumilite variably replaced by intergrowths of Crd–Qtz–Ksp-Opx (Berg & Wheeler, 1976).

The presence of osumilite in the aureoles suggests that contact metamorphism reached particularly high temperatures. Osumilite, or osumilite pseudomorphs, are rare with only a small handful documented worldwide (e.g. Berg & Wheeler, 1976; Ellis *et al.,* 1980; Motoyoshi *et al.,* 1993; Westphal *et al.,* 2003; Sajeev & Osanai, 2004). Also, UHT metamorphism is most commonly observed in regional metamorphic terranes, with rarer examples in mantle xenoliths and contact aureoles (Kelsey, 2008). High metamorphic temperatures in the aureoles, in this case, are also supported by the local evidence for partial melting of the Tasiuyak paragneiss, because this unit was previously dehydrated by melt loss during the regional metamorphism. Therefore, the aureoles of the NPS display a rare combination of features: UHT metamorphic minerals formed during contact metamorphism and relatively dry partial melting. In addition they display complex microstructures resulting from the development of contact metamorphic mineral associations in specific microdomains controlled by coarse-grained and dry regional metamorphic assemblages.

In a region located near the Anaktalik Brook (central eastern portion of the Torngat orogen, near Nain, Labrador), the Tasiuyak paragneiss is in direct contact with multiple intrusions of the NPS and displays a wide range of complex microstructures related to the contact metamorphism. The purpose of this thesis is to document these microstructures and to provide an interpretation in terms of:

(i) the role of the precursor regional assemblage on their development;

(ii) partial melting; and

(iii) the ranges of temperature conditions during contact metamorphism.

This will be achieved by means of:

(i) a detailed examination of the microstructures with special attention to those related to partial melting,

(ii) application of thermobarometry,

(iii) and phase equilibria modeling.

1.2 Structure of Thesis

This thesis is organized into six chapters. The introductory chapter, Chapter 1, includes the aim of the thesis (Section 1.1), regional geology (Section 1.3), a review of the previous work done in the area (Section 1.3), an outline of the study area (Section 1.4), relevant theoretical background (Section 1.5) and a discussion on the approach and analytical methods used (Section 1.6). Chapter 2 focuses on the petrography, mineral chemistry and bulk compositions for seven contact metamorphosed samples, organized into five sample types. Chapter 3 discusses the interpretations of the observations made in Chapter 2. Chapter 4 covers the two methods of thermobarometry used in this study: titanium in quartz and Grt–Opx thermobarometry. Chapter 5 covers phase equilibria modeling of both only regionally metamorphosed rocks and contact metamorphosed samples. Discussions and conclusions are covered in Chapter 6.

1.3 Regional Geology

The region surrounding Nain, Labrador (see Figure 1-1) is composed of three tectonostratigraphic components: the Archean Nain Craton (part of the larger North Atlantic craton as defined by Bridgwater *et al.* (1973), the Archean to Paleoproterozoic Churchill province and the Mesoproterozoic NPS. The following geological framework is taken from Wardle *et al.* (2002), to which the reader is referred for more details. The Nain North Atlantic craton is bounded to the west by the Torngat orogen, part of the Paleoproterozoic Churchill Province, to the north by the Paleoproterozoic Nagssugtoquidian orogen in Greenland, to the south by the Paleoproterozoic Makkovik-Ketilidian orogen and Mesoproterozoic Grenville orogen. The Nain craton consists of 3.8–2.8 Ga upper amphibolite to granulite facies gneisses which were intruded by mafic dyke swarms between 2.2 and 2.0 Ga and by anorthosite-granite suites from 2.1 to 2.0 Ga. The youngest rocks in the Nain craton are a series of small A-type granite plutons intruded between 1.76 and 1.74 Ga. Overlying sedimentary rocks are Paleoproterozoic in age and show upward progression from shallow to deep water environments.

The Churchill province comprises a core zone bounded to the west by the Paleoproterozoic New Quebec orogen and to the east by the Torngat orogen. It is truncated to the south by the Mesoproterozoic Grenville Province and is correlated to the north with the Proterozoic Trans-Hudson orogen (Whitmeyer & Karlstrom, 2007) see Figure 1-1). It is composed of primarily 2.7-2.6 Ga (locally 3.0 Ga in the northeast) tonalitic to granitic gneisses. Rocks in the Churchill province show evidence for Archean metamorphism and partial melting, which was later overprinted by Paleoproterozoic, amphibolite to granulite facies metamorphism. Two large batholiths along the western margin of the Churchill province were intruded between 1.84 and 1.81 Ga and represent possible magmatic arc rocks.

The Nain, Superior and Rae-Hearne cratons were amalgamated at ~1.87 Ga, producing the Torngat orogen. The Torngat orogen (see Figure 1-1) is a narrow, N-S trending doubly-vergent belt composed of metasedimentary and magmatic arc rocks which underwent granulite facies metamorphism as a result of the collision of the Churchill province and the Nain craton. Later transpressional motion and continued granulite facies metamorphism was focussed along the sinistral Abloviak shear zone between 1.845 and 1.820 Ga. A second shear zone, the Komaktorvik shear zone along the eastern margin of the Torngat orogen, was activated between 1.80 and 1.74 Ga and was coeval with retrograde metamorphism. The Tasiuyak domain makes up most of the exposed Torngat orogen and is composed predominately of the Tasiuyak gneiss. The Tasiuyak gneiss is defined by alternating layers of Grt-rich leucogranite and Grt–Sil–Bt–Gr pelitic gneiss, which show evidence for extensive partial melting. The protolith of the Tasiuyak gneiss is most likely a shale-greywacke sequence with a depositional age of, at most, 1.94 Ga. The Tasiuyak domain is thought to be derived from an accretionary prism; however, it is still uncertain whether it originated from the Churchill or the Nain margin.

The NPS was emplaced into the Torngat Orogen, west of Nain between 1.35 and 1.29 Ga and comprises a roughly 20 000 km^2 area of mid- to upper-crustal anorogenic intrusive igneous rocks ranging from granitic, anorthositic, dioritic to troctolitic in composition (see Figure1-2; Ryan, 2000). Monzonite, leuconorite, gabbro and gabbronorite (ferrodiorite) also occur in minor volumes (Ryan, 2000). The NPS is thought to have formed in a crustal extensional setting, perhaps as the result of mantle upwelling which led to continuous replenishment of a mafic magma pond at the crust-mantle interface (Emslie *et al.,* 1994; Ashwal, 1993; Ryan, 2000 and references therein). According to this interpretation, the magma pond provided enough heat to cause wholesale crustal anatexis resulting in dry granitic melts which buoyantly rose through the crust until cooling and crystallization occurred. Assimilation of depleted lower crustal material into the underlying magma pond is inferred to have promoted plagioclase saturation of the magma giving rise to buoyant anorthositic plutons that rose to the same crustal level as the earlier granitoid magmas. Residual dioritic melts were carried with the anorthositic material and separated during ascent. Troctolitic plutons are the result of rapid ascent of minor amounts of primitive mafic magma from the subcrustal reservoir (Emslie *et al.,* 1994). Regions intruded by several plutons are marked by multiple contact aureoles.

1.4 Previous Work

1.4.1 Regional Metamorphism

Regional studies of the Tasiuyak paragneiss distal from Nain (Rivers *et al.,* 1996; Ermanovics & van Kranendonk, 1998; see Figure 1-3) have indicated that metamorphism during development of the Torngat Orogen attained granulite facies conditions as the result of crustal overthickening brought about by thrusting and accretion. The following P–T conditions have also been reported for the regional metamorphism of the Tasiuyak paragneiss: 6–7kbar / 510–750ºC (Rivers *et al.,* 1996; Ermanovics & van Kranendonk, 1998) and 6–9kbar / 850–900ºC (Lee 1987).

However, the most comprehensive study of the regional assemblage, proximal to the study area was undertaken by Tettelaar (2004) and Tettelaar and Indares (2007) focussing on samples of the Tasiuyak paragneiss to the northwest and outside the contact aureoles of the Pearly Gates intrusion and the Tessiarsuyungoakh intrusion (see Fig 1-3).

Tettelaar and Indares (2007) observed a general mineral assemblage of Qtz–Kfs–Pl–Grt–Sil±Bt marked by coarse-grained quartz ribbons, garnet porphyroblasts, feldspar porphyroclasts and sillimanite prisms (which locally wrap garnet porphyroblasts) distributed within a biotite-bearing quartzofeldspathic matrix. Spinel locally occurs in quartz-absent regions in proximity to garnet, ilmenite and biotite and is wrapped by sillimanite. A foliation is defined by coarse sillimanite prisms and coarse quartz ribbons. Assemblages containing porphyroblastic cordierite, spinel and/or orthopyroxene have also been observed within the Tasiuyak paragneiss (Ryan, *personal communication*).

This assemblage and its microstructures are consistent with the stability field associated with the biotite dehydration melting reaction Bt + Sil + Pl + Qtz → Grt + Ksp + Liquid in the NaKFMASH system (Tettelaar & Indares, 2007). Locally, strong foliations and bent sillimanite prisms give evidence for extensive deformation during this metamorphic and anatectic event which would have resulted in extensive melt removal or redistribution (Tettelaar & Indares, 2007).

Previously mentioned studies which have used traditional thermobarometry methods only, did not take partial melting into account, and for the most part are not consistent with granulite facies metamorphism (e.g. Rivers *et al.,* 1996; Ermanovics & van Kranendonk, 1998). Tettelaar and Indares (2007) estimated a peak pressure and temperature of 8–10kbar and ~870°C using the GASP thermometer and the petrogenetic grid for anatectic metapelites of Spear *et al.* (1999) as a framework. This is not a rigorous estimation but, nevertheless, it is consistent with granulite-facies metamorphism and considers the effect of partial melting.

1.4.2 Contact Metamorphism

Contact aureoles produced around intrusions of the NPS range in width from a few meters to ~6km. Previous studies have focussed primarily on the aureoles surrounding the Tessiarsuyungoakh and the Makhavinekh Lake intrusions and in regions where there are no overlapping contact aureoles of different pluton affinity (Lee, 1987; McFarlane et al., 2003; Tettelaar & Indares, 2007; Ryan, 1991).

The first study of the NPS aureoles is that of Berg (1977a), who examined the Tasiuyak paragneiss, ironstones and ultramafic rocks. Within orthopyroxene and cordierite-bearing gneisses and granulites he observed Spl–Crd intergrowths rimmed by plagioclase, with these intergrowths locally forming coronae around sillimanite. However, Berg (1977a) did not observe any textural evidence for melt, which led to the conclusion of extremely low values of P_{H2O}. Berg (1977a) observed the UHT mineral osumilite coexisting with Crd–Opx–Ksp–Qtz–Pl–Gr–Po–Ilm and locally in symplectic intergrowths with quartz or orthopyroxene. In addition, Berg and Wiebe (1985) studied a ferro-aluminous gneissic xenolith within granite between anorthosite and gneisses, southeast of the present study area. This xenolith consists of Ol–Spl–Opx–Pl–Bt–Grt–Oam–Ilm–Po having alternating cordierite and feldspar-rich layers and Spl–Bt–Pl–Po–Ilm rich layers. Within this layering, ovoids containing Ol–Opx–Grt–Oam, interpreted as garnet pseudomorphs, occur. Lee (1987) and Ryan (1991) defined contact aureoles surrounding the Makhavinekh Lake Pluton (MLP) based on the presence of the static transformation of garnet and sillimanite to Opx–Crd and Spl–Crd, respectively, within the quartzofeldspathic matrix of the Tasiuyak paragneiss. This transformation progressed gradually towards the intrusion. Furthermore, Lee (1987) identified fayalitic olivine and Zn-rich spinel in some rocks of the aureole along the southern Makhavinekh Lake pluton. McFarlane *et al.* (2003) and Tettelaar and Indares (2007) reported similar garnet and sillimanite replacement textures in the aureoles of the MLP intrusion and Tessiarsuyungoakh monzonite intrusion (TI). Tettelaar and Indares (2007) also observed:

(a) xenomorphic pods of symplectic Crd–Pl and Crd–Ksp along feldspar-feldspar grain boundaries;

(b) progressive coarsening of the fine-grained quartzofeldspathic matrix of the regional assemblage; and

(c) recrystallization of quartz ribbons to coarse xenomorphic grains.

In addition, Tettelaar and Indares (2007) documented screens of paragneiss within the Tessiarsuyungoakh monzonite intrusion (TI), adjacent to the Pearly Gates anorthosite, but northwest of the current study area (see Figure 1-3), which are characterized by large corroded garnet enclosed by a sillimanite-absent, quartz-poor matrix having blocky spinel and coarse-grained biotite. Locally garnet is partially replaced, along rims and fractures, by symplectic Spl±Crd±Opx and is locally surrounded by a rim of orthopyroxene or symplectic Crd–Ksp. These rocks are interpreted as high-T, contact metamorphosed country-rock screens which cooled quickly along with the TI.

In both the most overprinted parts of the aureoles and in the screens, Tettelaar and Indares (2007) observed limited evidence of partial melting during the contact metamorphism, based on the following microstructures:

(i) pools of quartz enclosing remnant feldspars; and

(ii) thin films of quartz at grain boundaries and along triple junctions between feldspars, cordierite and/or orthopyroxene grains.

All studies of the Tasiuyak paragneiss in the contact aureoles show that the contact metamorphic assemblages are distributed in specific microdomains which are controlled by the precursor regional metamorphic assemblage. These microdomains are the result of the limited diffusion possible within the heterogeneous, coarse-grained microstructure of the relatively dry regional assemblage (protolith).

Temperature ranges across specific aureoles have been estimated as: 700–900°C (Grt–Opx thermometry based on Al solubility in Opx; McFarlane *et al.,* 2003); 600–760°C (Fe-Mg exchange thermometry, Lee 1987); 645–915°C (Fe-Mg exchange thermometry; Berg, 1977b). Pressure estimates of the contact metamorphism range from 3.5–5.5 kbars (Lee, 1987) to 3.7–6.6 kbars (Berg, 1977b) using thermobarometers involving garnet, cordierite, orthopyroxene and spinel.

1.5 Study Area

The study area is located 45km SSW of Nain, Labrador (see Figure 1-3) in the vicinity of Anaktalik Brook and Anaktalik Bay. The geology of the study area is shown in Figure 1-4. Six samples were collected within wedges of thermally metamorphosed granulite-facies Tasiuyak paragneiss between multiple intrusions of the NPS west-northwest of Anaktalik Bay (see Figure 1-4) and a seventh sample (DL-85-96) was collected proximal to ferrodiorite plutonic rocks of the Cabot Lake pluton, south of Makhavinekh Lake, ~25km south of Anaktalik Brook. In this area, the Tasiuyak paragneiss is bordered to the North by the foliated to massive Pearly Gates anorthosite pluton (see Tettelaar, 2004 for more information). To the east and south, the gneiss is bordered and enclosed by several different massive plutonic rocks: ferrodiorite, rapakivi granite of the Makhavinekh Lake pluton and an unnamed anorthosite to leuconorite pluton (B. Ryan, *personal communication, 2009*; Lee, 1987).

Within this region, but outside of the contact aureoles, the Tasiuyak paragneiss has been described by Lee (1987), McFarlane *et al* (2003) and Tettelaar (2004) as white to buff to brown weathering, migmatitic rocks with centimetre- to metre-scale layers derived from a metasedimentary protolith alternating with layers derived from leucogranitoid protolith of either *in situ* or external origin. Metasedimentary layers are generally rich in garnet, sillimanite, biotite, graphite and sulphides, as compared to adjacent leucogranitic layers. Locally, highly foliated metasedimentary diatexite with biotite-rich wisps, narrow folia and phenocrysts of K-feldspar are observed. The most thermally altered outcrops have rusty brown weathering and are locally sulphide- and graphite-bearing, somewhat friable gneiss with spots and discontinuous streaks of light- to dark- to greyish-blue cordierite (± spinel, ±orthopyroxene) within a granular orthopyroxene-bearing quartzofeldspathic matrix (B. Ryan, *personal communication, 2009*; see Figure 1-5).

1.6 Background Theory

1.6.1 Partial Melting of Pelitic Rocks

Partial melting of pelitic rocks occurs primarily as a result of hydrate-breakdown (or vapour-absent; mica-dehydration) melting, which requires the presence of a hydrous mineral phase such as muscovite and biotite and produces melts of granitic composition (Spear *et al.,* 1999; Brown, 2008). With increasing temperatures at pressures above ~3 kbars, muscovite breaks down first, most commonly by the low variance reaction Ms + Pl + Qtz → Ksp + Al_2SiO_5 + Liquid (see NaKFMASH P–T grid in Figure 1-6; Spear *et al.,* 1999). At pressures below ~3 kbars, the breakdown of muscovite produces H_2O, and thus does not contribute to partial melting (Spear *et al.,* 1999). At temperatures above those of the muscovite stability field, the dehydration melting reactions involve biotite. These reactions include multivariant reactions in the P–T fields III and IV of Figure 1-6, as well as univariant reactions (in the NaKFMASH system; for example see reactions 8 and 9 in Figure 1-6). For a given rock, the reaction(s) which will occur depending on the mineral assemblage and specific bulk compositions and therefore can be best represented by P–T pseudosections (see Chapter 5). Once biotite is eliminated, further melting involves anhydrous phases only (Ksp + Qtz ± Pl; dry melting; Spear *et al.,* 1999). In H_2O depleted rocks with no muscovite and little biotite, such as the Tasiuyak paragneiss prior to contact metamorphism, the dominant type of melting involves anhydrous minerals only and can occur only at high to ultra-high temperature conditions (Kelsey, 2008).

1.6.2 Microstructures Related to Partial Melting

Reactant minerals of partial melting reactions become rounded and corroded and melt films grow at the grain boundaries (Vernon, 2004). Syntectonic melting, during regional metamorphism, is localized in areas of low stress such as pressure shadows around porphyroblasts and locally melt filled cracks are present (Sawyer, 1999; Brown, 2008). As the degree of partial melting increases, small melt pockets and films begin to coalesce and eventually create pathways along which melt can percolate (Brown, 2008). Melt may be largely extracted from the site of formation, depending on the degree of partial melting, the pressure and deformation conditions, the permeability and porosity of the residual matrix and the viscosity of melt (Ribe, 1987; Brown, 2008). This removal of melt alters the bulk composition and H_2O content of the rock and can allow for preservation of the anhydrous mineral assemblages of the metamorphic peak by limiting the degree of retrogression (White & Powell, 2002). Preservation of the peak assemblage is dependent on the bulk composition, the diffusion rates between melt and residue, the number of melt loss events and the pressure-temperature conditions (White & Powell, 2002). If melt is entirely lost, the solid metamorphic assemblage of the thermal peak may be preserved, including any residual solid phases which were not eliminated by the prograde melting reactions (eg. quartz in quartz ribbons, sillimanite and in some cases plagioclase) and the key minerals produced during prograde melting reactions (eg. garnet, K-feldspar)

If cooling is rapid, fine scale melt films or inclusions may be quenched into glass, which, when analyzed, give directly the composition of the melt. Cooling is rarely fast enough, however, to quench large volumes of melt and part of the melt is commonly lost, making it difficult to obtain its true composition (White & Powell, 2002). In fact, because we are able to analyze only solid rocks, it is only possible to infer information about the melt based on the microstructures formed during the process of solidification of the melt that remained in the rock (Holness, 2008). The following review of these microstructures is taken from Holness (2008). These microstructures are a result of the nucleation and growth of solid phases and are primarily controlled by the time it takes the rock to cool and by the size of the pocket of melt. As mentioned above, the most rapidly cooled melt will form glass regardless of the size of the melt pool. This is typically only seen in crustal enclaves, xenoliths in volcanic rocks (buchites) and in some pyrometamorphic aureoles. As the cooling rate decreases and/or the size of the melt pockets increase, the solidification of melt changes from supercooled glass to finely crystalline material to a coarse crystalline aggregate. Commonly in rapidly cooled contact aureoles a fine granophyric intergrowth grows within melt films. As cooling rates decrease, this intergrowth texture becomes coarser (see Figure 1-7A, Holness & Sawyer, 2008; Holness, 2008). If the two components of the intergrowth nucleate entirely on pore-walls, highly irregular and cuspate grain boundaries will form (see Figure 1-7B; Holness & Sawyer, 2008; Holness, 2008). If the grain size of the solidifying material is equal to that of the melt film, a row of equigranular and equant grains will form, termed a 'string of beads' texture (see Figure 1-7C; Holness & Sawyer, 2008; Holness, 2008).

A variety of microstructures can form in rocks with slower cooling rates and in environments favouring the accumulation of melt into pockets, but specific microstructures primarily depend on the size of the pocket of melt. Larger microstructures such as granophyre and inclusion-filled oikocrysts can form in the larger melt pockets. Polycrystalline aggregates can form in thick melt films. In the case of the smallest pockets, melt may be pseudomorphed by a single crystal of the phase which has the greatest difficultly nucleating (see Figure 1-8). The mineral which forms the pseudomorph is commonly different than that comprising the pore walls and if the same mineral is formed it will be of a different chemical composition than that in the pore walls. It is important to note that the composition of this pseudomorph does not likely represent the composition of the last melt contained in that melt pocket (Holness & Sawyer, 2008). Different components of the last melt may occur as single crystal pseudomorphs throughout the rock at the grain scale, giving evidence of the movement and transfer of melt at the grain scale (Holness & Sawyer, 2008). An average of the compositions of different pseudomorphs at the centimeter scale can approximate the composition of the final melt (Holness & Sawyer, 2008).

Coarse granophyric intergrowths and pore wall overgrowths can form in slowly cooled rocks enclosing large melt pockets. As melt begins to crystallize, solidification of a certain phase, for example quartz, on pore walls of a residual grain is favoured. A second mineral, such as plagioclase, begins to grow simultaneously as crystallization progresses, forming a granophyric intergrowth between the two minerals. This is best seen using cathodoluminescence imaging to enhance the residual cores and overgrowths on the first mineral. Nucleation of small crystals within large pockets of melt may lead to the formation of euhedral idiomorphic crystals, similar to those seen in plutonic igneous rocks (Vernon, 2004). It is important to note that many of these fine-grained microstructures, such as melt films and granophyric intergrowths, are highly vulnerable to eradication during deformation. Therefore, relatively low-strain environments are the most likely to preserve the actual melt characteristics of rocks.

The nature and distribution of minerals within crystallized melt depends on the diffusion rates between the residue and the segregated melt (White & Powell, 2010). Diffusion of elements and volatiles, especially water, from the segregated melt into the residue promotes the crystallization of anhydrous quartzofeldspathic minerals within the leucosome and simultaneous hydration of the residue allowing for retrogression and re-growth of hydrous mineral phases (White & Powell, 2010). Retrogression of the residue still depends upon the degree of melt loss and the residue:melt at the initiation of cooling (White & Powell, 2010).

Once the melt has solidified, minerals progress towards textural equilibration. This is represented by an increase in the dihedral angles at the boundary between triple-grain junctions and pseudomorphed melt pockets (Holness *et al.,* 2011). This increase in dihedral angle is accommodated by a decrease in surface area resulting in grain size coarsening and rounding and smoothing of grain boundaries (Holness *et al*., 2011).

1.6.3 UHT Metamorphism

Ultra-high temperature (UHT) metamorphism is classified within the P–T space defined by temperatures greater than 900ºC and pressures below the 20ºC/km geothermal gradient (see Figure 1-9; Kelsey, 2008). There are more than forty locations in the world identified to have undergone UHT metamorphism in a variety of regional tectonic settings showing a strong correlation to supercontinent creation (Kelsey, 2008). UHT conditions have also rarely been observed in xenoliths and deep-seated contact metamorphic aureoles (Kelsey, 2008). Textures and mineral assemblages indicative of UHT conditions are best observed in high magnesian meta-pelites which are rare and may be derived from: evaporitic mudstones, high magnesian argillaceous rocks, metasomatic rocks, pelites mixed with evaporites or residual bulk compositions created by the removal of Si- and Fe-rich melt (Kelsey, 2008 and references therein).

There is a wide range of mineral assemblages indicative of UHT conditions. They are dependent on the protolith and for the purposes of this study, only pelitic compositions are considered. For a full listing of UHT mineral assemblages see Kelsey (2008).

Sapphirine + quartz assemblages represent the highest observed crustal temperature conditions of >1000–1050ºC and are typically isolated from each other by coronae of sillimanite and/or orthopyroxene (Kelsey, 2008). The most common mineral assemblage, appearing in >65% of UHT localities, is **Opx + Sil + Qtz** and is primarily stable at >8–9bars and >900ºC (Kelsey, 2008). Texturally this assemblage can occur as porphyroblasts to fine-grained intergrowths (Kelsey, 2008).

Osumilite is a rare UHT mineral which has been documented in few localities only including xenoliths and some deep-seated contact metamorphic terranes (Kelsey, 2008). It has a hexagonal crystal structure and general formula of $(K,Na)(Mg,Fe)_2(Al,Mg,Fe)_3(Si,Al)_{12}O_{30}$ (Carrington & Harley, 1995). Osumilite is stable in relatively anhydrous conditions and P–T conditions ranging from 0.8–10.7 kbars and >1000ºC (Carrington & Harley, 1995). There is a range of reactions inferred to produce osumilite; the most common include:

(1) Bt + Crd + Ksp = Osm + Opx + Liq;

(2) Crd + Opx + Ksp + Qtz = Grt + Osm + Liq (Carrington & Harley, 1995).

Osumilite is rarely preserved during cooling, due to its highly unstable nature at low temperatures. Generally, its former presence can only be inferred by a very fine-grained intergrowth of its breakdown products Crd + Ksp + Qtz + Opx (Carrington & Harley, 1995; Holland *et al.,* 1996). Samples of osumilite from the NPS aureole, provided by Prof. Jonathan Berg for the purposes of this study, show coronae of this very fine-grained intergrowth (see Figure 1-10). Chemical analyses of these samples, compared with analyses from the literature, are shown in Table 1-1 (Berg & Wheeler, 1976; Grew, 1982; Carrington & Harley, 1995).

Spinel + quartz assemblages are common amongst UHT terranes and can occur in many textural relationships (Kelsey, 2008). Other less common UHT mineral assemblages include **sapphirine-bearing assemblages** with cordierite, orthopyroxene, spinel, corundum, biotite and/or garnet (Kelsey, 2008). **Spl–Crd** intergrowths replacing sillimanite and **Opx–Crd** intergrowths replacing garnet are also indicative of UHT conditions, when in the presence of melt (Kelsey, 2008).

In addition, some minerals stable under UHT conditions have distinctive compositional ranges:

(i) orthopyroxene is characterized by high-Al contents (Kelsey, 2008);

(ii) feldspars in metapelites are of ternary compositions (>10 mol% albite and <90% potassic; Kelsey, 2008);

(iii) cordierite has a_{H2O} <0.08, a maximum H_2O content of 0.2 wt% and a CO_2 content of 0.5–1.05 wt% (Harley & Thompson, 2004); and

(iv) UHT spinel is mainly Zn- and Cr-bearing (Kelsey, 2008 and references therein).

1.6.4 Quantitative Determination of UHT Conditions

The use of traditional thermobarometry on UHT assemblages is problematic and typically underestimates temperatures because minerals tend to re-equilibrate during cooling from high temperatures, especially from granulite facies and above. The Ti-in-Qtz thermometer (TitaniQ) is more applicable to UHT assemblages because Ti is relatively immobile during cooling (Thomas *et al.* 2010, see Section 4.1 for further discussion). Similarly, the Al-in-Opx thermometer (Opx–Grt thermometer) is also rigorous for UHT assemblages because Al is relatively immobile (MacFarlane *et al.*, 2003, see Section 4.2 for further discussion).

Phase equilibria modeling of specific bulk rock compositions can be used to obtain P–T conditions and the stability fields of known mineral assemblages. Its use in UHT assemblages, however, has some limitations, because the rocks are typically heterogeneous and contain many disequilibrium textures such as coronae and symplectites (Kelsey, 2008). Effective estimates of P–T conditions for these rocks must thus use bulk compositions of specific microdomains interpreted to represent a single mineral reaction microstructure (Kelsey, 2008). The use of whole rock bulk compositions can still be used for general comparisons and observations of topologies; however, direct P–T conditions cannot be taken from such diagrams.

1.7 Approach and Analytical Methods

1.7.1 Approach

This research comprises three main components: detailed petrography, thermobarometry and phase equilibria modeling.

Detailed petrography involved:

(i) examination of samples with a petrographic microscope to make first-order observations to obtain mineralogy and millimetre to centimetre scale microstructures;

(ii) cathodoluminescence imaging to allow for clearer observation of fine scale, potentially melt-related microstructures by highlighting feldspathic minerals;

(iii) the production of mineral maps at the thin section scale using an SEM with MLA software to examine the distribution of microstructures, as well as to better differentiate the distribution of minerals which are colorless under the petrographic microscope (i.e. quartz, feldspars and cordierite); and

(iv) analysis of minerals with an electron microprobe to determine the ranges in composition of key minerals in specific textural settings and to estimate bulk compositions.

The information gathered using detailed petrography allowed for first-order interpretations of:

(a) textures and microstructures in terms of the role of the regional assemblage on the development of the contact mineral associations in specific microdomains;

(b) potential evidence for partial melting; and

(c) the extent of melt-related microstructures.

The second component involves the application of the Ti-in-Qtz and Al-in-Opx thermobarometers, using relevant mineral compositions, to constrain the range of the contact metamorphism.

Finally, phase equilibria modeling was used:

(i) to constrain the peak pressure and temperature conditions for the regional metamorphism using a P–T pseudosection calculated for a sample from Tettelaar and Indares (2007); the rationale for this is that the P–T conditions of the regional metamorphism in the vicinity of the study area were poorly constrained and this information is important in order to evaluate the protoliths involved in the contact metamorphism; and

(ii) to calculate P–T pseudosections for a range of bulk compositions of representative samples from the study area in order to:

a. evaluate the mineral assemblage that was stable at the peak of the regional metamorphism in the contact metamorphosed samples; and

b. compare the topologies within the high to ultra-high temperature-low pressure conditions of the contact metamorphism with the minerals and textures observed.

Topologies estimated using this method characterize equilibrium assemblages and cannot be directly related to disequilibrium assemblages observed in thin section and thus will only be compared to observe general similarities and trends.

Details of the analytical techniques used within these components are described below.

1.7.2 Scanning Electron Microscope (SEM) - Mineralogical Maps

Mineralogical maps were produced using Mineral Liberation Analysis (MLA) software (developed by JKTech, University of Queensland, Australia) in conjunction with the FEI Quanta 400 environmental scanning electron microscope operated by the Core Research Equipment and Instrument Training (CREAIT) Network at Memorial University of Newfoundland and Labrador. MLA software, using backscattered electron imaging as a measure of average atomic number, determines grain boundaries and employs user-defined X-ray spectra and collected X-ray spectra within each grain to define the identity of each grain within a thin section. Compilation of this information results in a mineralogical map at the thin section scale and an estimate of modal mineral percentages.

1.7.4 Electron Microprobe – Mineral Analyses

Quantitative analyses were carried out on an automated 4 spectrometer Cameca Camebax MBX electron probe running under Henderson automation by the wavelength dispersive X-ray analysis method (WDX) at Carleton University. Analytical methods and standards for the electron microprobe analysis are based on Jenkins and Devris (1970), Goldstein *et* *al* (1981), Ziebold (1967), Robinson (1998) and work done by Henderson Microbeam Services at the University of Michigan. Analyses were done using the following operating conditions: 20 kV accelerating potential and 20 nA beam current for silicate and oxide minerals. Feldspars were analyzed using a 10x10 micron rastered electron beam due to their sensitivity under a focussed beam. Elements were analyzed for peak counting times of 15–40 seconds or 40,000 accumulated counts. Background analysis was done at 50% peak counting time on either side of the analyzed peak. Raw X-ray data were converted to elemental weight percent by the Cameca PAP matrix correction program. The standards used were a collection of well characterized natural and synthetic material and compounds listed in Table 1-2. Analyses are accurate within 1–2 relative percent for major elements with >10 wt% and 3–10 relative percent for minor elements with >0.5 wt% to <10 wt%. For analyses approaching the detection limit (<0.1wt%), relative errors approach 100%. Appendix A gives the analyzed mineral compositions in wt %, mol % and numbers of cations per formula unit.

Titanium concentrations in quartz were used in the Titani-Q thermobarometer (Thomas *et al.,* 2010) to calculate temperatures of quartz crystallization in specific textural settings. Titanium concentration in quartz is typically on the order of parts per million and analyses were done under different analytical conditions in order to Optimize the estimate of titanium concentration. The operating conditions for these analyses were 15kV accelerating potential and 20 nA beam current. Titanium concentration in quartz was measured for peak counting times of 150 seconds, with background counting times of 75 seconds using three PET crystals simultaneously. The K-alpha quartz and TiO_2 standards were used. Standards SRM 610 and 612 were also analyzed for comparison of titanium analyses and were conducted with a beam rastered over ~15–20 microns. SRM 610 yielded 500 ppm titanium and was analyzed for 30 seconds counting time (with cited values up to 524 ppm in the literature). SRM 612 yielded 50 ppm titanium and was analyzed for the full 150 seconds (with cited values up to 57 ppm in the literature). The quartz standard is a pure quartz sample and yielded 0 ppm titanium. The distribution of Fe^{2+} and Fe^{3+} ions in iron-bearing minerals was calculated using the stoichiometric method of Droop (1987). The percentage of total iron as Fe^{3+} showed very low (<1%) and inconsistent results which most likely represent analytical error. The only mineral which showed consistent Fe^{3+} concentrations was spinel with ~7-12% total iron as Fe^{3+} across the entire sample set.

1.7.4 THERMOCALC – Phase Equilibria Modeling

Phase equilibria modeling for this study consisted of the calculation of P–T pseudosections using THERMOCALC, a thermodynamic calculation program (Holland & Powell, 1998). THERMOCALC uses known, user-input, bulk compositions of rocks and a set of internally consistent thermodynamic data sets to calculate P–T pseudosections of mineral stability fields and mineral isopleths for that specific bulk composition. P–T pseudosections were calculated using mineral data file tc-ds55 (Holland and Powell; created in November 2003) within the NCKFMASHTO system, within a pressure-temperature range of 700–1100°C and 3.5–12 kbars, using the following a-x models and abbreviations: biotite (bi: White *et al.,* 2007), silicate melt (liq:

White *et al.,* 2007), cordierite (cd: Holland *et al.,* 1998), garnet (g: White *et al.,* 2007), orthopyroxene (opx: White *et al.,* 2002), plagioclase (pl: Holland & Powell, 2003), K-feldspar (ksp: Holland & Powell, 2003), spinel (sp: White *et al.,* 2002), osumilite (osm: Holland *et al.,* 1996) and ilmenite (ilm: White *et al.,* 2000). Bulk compositions were calculated using modal percentages estimated from MLA mineral maps (see above) and average chemical compositions of minerals. Due to the lack of conventional methods to discern the Fe^{2+} and Fe^{3+} in ferrous minerals, an estimated oxygen value is added to the bulk composition to account for the analyzed Fe being assigned as Fe^{2+} (FeO) only. These rocks contain little magnetite and the main Fe^{3+} containing phase is spinel which is composed of primarily Fe^{2+}, with ~7-12% of total Fe as Fe^{3+} (see Appendix A for Fe^{3+} calculations). Using a range of oxygen values cited in the literature, a low value or 0.1 was chosen to represent the distribution of iron in these compositions. Similarly the proportion of H_2O in cordierite is difficult to determine. Based on experimental studies by Harley and Thompson (2004) of cordierite which have withstood high temperatures, a value of 0.1 molecules of H_2O per molecule of cordierite was used.

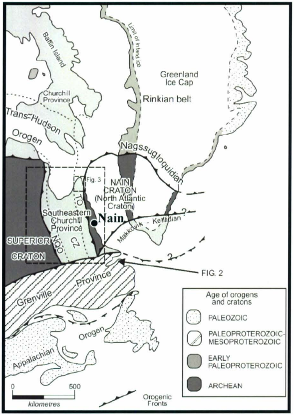

Figure 1-1. Regional geology of eastern Canada and adjacent Greenland (Wardle *et al.*, 2002). NQO: New Quebec Orogen; TO: Torngat Orogen; CZ: Core Zone.

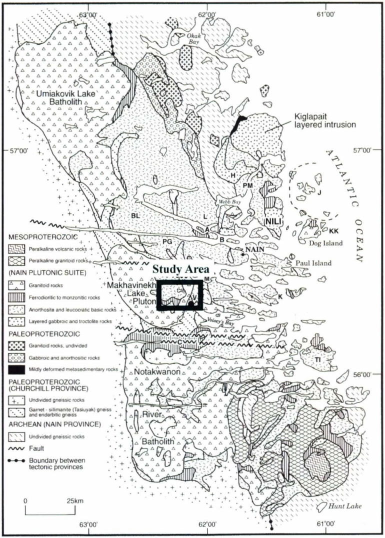

Figure 1-2. Geological map of the Nain Plutonic Suite (Ryan, 2000). Study area shown with black box. Anorthosite intrusions: BL: Bird Lake; K: Kikkertavak Island; Koliktalik Island; L: Mount Lister; PG: Pearly Gates; PM: Port Manvers Run and TI: Tunungayualok Island. Troctolitic intrusions: B: Barth Island; H: Hettasch; J: Jonathon; M: Mushuau; NILI: Newark Island and V: Voisey's Bay. Ferrodioritic intrusions: C: Cabot Lake and A: Akpaume intrusion.

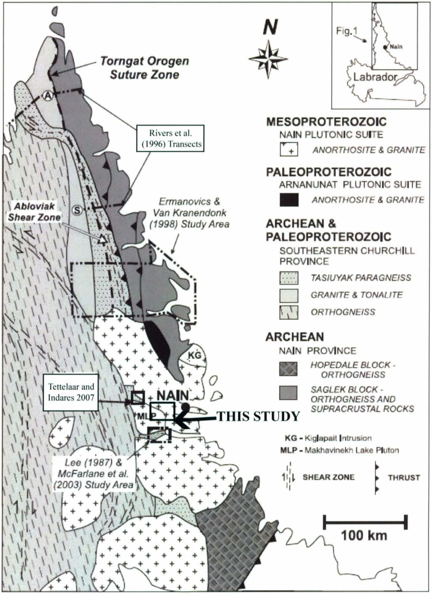

Figure 1-3. Regional geology of Northern Labrador showing locations of P-T studies (modified from Tettelaar & Indares, 2007)

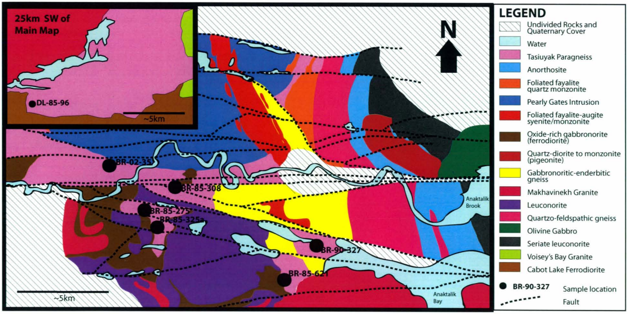

Figure 1-4. Study area showing sample localities in relation to local geology. Map based on Ryan and Lee (1989) and additional imformation supplied by B. Ryan, 2010.

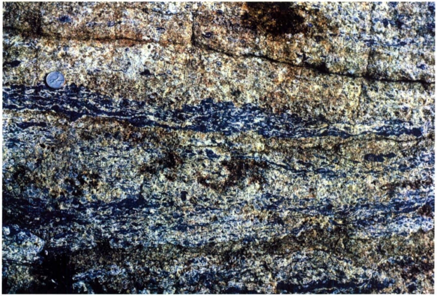

Figure 1-5. Field photograph of weathered outcrop of type C sample BR-85-275 showing streaks of dark blue cordierite-rich layers and light quartzofeldspathic layers. Located south of Anaktalik Brook. Photo by B.Ryan. See coin for scale.

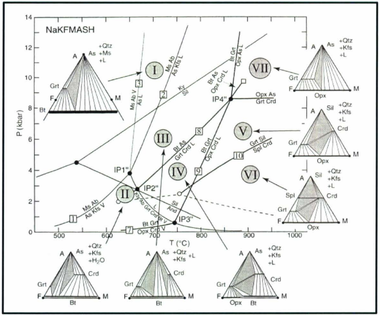

Figure 1-6. NaKFMASH Petrogenetic grid with AFM diagrams (Spear *et al.,* 1999).

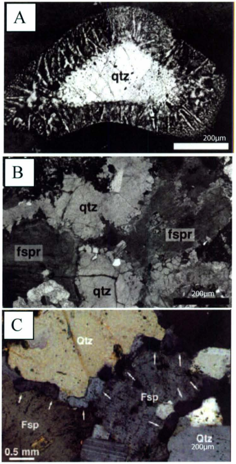

Figure 1-7. Melt solidification microstructures from Holness and Sawyer (2008; A and B) and Holness et al., 2011 (C). (a) Coarse granophyric rim separating Qtz and Ksp, (b) Highly cuspate and irregular boundary between Qtz and Fspr, (c) `String of Beads` texture.

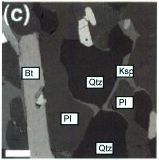

Figure 1-8. Back-scattered electron image of small melt films and pockets of Ksp between Qtz and Pl. Sample from Ashuanipi granulite-facies migmatite. Scale bar represents 50μm (Holness & Sawyer, 2008)

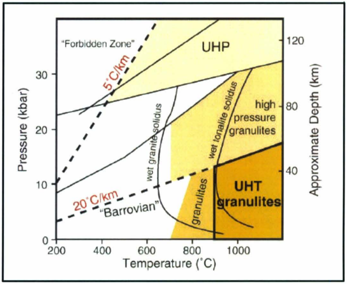

Figure 1-9. UHT metamorphism classification in P-T space (from Kelsey, 2008)

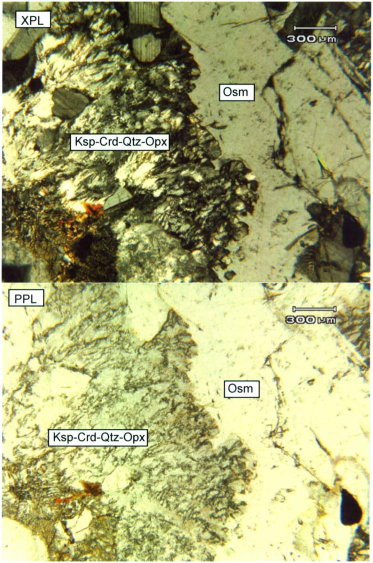

Figure 1-10. Photomicrographs of osumilite with corona of very fine grained intergrowth of Ksp-Crd-Qtz-Opx (sample Os1 from J. Berg).

Table 1-1. Osumilite composition data [Structural formula: $(K,Na)(Mg,Fe^{2+})_2(Al,Mg,Fe^{3+})_3(Si,Al)_{12}O_{30} = CA_2T2_3T1_{12}O_{30}$].

	This Study (sample supplied by J. Berg)					Carrington and Harley 1995									Berg and Wheeler 1976	Grew 1982	
Spot #	osm-os2-001	osm-os2-002	osm-os2-003	osm-os2-004	osm-os2 Ave	DG51-3a	DG51-3b	DG49-7	DG66-4	DG60-5a	DG60-5b	DG47-5	DG55-3	DG65-3	Nain-14	Ref. Peak, Antarctica	AVE
Weight %																	
SiO2	61.99	62.24	62.14	62.42	**62.20**	61.87	61.75	62.15	63.16	61.12	62.70	60.93	61.83	62.03	62.18	62.20	**62.05**
Al2O3	22.81	22.44	22.61	22.85	**22.68**	23.33	23.63	24.31	22.39	23.94	22.23	23.64	23.88	23.99	21.58	23.06	**23.11**
TiO2	0.11	0.12	0.11	0.14	**0.12**	0.00	0.00	0.00	0.00	0.00	0.00	0.00	0.00	0.00	0.00	0.00	**0.03**
FeO	6.10	6.27	6.25	6.12	**6.19**	4.66	3.60	1.48	1.44	3.85	1.91	3.32	1.31	1.00	3.97	0.45	**3.45**
MgO	5.76	5.74	5.73	5.81	**5.76**	6.26	6.91	7.89	8.41	6.35	8.42	6.99	8.27	8.43	7.46	9.29	**7.18**
MnO	0.11	0.07	0.10	0.08	**0.09**	0.00	0.00	0.00	0.00	0.00	0.00	0.00	0.00	0.00	0.00	0.00	**0.02**
ZnO	0.03	0.07	0.00	0.09	**0.05**	0.00	0.00	0.00	0.00	0.00	0.00	0.00	0.00	0.00	0.00	0.00	**0.01**
CaO	0.06	0.04	0.03	0.02	**0.04**	0.01	0.02	0.02	0.00	0.02	0.03	0.01	0.00	0.02	0.06	0.01	**0.02**
Na2O	0.32	0.36	0.30	0.37	**0.34**	0.04	0.04	0.04	0.00	0.05	0.03	0.04	0.04	0.00	0.22	0.29	**0.14**
K2O	4.34	4.19	4.26	4.23	**4.26**	4.29	4.28	4.32	4.50	4.30	4.54	4.30	4.33	4.37	4.12	4.34	**4.31**
BaO	0.18	0.33	0.28	0.24	**0.26**	0.00	0.00	0.00	0.00	0.00	0.00	0.00	0.00	0.00	0.00	0.00	**0.07**
Total	101.80	101.86	101.83	102.38	**101.97**	100.46	100.23	100.21	99.90	99.63	99.86	99.23	99.66	99.84	99.59	99.64	**100.41**
Mol %																	
SiO2	67.00	67.17	67.13	67.06	**67.09**	67.52	67.28	67.34	67.94	67.37	67.49	67.06	67.11	67.15	67.41	66.83	**67.25**
Al2O3	14.53	14.28	14.39	14.47	**14.42**	15.00	15.17	15.52	14.19	15.55	14.10	15.33	15.28	15.30	13.79	14.60	**14.75**
TiO2	0.09	0.09	0.09	0.11	**0.10**	0.00	0.00	0.00	0.00	0.00	0.00	0.00	0.00	0.00	0.00	0.00	**0.03**
FeO	5.51	5.66	5.65	5.50	**5.58**	4.25	3.28	1.34	1.30	3.55	1.72	3.06	1.19	0.91	3.60	0.40	**3.28**
MgO	9.28	9.23	9.22	9.30	**9.26**	10.18	11.22	12.75	13.49	10.43	13.51	11.47	13.38	13.60	12.06	14.88	**11.45**
MnO	0.10	0.06	0.10	0.07	**0.08**	0.00	0.00	0.00	0.00	0.00	0.00	0.00	0.00	0.00	0.00	0.00	**0.03**
ZnO	0.03	0.05	0.00	0.07	**0.04**	0.00	0.00	0.00	0.00	0.00	0.00	0.00	0.00	0.00	0.00	0.00	**0.01**
CaO	0.07	0.05	0.04	0.02	**0.04**	0.01	0.02	0.02	0.00	0.02	0.03	0.01	0.00	0.02	0.07	0.01	**0.03**
Na2O	0.33	0.38	0.32	0.39	**0.35**	0.04	0.04	0.04	0.00	0.05	0.03	0.04	0.04	0.00	0.23	0.30	**0.16**
K2O	2.99	2.89	2.94	2.90	**2.93**	2.99	2.97	2.99	3.09	3.02	3.12	3.02	3.00	3.02	2.85	2.97	**2.98**
BaO	0.08	0.14	0.12	0.10	**0.11**	0.00	0.00	0.00	0.00	0.00	0.00	0.00	0.00	0.00	0.00	0.00	**0.03**
Total	100.00	100.00	100.00	100.00	**100.00**	100.00	100.00	100.00	100.00	100.00	100.00	100.00	100.00	100.00	100.00	100.00	**100.00**
No. of Cations																	
Si	10.25	10.29	10.27	10.26	**10.27**	10.25	10.21	10.18	10.38	10.18	10.35	10.18	10.19	10.19	10.37	10.23	**10.25**
Al	4.45	4.37	4.41	4.43	**4.41**	4.56	4.61	4.69	4.34	4.70	4.32	4.65	4.64	4.64	4.24	4.47	**4.50**
Ti	0.01	0.01	0.01	0.02	**0.01**	0.00	0.00	0.00	0.00	0.00	0.00	0.00	0.00	0.00	0.00	0.00	**0.00**
Fe	0.84	0.87	0.86	0.84	**0.85**	0.64	0.50	0.20	0.20	0.54	0.26	0.46	0.18	0.14	0.55	0.06	**0.48**
Mg	1.42	1.41	1.41	1.42	**1.42**	1.55	1.70	1.93	2.06	1.58	2.07	1.75	2.03	2.06	1.86	2.28	**1.77**
Mn	0.01	0.01	0.01	0.01	**0.01**	0.00	0.00	0.00	0.00	0.00	0.00	0.00	0.00	0.00	0.00	0.00	**0.00**
Zn	0.00	0.01	0.00	0.01	**0.01**	0.00	0.00	0.00	0.00	0.00	0.00	0.00	0.00	0.00	0.00	0.00	**0.00**
Ca	0.01	0.01	0.01	0.00	**0.01**	0.00	0.00	0.00	0.00	0.00	0.00	0.00	0.00	0.00	0.01	0.00	**0.00**
Na	0.10	0.12	0.10	0.12	**0.11**	0.01	0.01	0.01	0.00	0.02	0.01	0.01	0.01	0.00	0.07	0.09	**0.05**
K	0.91	0.88	0.90	0.89	**0.90**	0.91	0.90	0.90	0.94	0.91	0.96	0.92	0.91	0.92	0.88	0.91	**0.91**
Ba	0.01	0.02	0.02	0.02	**0.02**	0.00	0.00	0.00	0.00	0.00	0.00	0.00	0.00	0.00	0.00	0.00	**0.00**
Total	18.03	18.01	18.01	18.01	**18.01**	17.93	17.94	17.93	17.92	17.93	17.98	17.96	17.96	17.95	17.98	18.04	**17.97**
X(Fe)	*0.37*	*0.38*	*0.38*	*0.37*	***0.38***	*0.29*	*0.23*	*0.10*	*0.09*	*0.25*	*0.11*	*0.21*	*0.08*	*0.06*	*0.23*	*0.03*	***0.21***
X(Mg)	*0.63*	*0.62*	*0.62*	*0.63*	***0.62***	*0.71*	*0.77*	*0.90*	*0.91*	*0.75*	*0.89*	*0.79*	*0.92*	*0.94*	*0.77*	*0.97*	***0.79***
Al(T1)	1.75	1.71	1.73	1.74	**1.73**	1.75	1.79	1.82	1.62	1.82	1.65	1.82	1.81	1.81	1.63	1.77	**1.75**
Al(T2)	2.69	2.67	2.68	2.69	**2.68**	2.81	2.82	2.88	2.72	2.88	2.67	2.83	2.82	2.83	2.61	2.70	**2.75**
C	1.02	1.00	1.00	1.01	**1.00**	0.92	0.92	0.92	0.94	0.93	0.97	0.93	0.92	0.92	0.95	1.00	**0.96**
A-T2	4.95	4.95	4.96	4.95	**4.95**	5.00	5.02	5.01	4.98	5.00	5.00	5.03	5.03	5.03	5.02	5.04	**5.00**
T1	12.00	12.00	12.00	12.00	**12.00**	12.00	12.00	12.00	12.00	12.00	12.00	12.00	12.00	12.00	12.00	12.00	**12.00**
TOTAL	17.97	17.95	17.95	17.96	**17.96**	17.92	17.94	17.92	17.92	17.93	17.97	17.96	17.96	17.95	17.97	18.04	**17.95**

*Samples analyzed in this study are of the same sample set as the samples analyzed in Berg and Wheeler (1978).

Table 1-2. Elemental standards used for microprobe analysis.

Element	Line	Standard
Si	KA	olivine
Al	KA	spinel syn.
Mg	KA	olivine
Na	KA	albite
K	KA	microcline USNM
Ca	KA	wollastonite
Ti	KA	MnTiO3 syn.
Cr	KA	Cr2O3 syn.
Mn	KA	MnTiO3 syn.
Fe	KA	fayalite syn.
Ni	KA	NiO syn.
Ba	LA	barite
Cl	KA	tugtupite
Fe	KA	lithium fluoride syn.
Zn	KA	gahnite USNM
Ti (in SiO2)	SRM	Glass samples 610: 41.7 - 524.4 ppm Ave: 403.0 ppm 612: 38.2 - 57.0 ppm Ave: 55 ppm

CHAPTER 2: PETROGRAPHY AND MINERAL CHEMISTRY OF THE CONTACT METAMORPHOSED SAMPLES

2.1 Petrography

2.1.1 Introduction

This study focuses on six samples from Tasiuyak paragneiss units, surrounded by plutons of the NPS, in the Anaktalik Brook area, just west of Nain, Labrador and a seventh sample located ~25km south of the Anaktalik Brook, proximal to the Cabot Lake ferrodiorite intrusion (see Figure 1-3). These samples consist of an assembly of textural domains with distinctive mineralogy and/or microstructures. In terms of the overall mineralogy and textural domains, the seven samples have been categorized into five main sample types. These types are described below in terms of their petrography and mineral chemistry. Absolute values of the ranges in size implied by the modifiers very fine-, fine-, medium- and coarse-grained are given in the List of Abbreviations on page *xi*. The petrography is summarized in Table 2-1. An interpretation of the different domains in these sample types is given in the following chapter.

2.1.2 Type A Samples

2.1.2.1 Petrography

Type A samples (BR-02-35 north of Anaktalik Brook, adjacent to Pearly Gates anorthosite and BR-90-327 west of Anaktalik Bay, proximal to a leuconorite intrusion and the Makhavinekh granite) are characterized by Opx–Crd (21–50 %), Spl–Crd (15–26

%) and quartzofeldspathic domains (35–50 %). These samples have a modal mineralogy of: cordierite 38–44%; plagioclase 23–29%; K-feldspar 14–24%; orthopyroxene 2–10%; quartz 1–4%; spinel 1–3%; ilmenite <1%; garnet <1%; biotite <1% (see Figures 2-1 and 2-2). Ilmenite and biotite are xenoblastic and medium-grained and observed in all textural domains. Minerals observed in trace amounts include: muscovite, chlorite, corundum, magnetite, graphite, zircon, pyrrhotite, monazite and pyrite.

The Opx–Crd domains are rounded and range in size from ~2–10 mm. They are composed of an Opx–Crd radial symplectite (see Figures 2-1A, 2-2A,B, 2-3A) with minor very fine-grained plagioclase and/or quartz and locally, relict corroded garnet at the core (see Figures 2-2B,C). In places, this domain is surrounded by a Crd–Pl symplectite (see Figure 2-1B) and in sample BR-90-327 one domain is entirely composed of this symplectite (Crd–Pl subdomain; see Figures 2-2C, 2-4A). These Opx–Crd domains, in sample BR-02-35, are surrounded by a medium to coarse-grained atoll of orthopyroxene and/or medium-grained plagioclase (see Figures 2-1A, 2-3B). This type of domain is locally flanked by medium to coarse-grained plagioclase and/or a Pl–Crd symplectite in sample BR-90-327 (see Figures 2-2B, 2-3A).

The Spl–Crd domains are abundant and aligned (BR-90-327, see Figure 2-2D) to scattered and irregular (BR-02-35, see Figure 2-1C) and range in size from 0.5 mm x 3.0 mm to 3.0 mm x 10 mm. These domains are composed of a Spl–Crd intergrowth within a corona of cordierite rimmed by medium-grained plagioclase (see Figures 2-1C, 2-2D, 2-3C). Locally, spinel is partially replaced by corundum.

The quartzofeldspathic domains in BR-90-327 form a network (matrix) enclosing other domains. They are composed primarily of perthitic K-feldspar and fine-grained quartz and are rimmed by medium to coarse-grained plagioclase with minor medium-grained orthopyroxene (see Figure 2-2E). These quartzofeldspathic domains, in BR-90-327, also locally include an isolated domain of coarse orthopyroxene and quartz with minor chlorite and graphite (see Figures 2-2F, 2-4B). The quartzofeldspathic domains in BR-02-35 separate the other domains and are mainly composed of coarse quartz and perthitic K-feldspar as well as minor medium-grained orthopyroxene, cordierite and plagioclase (see Figure 2-1D). They also contain:

(a) medium-grained geometric Crd–Qtz intergrowth rimmed by corroded feldspars and minor orthopyroxene (see Figures 2-1E, 2-5); and

(b) a quartzofeldspathic region of corroded plagioclase and K-feldspar in a coarse matrix (see Figures 2-1F, 2-4C).

In addition, the quartzofeldspathic domains host fine scale microstructures which are absent elsewhere. These include the following:

(c) xenomorphic, lobate, interstitial pockets of primarily K-feldspar (locally quartz or plagioclase) ranging in size from <1mm to ~5mm. These pockets occur at grain boundaries and triple junctions between plagioclase grains which are rounded against K-feldspar (see Figure 2-6A,C);

(d) pods and cracks in-filled with a very fine-grained Pl–Qtz symplectite and/or plagioclase and/or quartz between and within coarse-grained perthitic K-feldspar, as well as Pl–Qtz symplectite rims on plagioclase (see Figure 2-6B);

(e) euhedral cordierite surrounded by a film of K-feldspar, near and as inclusions in plagioclase grains which are rounded against K-feldspar (see Figure 2-6D); and

(f) thin partial films of an albite-rich plagioclase (see Figure 2-7) or ternary feldspar along plagioclase grain boundaries with K-feldspar and cordierite, respectively.

2.1.2.2 Mineral Chemistry

Ranges in mineral composition in specific textural settings are shown in Tables 2-2 to 2-5. **Plagioclase** has $X_{An} = 0.32–0.44$, $X_{Ab} = 0.54–0.70$ and $X_{Or} = 0.01–0.05$ and is generally An-rich in sample BR-90-327 relative to sample BR-02-35. Plagioclase in both samples show a slight (<0.02) decrease in X_{An} toward the rounded rims. In specific textural settings the composition of plagioclase covers a narrow range and in each sample these ranges overlap, with the exception of an Ab-rich plagioclase (in contact with K-feldspar) and ternary feldspar (in contact with cordierite) in fine-grained rims on rounded plagioclase grains within the quartzofeldspathic matrix (see Table 2-2).

K-feldspar compositions range from ternary to orthoclase depending on textural setting and have an overall range of $X_{Or} = 0.70–0.97$, $X_{Ab} = 0.03–0.28$ and $X_{An} = 0.00–0.08$ (see

Table 2-3). K-feldspar within the quartzofeldspathic domains in both samples and within the isolated coarse-grained domain in BR-90-327 is ternary feldspar, whereas K-feldspar within the medium-grained quartzofeldspathic region in BR-02-35 is orthoclase. Xenomorphic pockets of K-feldspar range from orthoclase to ternary feldspar with increasing size of pocket.

Cordierite has X_{Fe}= 0.37–0.44 and shows narrow ranges in composition in specific textural settings (see Table 2-4). In general, cordierite has lower X_{Fe} in the Opx–Crd and Spl–Crd domains relative to the cordierite rimming those domains and within the matrix. This trend is more obvious in sample BR-02-35.

Orthopyroxene is hypersthene with X_{Fs} = 0.59–0.64 and Al_2O_3 = 2.09–3.67 mol% (see Table 2-5). In general, X_{Fs} in orthopyroxene is highest in the Opx–Crd domains.

Spinel is generally homogeneous with X_{Fe} = 0.86–0.87, ZnO = 0.71–1.13 mol%, Cr_2O_3 = 0.20–0.83 mol%, MnO = 0.18–0.26 mol% and TiO_2 = 0.09–0.47 mol%. TiO_2 values decrease in the core of Spl–Crd domains.

Garnet compositions depend upon the textural setting. Garnet occurring in the cores of the Opx–Crd domains has X_{Alm} = 0.55–0.64, X_{Prp} = 0.34–0.44, X_{Grs} = 0.00–0.02 and X_{Sps} = ~0.01. In contrast, garnet in the cores of the Pl–Crd symplectites has X_{Alm} = ~0.76, X_{Prp} = ~0.19, X_{Grs} = ~0.03 and X_{Sps} = ~0.02.

2.1.3 Type B Samples

2.1.3.1 Petrography

Type B, represented by sample BR-85-308, from south of Anaktalik Brook, adjacent to a ferrodiorite intrusion, is characterized by elongate, aligned and interwoven Pl-rich (~50%) and Crd-rich (~50%) domains (see Figure 2-8). It has a modal mineralogy of: plagioclase ~41%, cordierite ~34%, orthopyroxene ~13%, K-feldspar ~ 10%, ilmenite ~1%, garnet <1%, spinel <1%. Minerals observed in trace amount include: magnetite, biotite, quartz, chlorite, zircon, monazite and pyrrhotite.

The Crd-rich domains consist of a cordierite groundmass enclosing medium-grained xenoblastic orthopyroxene and elongate Spl–Crd surrounded by a monomineralic rim of cordierite (see Figure 2-8B). These domains are similar to the Opx–Crd and Spl–Crd domains observed in Type A samples (see Section 2.1.2.1). However, the Spl–Crd and Opx–Crd regions in this type are not separated by quartzofeldspathic material, as is seen in Type A samples (see Section 2.1.2.1). Pl-rich domains are ~2–7 mm thick (see Figure 2-8) and are composed of medium-grained, locally micro-antiperthitic (see Figure 2-9A) plagioclase groundmass enclosing xenoblastic medium-grained orthopyroxene (see Figure 2-8a) and coarse-grained, fractured micro-perthitic K-feldspar pockets (2–5 mm and 2–10 mm long; see Figures 2-8A,C, 2-9B,C). There are two boundary relationships observed between the K-feldspar pockets and surrounding plagioclase:

(i) K-feldspar encloses xenoblastic plagioclase which is rounded in contact with K-feldspar (see Figures 2-8C, 2-9C);

(ii) and xenoblastic orthopyroxene occurs along the boundary isolated from the K-feldspar by a monomineralic rim of plagioclase (see Figures 2-8A, 2-9B).

Plagioclase in-fills fractures within, and corrodes, the coarse-grained K-feldspar (see Figure 2-9D). This Pl-rich domain is similar to the quartz-poor quartzofeldspathic domain observed in Type A, sample BR-90-327 with respect to the spatial distribution of feldspars. Medium- to coarse-grained xenoblastic ilmenite is present in both textural domains.

2.1.3.2 *Mineral Chemistry*

In sample BR-85-308, **plagioclase** has a narrow range of compositions with X_{An} = 0.35–0.39, X_{Ab} = 0.57–0.64 and X_{Or} = 0.01–0.05 (see Table 2-2). Individual plagioclase grains show a weak decrease in X_{An} (<0.01) towards the rounded rims in contact with K-feldspar. **K-feldspar** is ternary with X_{Or} = 0.79–0.86, X_{Ab} = 0.12–0.18, X_{An} = 0.01–0.04 (see Table 2-3). The exception is the exsolution lamellae within anti-perthitic plagioclase which are orthoclase. K-feldspar along the rim of coarse K-feldspar pockets, in contact with rounded rims of plagioclase and adjacent plagioclase-rimmed orthopyroxene is slightly enriched in X_{Or} (by 0.03) with respect to the core of the coarse-grained K-feldspar. **Cordierite** has X_{Fe} = 0.36–0.38 (see Table 2-4). **Orthopyroxene** is hypersthene with X_{Fs} = 0.57–0.60 and Al_2O_3 = 2.60–3.50 mol % (see Table 2-5). Orthopyroxene in the Pl-rich domain has slightly lower X_{Fs} (by 0.02) than in the Crd-rich domain. **Spinel** has X_{Fe} = 0.81–0.83, X_{Mg} = 0.17–0.19, TiO_2 = 0.13–0.18, Cr_2O_3 = 0.46–0 .70 mol%, ZnO = 1.22–0.31 mol% and MnO = 0.13–0.16 mol%.

2.1.4 Type C Samples

2.1.4.1 Petrography

Type C samples (BR-85-275 and BR-85-325, both from the same septum south of Anaktalik Brook, immediately adjacent to ferrodiorite and leuconorite intrusions) have a modal mineralogy of: cordierite 38–55%, plagioclase 20–23%, K-feldspar 11–16%, quartz 6–11%, orthopyroxene 1–7%, spinel 1–4%, ilmenite ~1%, biotite <1% and garnet <1%. These phases are distributed in five main textural domains. Based on their dominant mineralogy, these domains are defined as: Spl–Crd (10–40%), Pl–Crd (1–10%), Pl–Opx (2–5%), fine-grained Ksp–Qtz–Crd–Opx (20–30%) and coarse-grained Ksp–Qtz–Crd–Opx (10–40%; see Figure 2-10 for sample BR-85-275 and Figure 2-11 for sample BR-85-325). The distribution of these domains differs between the two samples. BR-85-275 is characterized by a 10mm thick layer of coarse-grained Ksp–Qtz–Crd–Opx located in between a mosaic of the remaining domains which are generally elongate parallel to the layering, defining a coarse foliation (see Figure 2-10). Alternately, BR-85-325 is mostly composed of a thick (>2cm) layer of aligned Spl–Crd domains partly rimmed by plagioclase and a ~1.5cm thick layer dominated by fine-grained Ksp–Qtz–Crd–Opx domains with subordinate Pl–Opx and Pl–Crd domains (see Figure 2-11). The different domains in these two layers are variably elongated defining a crude foliation. The coarse-grained Ksp–Qtz–Crd–Opx domain in BR-85-325 crosscuts both layers (see Figure 2-11). Fine to medium-grained biotite is present throughout both the samples. Minerals observed in trace amounts include: chlorite, corundum, zircon, monazite, magnetite, pyrrhotite, pyrite and chalcopyrite.

The Spl–Crd domains are generally elongate and range in size from 0.5 x 2.0 mm to 4.0 x 10.0 mm (see Figures 2-10A, 2-11A). These domains are composed of a Spl–Crd intergrowth with a corona of cordierite rimmed by medium-grained plagioclase. Locally, spinel is partially replaced by corundum. These domains are similar to those discussed in type A and B samples (see Sections 2.1.2.1 and 2.1.3.1).

The Pl–Crd domains are generally rounded, range in size from <0.5 mm to 3 mm and are composed of a medium-grained Pl–Crd symplectite enclosing minor fine-grained orthopyroxene (see Figures 2-10B, 2-11B). These domains are similar to, but more isolated than the Pl–Crd subdomain discussed in sample BR-90-327 (see section 2.1.2.1).

The Pl–Opx domains mainly occur as rims on the Spl–Crd domains but also form irregularly shaped pods (see Figures 2-10C, 2-11C). These domains range in size from 1 to 4 mm and are composed of medium-grained xenoblastic plagioclase and orthopyroxene with minor ilmenite and/or graphite. These domains are similar to those observed in type A and B samples (see Sections 2.1.2.1 and 2.1.3.1), but differ in spatial distribution.

The fine-grained Ksp–Qtz–Crd–Opx domains are subround to elongate and are composed of feathery intergrowths of Ksp–Qtz–Crd with skeletal orthopyroxene. These domains are rimmed by medium-grained plagioclase and locally have a corona of a radial Ksp–Pl symplectite (see Figures 2-10D, 2-11D, 2-12, 2-13).

The coarse-grained Ksp–Qtz–Crd–Opx domains form layers (see Figure 2-10E) that locally crosscut the main foliation (see Figure 2-11E). They are mainly composed of coarse-grained orthopyroxene containing quartz, ilmenite and cordierite inclusions (see Figures 2-10E, 2-11E, 2-14A), coarse-grained quartz (see Figures 2-9E, 2-10E, 2-14B) and coarse-grained locally perthitic K-feldspar (see Figures 2-10E, 2-11E). The K-feldspar is locally corroded (see Figure 2-15) by a fine to coarse-grained geometric Crd–Qtz intergrowth locally enclosing pockets of plagioclase and K-feldspar (see Figures 2-10E,F, 2-11E, 2-15, 2-16), similar to those observed within quartzofeldspathic domains in type A samples (see Figure 2-5 and Section 2.1.2.1). These coarse-grained domains also contain fine-grained Ksp–Pl symplectic pods (see Figure 2-14C) and medium-grained ilmenite rimmed by (radial) coronae of biotite with Bt–Qtz symplectites forming the outer rim.

Xenomorphic, lobate pockets of primarily K-feldspar (locally quartz or plagioclase) occur at grain boundaries and triple junctions between plagioclase grains (see Figures 2-11F, 2-17A,B) and are located within the fine and coarse-grained Ksp–Qtz–Crd–Opx domains and Pl–Opx domains. These xenomorphic pods range in size from <1mm to ~5mm. Surrounding plagioclase grains have a rounded shape against the xenomorphic pockets and locally have partial rims of Pl–Qtz symplectite (see Figure 2-17B). In addition, pockets and cracks within coarse perthitic K-feldspar are in-filled by very fine-grained Pl–Qtz symplectite and/or plagioclase and/or quartz and are present only within the coarse-grained Ksp–Qtz–Crd–Opx domain in BR-85-325.

2.1.4.2 *Mineral Chemistry*

Ranges in mineral compositions in specific textural settings are given in Tables 2-2 to 2-5. **Plagioclase** is X_{An} = 0.34–0.42, X_{Ab} = 0.54–0.65 and X_{Or} = 0.00–0.05 (see Table 2-2) and its composition is similar in the different textural domains. Individual grains show a slight (<0.02) increase in X_{An} toward the rounded rims in contact with xenomorphic K-feldspar pockets.

The composition of **K-feldspar** ranges from ternary to orthoclase; X_{Or} = 0.67–0.97, X_{Ab} = 0.02–0.25, X_{An} = 0.00–0.11 depending on textural setting (see Table 2-3). K-feldspar within the fine-grained Ksp–Qtz–Crd–Opx domains and respective Ksp–Pl symplectic coronae, coarse-grained Ksp–Qtz–Crd–Opx domains and Ksp–Pl symplectic pods are ternary, whereas fine-grained xenomorphic melt pockets and fine-grained rims (in BR-85-275) are orthoclase. X_{Or} increases from core to rim in the Ksp–Pl symplectic coronae around fine-grained Ksp–Qtz–Crd–Opx domains. Xenomorphic pockets of K-feldspar range from orthoclase to ternary with increasing size of pocket. There is a slight increase in X_{Or} towards the rims of coarse-grained K-feldspar within the coarse-grained Ksp–Qtz–Crd–Opx domains.

Cordierite has X_{Fe} = 0.39–0.45 (see Table 2-4) and shows narrow ranges in composition in specific textural settings. Cordierite within sample BR-85-325 has, in general, higher

X_{Fe} relative to sample BR-85-275. There is a slight (<0.02) decrease in X_{Fe} towards the rims of the Pl–Crd domains in both samples.

Orthopyroxene is hypersthene with $X_{Fs} = 0.59–0.65$ and $Al_2O_3 = 2.10–3.33$ mol% (see Table 2-5). Also, orthopyroxene shows higher X_{Fs} within Pl–Crd domains relative to all other textural settings in sample BR-85-275.

Spinel has a generally homogeneous composition with $X_{Fe} = 0.85–0.86$, $ZnO = 0.52–0.80$ mol%, $Cr_2O_3 = 0.19–0.42$ mol%, $MnO = 0.14–0.24$ mol% and $TiO_2 = 0.14–0.46$ mol%. TiO_2 values decrease in the core of elongate Spl–Crd domains.

Biotite has $X_{Fe} = 0.28–0.38$, slightly increasing when in contact with ferromagnesian minerals, F = 1.23-2.16 cations p.f.u. and $TiO_2 = 2.33–4.06$ mol% slightly increasing with proximity to ilmenite. In general there is a 0.04 increase in X_{Fe} and a 0.5 mol% increase in TiO_2 towards the rims of biotite grains.

2.1.5 Type D Samples

2.1.5.1 Petrography

This type is represented by sample DL-85-96, which comes from a location ~25km south of Anaktalik Brook and proximal to the Cabot Lake ferrodiorite intrusion. The sample is characterized by Sil-rich domains (~15%) between Fa-rich domains (~50%) in one side of the sample and a quartzofeldspathic domain (~35%, see Figure 2-18) which is dominant on the other side. It has a modal mineralogy of: K-feldspar 25%, cordierite 22%, plagioclase 16%, orthopyroxene 15%, quartz 10%, olivine 4%, sillimanite 3%, spinel 3%, biotite 1%, garnet <1% and ilmenite <1%. Minerals observed in trace amount include: chlorite, muscovite, pyrrhotite, rutile, magnetite, pyrite, monazite, zircon, corundum and chalcopyrite.

The Fa-rich domains are composed of a fine-grained intergrowth of orthopyroxene, cordierite and skeletal fayalite (with spinel inclusions) surrounded by an Opx–Crd intergrowth (see Figures 2-18A, 2-19A,B). These domains have coronae of orthopyroxene and fine rims of plagioclase and/or cordierite. The crystal habit of the orthopyroxene grains in the coronae shows a distinct correlation to the surrounding matrix minerals. Orthopyroxene in contact with quartz is coarse and granoblastic, whereas orthopyroxene in contact with K-feldspar is fine-grained and acicular (see Figure 2-19A). There is a gradual transition between the Opx–Crd intergrowths and the Spl–Pl–Crd–Opx intergrowth where the Fa-rich domain is adjacent to the Sil-rich domain.

The Sil-rich domains are composed of coarse-grained xenoblastic to idiomorphic sillimanite surrounded by coronae of fine-grained intergrowths of Spl–Pl–Crd–Opx (see Figures 2-18A, 2-20A). The fine-grained intergrowth is present only along boundaries between the Sil-rich and Fa-rich domains (see Figure 2-18). Locally, coarse sillimanite grains have coronae of Spl–Pl or Spl–Crd intergrowths (see Figure 2-20B). Plagioclase is medium to coarse-grained and interstitial between sillimanite grains. Due to differences in composition, plagioclase observed within the Spl–Pl intergrowth coronae luminesces a bright green yellow, whereas interstitial plagioclase and plagioclase within the fine-grained intergrowth of Spl–Pl–Crd–Opx luminesces a medium blue (see Figure 2-20A). Ilmenite is xenoblastic and medium-grained with biotite coronae throughout the assemblage.

The quartzofeldspathic domain is mainly composed of coarse mortar-textured perthitic K-feldspar with regions rich in plagioclase and xenoblastic and elongate to equant quartz (see Figures 2-18C, 2-19C, 2-20C, 2-20D). Matrix plagioclase grains are locally rounded along shared grain boundaries with K-feldspar and contain rims which appear darker in both back scattered electron imaging and cathodoluminescence imaging (see Figure 2-20C). In matrix regions rich in corroded plagioclase, the plagioclase grains are within a matrix of xenoblastic K-feldspar (see Figure 2-20D). Fractures in coarse K-feldspar are infilled with plagioclase.

2.1.5.2 Mineral Chemistry

Ranges in mineral composition in specific textural settings are given in Tables 2-2 to 2-5. In terms of composition, there are two contrasting types of **plagioclase** in this sample (see Table 2-2):

(a) Ca-rich, with $X_{An} = 0.75–0.88$, $X_{Ab} = 0.12–0.25$ and $X_{Or} = 0.00–0.01$;

(b) and Na-rich with $X_{An} = 0.07–0.40$, $X_{Ab} = 0.57–0.90$ and $X_{Or} = 0.00–0.09$.

The most calcic type is restricted to the Spl–Pl intergrowths around sillimanite and has a bright green yellow colour in cathodoluminescence images (see Figure 2-20B). All other plagioclase belongs to the Na-rich type, which luminesces a medium blue. Plagioclase within the fine-grained intergrowth of Spl–Pl–Crd–Opx around sillimanite has X_{An} = 0.38–0.40, X_{Ab} = 0.57–0.58 and X_{Or} = 0.03–0.04. Matrix plagioclase mainly has compositions of X_{An} = 0.29–0.36, X_{Ab} = 0.63–0.70 and X_{Or} = 0.00–0.03 except for some dark Na-rich rims in which compositions are X_{An} = 0.07–0.36, X_{Ab} = 0.65–0.90 and X_{Or} = 0.01–0.04.

Mortar textured **K-feldspar** in the matrix is ternary with X_{Or} = 0.75–0.85, X_{Ab} = 0.14–0.24 and X_{An} = 0.00–0.01 (see Table 2-3). Xenomorphic K-feldspar pockets within the matrix are near the orthoclase-ternary boundary with X_{Or} = 0.86–0.89, X_{Ab} = 0.10–13 and X_{An} = 0.00–0.01.

Cordierite ranges from X_{Fe} = 0.32–0.41 and is dependant on textural setting (see Table 2-4). The least ferrous cordierite is within the Spl–Crd intergrowth rims on sillimanite, and has X_{Fe} = 0.32–0.35, whereas the remaining cordierite has X_{Fe} = 0.36–0.41.

Orthopyroxene compositions are X_{Fs} = 0.57–0.61 and Al_2O_3 = 0.43–4.94 mol% (see Table 2-5). X_{Fs} varies slightly depending on textural setting, but Al_2O_3 ranges more widely. The least aluminous orthopyroxenes are within the granoblastic coronae around the fayalite-rich domain and have Al_2O_3 = 0.43–1.74 mol%. The acicular coronae show slightly higher values with Al_2O_3 = 1.41–2.07 mol%. The most aluminous orthopyroxenes occur within the fayalite-rich domain with Al_2O_3 = 1.66–4.94 mol%.

Spinel has X_{Fe} = 0.78–0.82, ZnO = 0.15–1.22 mol%, Cr_2O_3 = 0.05–0.28 mol%, MnO = 0.17–0.48 mol% and TiO_2 = 0.03–0.18 mol% and its composition depends on textural setting. ZnO is highest in spinel inclusions in fayalite (1.08–1.22 mol%) and lowest in spinel intergrown with plagioclase, cordierite and/or orthopyroxene (0.15–0.75 mol %). MnO is lowest in spinel inclusions in fayalite (0.17–0.18 mol%) and slightly higher within the Spl–Pl–Crd–Opx intergrowths (0.25–0.48 mol%).

Biotite coronae around ilmenite throughout the assemblage has X_{Fe} = 0.33–0.34, F = 1.08-1.22 cations p.f.u. and TiO_2 = 2.67–2.81 mol%. **Olivine** is fayalite with X_{Fa} = 0.75–0.77, X_{Fo} = 0.23–0.25, TiO_2 = 0.00–0.02 mol% and MnO = 0.50–0.56 mol%.

2.1.6 Type E Samples

2.1.6.1 Petrography

This type is represented by sample BR-85-621, located west of Anaktalik Bay, adjacent to a ferrodiorite intrusion, and is characterized by a feldspathic domain (~50%) enclosing garnetiferous domains (~30%), Spl–Pl domains (~10%) and a coarse-grained Ksp–Qtz–

Opx domain (~10%; see Figure 2-21). It has a modal mineralogy of: plagioclase 52%, garnet 13%, orthopyroxene 11%, spinel 7%, K-feldspar 6%, biotite 5%, quartz 2%, cordierite 1%, ilmenite <1%. Ilmenite is present primarily in the feldspathic matrix and the coarse-grained domain. Minerals observed in trace amount include: chlorite, magnetite, corundum, muscovite, pyrrhotite, sillimanite, zircon, apatite, pyrite, monazite, graphite and chalcopyrite.

The garnetiferous domains are augen-shaped and 4–9 mm wide and 8–14 mm long (see Figure 2-21A). They are composed of medium-grained Grt–Spl–Opx–Pl–Bt with coarse to medium-grained biotite and locally fine-grained cordierite along the rims (see Figures 2-21A, 2-22A, 2-23). Locally, plagioclase forms thin coronae around spinel and garnet (see Figure 2-23).

The Spl–Pl domains are form-fitting to garnetiferous domains, amoeboid and are <1 to 4 mm wide by 3–15 mm long (see Figure 2-21B). They are composed of medium-grained subidioblastic Spl–Pl intergrowths with medium to coarse-grained ilmenite, biotite and K-feldspar (see Figures 2-21B, 2-22A,B).

The coarse-grained Ksp–Qtz–Opx domain is ~10 x 14mm in size and is composed of coarse- to very coarse-grained orthopyroxene (with K-feldspar and quartz inclusions), quartz and K-feldspar with medium-grained plagioclase (see Figure 2-21C). The domain is surrounded by a fine-grained rim of Pl–Qtz symplectites (see Figure 2-24A). Orthopyroxene is heavily altered to chlorite. K-feldspar has abundant fractures which are in-filled by plagioclase. There is an abundance of zircon, monazite and apatite, in this domain.

The feldspathic domain forms a network (matrix) enclosing the other domains and is composed primarily of xenoblastic to subidioblastic plagioclase with subordinate medium-grained xenoblastic orthopyroxene (see Figure 2-21D) as well as xenomorphic lobate pockets of K-feldspar (see Figures 2-21D, 2-24B). Rims of plagioclase against these pockets are rounded (see Figure 2-24B). Medium- to coarse-grained ilmenite, locally surrounded by coarse-grained biotite, is observed in this domain.

2.1.6.2 *Mineral Chemistry*

Ranges in mineral composition in specific textural settings are given in Tables 2-2 to 2-5. **Plagioclase** has a wide range in composition with $X_{An} = 0.33–0.89$, $X_{Ab} = 0.10–0.65$ and $X_{Or} = 0.00–0.03$, which strongly depends on textural setting (see Table 2-2). The garnetiferous and Spl–Pl domains contain the most An-rich plagioclase, $X_{An} = 0.56–0.89$, with highest X_{An} in plagioclase coronae around spinel and garnet. Towards the core of the Spl–Pl domains there is a slight decrease in X_{An}. In the matrix and coarse-grained Ksp–Qtz–Opx domain plagioclase is more Ab-rich with $X_{An} = 0.33–0.46$ but with compositions depending on proximity to different textural settings. Matrix plagioclase increases in X_{An} with proximity to the garnetiferous domain to as high as $X_{An} = 0.57$.

Matrix plagioclase also increases in X_{An} with proximity to the Spl–Pl domains to as high as $X_{Ab} = 0.66$.

K-feldspar ranges from ternary to orthoclase depending on textural setting (see Table 2-3). K-feldspar within the coarse-grained Ksp–Qtz–Opx domain is ternary with X_{Or} = 0.75–0.88, X_{Ab} = 0.12–0.22 and X_{An} = 0.00–0.03. Orthoclase feldspar occurs in the feldspathic matrix within the xenomorphic pockets and has X_{Or} = 0.91–0.96, X_{Ab} = 0.04–0.08 and X_{An} = ~0.00. X_{Or} increases towards rims of coarser orthoclase and is highest in the finest grains.

Cordierite has X_{Fe} = 0.33–0.34 (see Table 2-4). **Orthopyroxene** has X_{Fs} = 0.51–0.66 and Al_2O_3 = 1.51–2.92 mol% (see Table 2-5) and its composition varies depending on textural setting. The most Fe-rich orthopyroxene is within the coarse-grained Ksp–Qtz–Opx domain and shows a decrease in X_{Fs} towards the rims of individual grains. The least Fe-rich orthopyroxene is found within the garnetiferous domain.

Spinel within the garnetiferous domain has X_{Fe} = 0.74–0.76, ZnO = 1.37–1.68 mol%, Cr_2O_3 = 0.08–0.16 mol%, MnO = 0.03–0.09 mol% and TiO_2 = 0.03–0.08 mol%. In contrast, spinel within the Spl–Pl domain is more Fe-rich with X_{Fe} = 0.86–0.90, ZnO = 0.40–0.56 mol%, Cr_2O_3 = 0.07–0.10 mol%, MnO = 0.22–0.29 mol% and TiO_2 = 0.08–0.20 mol%.

Garnet is Fe-rich with $X_{Alm} = 0.73–0.76$, $X_{Prp} = 0.19–0.22$, $X_{Grs} = 0.04–0.05$ and $X_{Sps} = \sim 0.01$. There is a slight decrease in X_{Alm} and increase in X_{Prp} towards the core of the augen-shaped garnetiferous domains (see Figure 2-23). BSE imaging shows three distinct brightness levels of garnet throughout these domains. This does not correspond to measured compositional differences and cannot be explained further.

Biotite has compositions $X_{Fe} = 0.31–0.50$, F = 0.59-1.04 cations p.f.u. and TiO_2 = 1.96–4.07 mol% depending on textural setting. The more magnesian biotite ($X_{Fe} = 0.31–0.36$) is associated with the garnetiferous domain, whereas the more ferrous biotite ($X_{Fe} = 0.46–0.50$) is associated with the matrix and the Spl–Pl domains. TiO_2 increases with association with titanium bearing minerals such as spinel, within garnetiferous and Spl–Pl domains (TiO_2 = 2.18–4.07 mol%), and ilmenite within the feldspathic matrix (TiO_2 = 3.56–3.99 mol %). The least Ti-rich biotite (TiO_2 = 1.96–2.03 mol%) surrounds the garnetiferous domains, where biotite is primarily in contact with the feldspathic matrix and only minor spinel.

2.2 Bulk Chemistry

Bulk compositions (in wt% and mol%; based on mineral compositions) and modal mineralogies of the 7 contact metamorphosed samples are given in Table 2-6 (for analytical techniques, see Section 1.6.3). These compositions are plotted on an AFM diagram and variation diagrams (in mol %) with selected composition data from Tettelaar and Indares (2007) for comparison (see Figures 2-25, 2-26 and Table 2-7).

In the AFM diagram, all the samples, from both this study and the selected samples from Tettelaar and Indares (2007), have an Al-index of 20–50 and an X_{Fe} of 50–70. These ranges are consistent with aluminous pelites.

Among the samples of this study, types A, B and C samples are chemically similar with the highest SiO_2 contents and intermediate Al_2O_3 and CaO. However, type A sample BR-90-327 has:

(i) the highest K_2O of all samples, in accordance with its markedly higher K-feldspar modal percentage; and

(ii) the lowest MgO, linked to the lower modal percentage of orthopyroxene in this sample.

Type B sample BR-85-308 has the highest Na_2O in accordance with its markedly higher plagioclase modal percentage. Type C sample BR-85-275 has:

(i) the highest SiO_2 and is most comparable to the range of samples from Tettelaar and Indares (2007; particularly aureole samples TL02-73, TL02-74 and regionally metamorphosed only sample TL-146H); and

(ii) noticeably higher K_2O than type C sample BR-85-325 in accordance with its 6% higher K-feldspar content.

Contact aureole samples TL02-73 and TL02-74 from Tettelaar and Indares (2007) are most comparable to the type C samples, with slightly more Na_2O (less so CaO).

K_2O, MgO and Na_2O ranges can be closely linked with related mineral percentages; however, little linkage can be made between the SiO_2 content and the modal percentage of quartz. For instance samples having little or no quartz, such as BR-85-308 and BR-90-327, have SiO_2 contents similar to those of samples containing 5% or more of quartz. This lack of quartz is thus more likely a result of quartz being consumed as a reactant in prograde reactions as opposed to an inherent low abundance of SiO_2 in the protolith.

The composition of sample type D (DL-85-96) lies close to the range defined by types A,B and C in the variation diagrams; however, it has slightly lower Al_2O_3 and the highest FeO+MgO of all the sample types. This composition also bears similarities with that of the screen sample TL02-29 from Tettelaar and Indares (2007).

Sample type E (BR-85-621) is chemically distinct from all the other sample types, in both this study and that of Tettelaar and Indares (2007). It has the lowest SiO_2 (~ 48 mol%) and the highest Al_2O_3 (20 mol %) and CaO (~6 mol). This composition is inconsistent with a pelitic protolith and likely represents an intermediate composition plutonic rock.

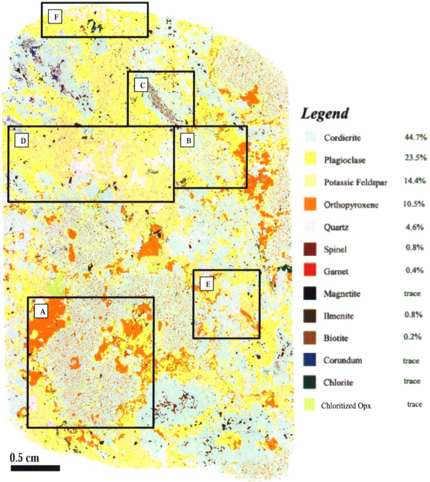

Figure 2-1. Mineralogical map of Type A sample BR-02-35. (A) Opx-Crd domain (B) Pl-Crd symplectite surrounding Crd-Opx symplectite; (C) Elongate Spl-Crd domain with Crd corona rimmed by Pl; (D) Quartzofeldspathic domain composed of coarse-grained Qtz, perthitic Ksp and Crd with minor medium-grained Opx and Pl; (E) Medium-grained geometric symplectite of Crd and Qtz rimmed by corroded feldspars and minor Opx; (F) Medium-grained corroded quartzofeldspathic region of corroded Pl and Ksp in interstitial Qtz.

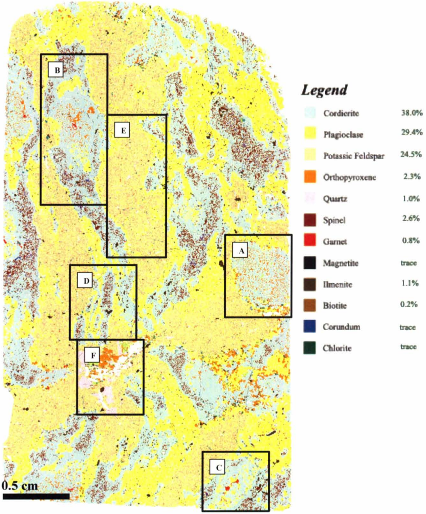

Figure 2-2. Mineralogical map of Type A sample BR-90-327. (A) Rounded Opx-Crd domain with symplectite radiating from center; (B) Rounded Opx-Crd domain with relict Grt at core flanked by coarse-grained Ple and a Pl-Crd intergrowth; (C) Rounded Pl-Crd domain with relict Grt at core; (D) Abundant and aligned Spl-Crd domains composed of Spl-Crd intergrowth with a Crd corona, all rimmed by Pl; (E) Quartzofeldspathic domain composed of coarse perthitic Ksp with fine-grained Qtz all rimmed by Pl with minor Opx; (F) Isolated domain of coarse Opx and Qtz with minor chlorite and graphite (white).

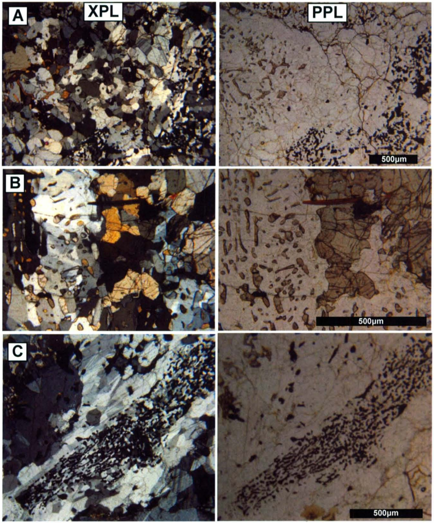

Figure 2-3. Photomicrographs of Type A Samples. (A) Rounded Opx-Crd domains wrapped by elongate Spl-Crd domains, flanked by coarse-grained Pl (BR-90-327, location Fig 2-2b); (B) Coarse Opx atoll around rounded Opx-Crd domain (BR-02-35, location Fig 2-1a); (C) Elongate Spl-Crd domain: Spl-Crd intergrowth with Crd corona and minor Pl rim (BR-02-35, location Fig 2-1c).

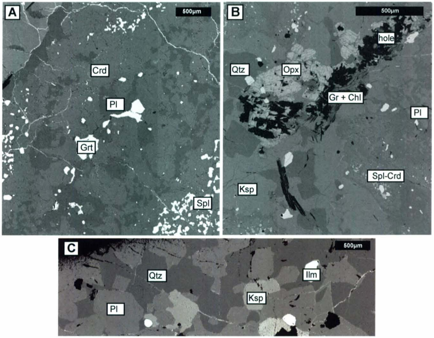

Figure 2.4. BSE images of Type A samples. (A) Rounded Pl-Crd domain with corroded Grt at core (BR-90-327, location Fig 2-2C); (B) Isolated coarse-grained domain of Opx-Qtz with minor Gr and Chl (BR-90-327, location Figure 2-2F); (C) Medium-grained quartzofeldspathicregion of corroded Pl and Ksp within interstitial Qtz (BR-02-35, location Fig 2-1F)

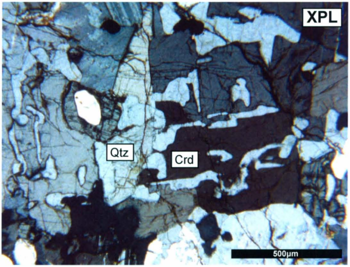

Figure 2-5. Photomicrograph of Type A sample BR-02-35. Geometric intergrowth of Crd-Qtz (location Fig 2-1E).

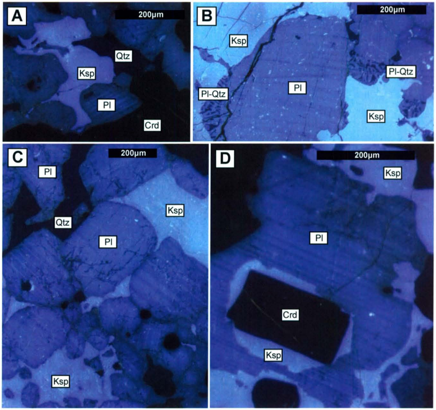

Figure 2-6. Cathodoluminescense images of type A samples. (A) Xenomorphic, lobate, interstitial pockets of Ksp and Qtz (BR-02-35); (B) Very fine-grained Pl-Qtz symplectite along edges of rounded Pl grains (BR-90-327); (C) Xenomorphic, lobate, interstitial pockets of Ksp and Qtz (BR-02-35); (D) Euhedral Crd within xenomorphic Ksp near Pl . (BR-02-35)

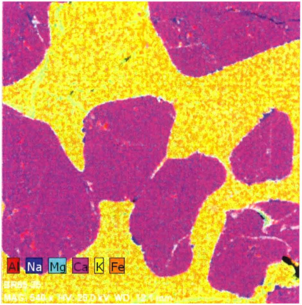

Figure 2-7. Element map of Pl with local albitic rim within Ksp (sample BR-02-35).

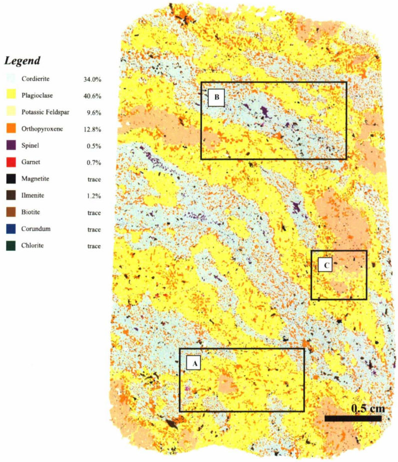

Figure 2-8. Mineralogical map of type B sample BR-85-308. (A) Pl-rich domain with medium-grained Pl groundmass enclosing anhedral medium-grained Opx with coarse-grained Ksp pocket; (B) Crd-rich domain with Crd groundmass enclosing medium grained anhedral Opx and elongate Spl-Crd intergrowths; (C) Xenomorphic, lobate pockets of Ksp along within coarse Ksp pockets within Pl-rich domain.

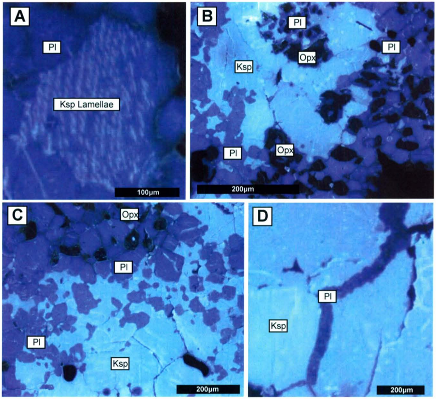

Figure 2-9. Cathodoluminescence images of type B sample BR-85-308. (A) Micro-antiperthite; (B) Ksp pockets within Pl-rich domain with medium-grained Opx. Boundary relationship showing Opx rimmed by monomineralic Pl; (C) Ksp pocket within Pl-rich domain. Boundary relationship illustrating Pl enclosed by Ksp; (D) Pl in-filling fracture in coarse Ksp.

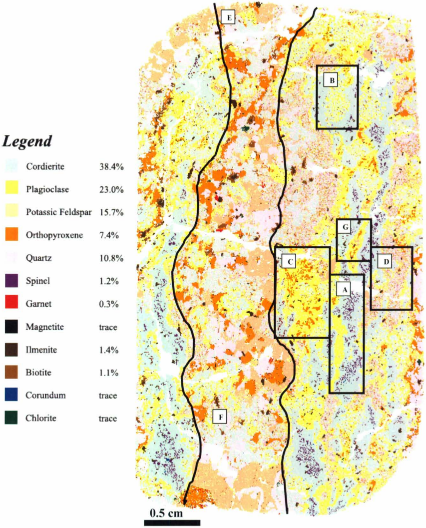

Figure 2-10. Mineralogical map of type C sample BR-85-275. (A) Spl-Crd domain: Spl-Crd intergrowth with Crd corona rimmed by Pl; (B) Pl-Crd domain with minor fine-grained Opx (C) Pl-Opx domain with minor Ilm; (D) Fine-grained feathery Ksp-Qtz-Crd intergrowth with skeletal Opx and a Ksp-Pl symplectite corona; (E) Coarse-grained Ksp-Qtz-Crd-Opx domain; (F) Fine- to coarse-grained geometric Crd-Qtz intergrowth with minor Pl and Ksp; (G) Xenomorphic lobate pocket of Ksp within Pl and Opx.

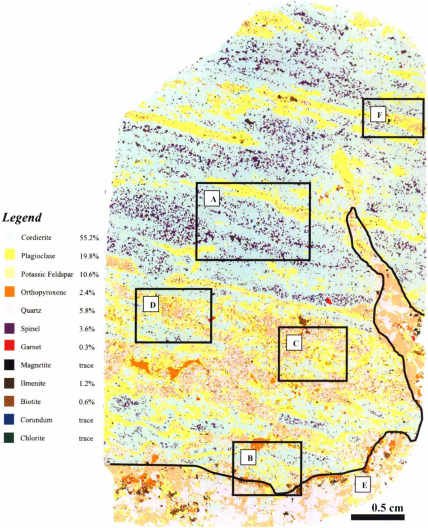

Figure 2-11. Mineralogical map of type C sample BR-85-325. (A) Spl-Crd domain with Spl-Crd intergrowth rimmed by a Crd corona; (B) Pl-Crd domain with minor Opx; (C) Pl-Opx domain; (D) Fine-grained feathery Ksp-Qtz-Crd intergrowth with skeletal Opx with Ksp-Pl symplectite corona; (E) Coarse-grained Ksp-Qtz-Crd-Opx domain; (F) Xenomorphic lobate pocket of Ksp within Pl.

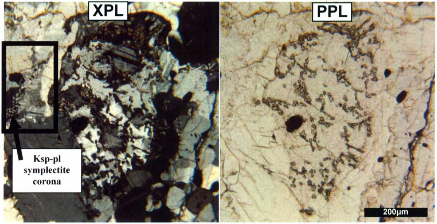

Figure 2-12. Photomicrograph of type C sample BR-85-325. Feathery intergrowth of Ksp-Qtz-Crd with skeletal Opx with a Ksp-Pl symplectite corona.

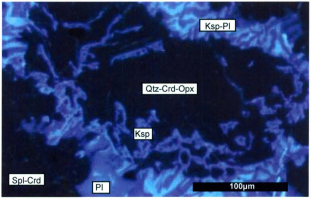

Figure 2-13. Cathodoluminescence image of type C sample BR-85-325. Feathery intergrowth of Ksp-Qtz-Crd-Opx with a Ksp-Pl symplectite corona.

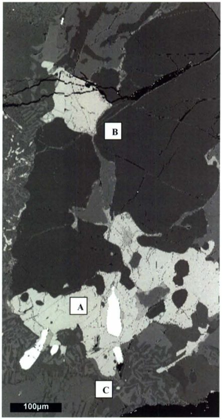

Figure 2-14. BSE image of type C sample BR-85-275. Coarse-grained Ksp-Qtz-Crd-Opx domain: (A) Coarse Opx with Qtz, Ilm and Crd inclusions; (B) coarse-grained Qtz; (C) Fine-grained Ksp-Pl symplectic pod.

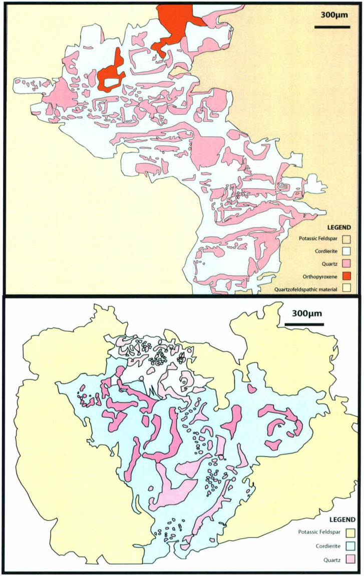

Figure 2-15. Line drawings of Crd-Qtz geometric intergrowths in corroded Ksp in type C sample BR-85-325. Different shades of pink (Qtz) and blue (Crd) represent different optical grain orientations.

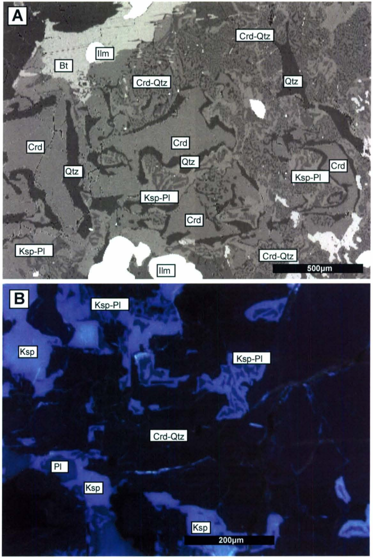

Figure 2-16. Crd-Qtz geometric intergrowths in type C samples. (A) BSE image of fine- to medium-grained geometric intergrowth of Crd-Qtz with minor Pl and Ksp (BR-85-275); (B) Cathodoluminescence image of pockets of Pl and xenomorphic Ksp enclosed by geometric intergrowth of Crd-Qtz (BR-85-325).

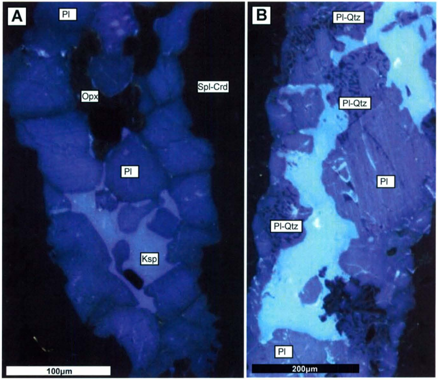

Figure 2-17. Cathodoluminescence images of type C samples. (A) Xenomorphic lobate pocket of Ksp at grain boundaries and triple-grain junction of Pl with rounded rims along shared grain boundaries with the xenomorphic pockets (BR-85-275). (B) Xenomorphic lobate Ksp pockets within Pl, rounded along shared grain boundaries with xenomorphic pockets and fine-grained pockets of Pl-Qtz symplectite (BR-85-325).

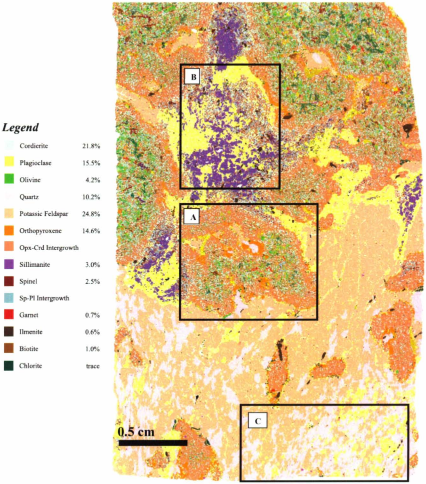

Figure 2-18. Mineralogical map of type D sample DL-85-96. (A) Fa-rich domain composed of fine-grained intergrowth of Opx-Crd and skeletal Fa with Spl inclusions surrounded by Crd-Opx intergrowth all with an Opx corona varying from granoblastic to acicular; (B) Sill-rich domain composed of coarse Sill with corona of fine-grained intergrowths of Spl-Pl-Crd-Opx and interstitial medium- to coarse-grained Pl; (c) Quartzofeldspathic domain composed of mortar-textured Ksp with region (right of box) rich in Pl and Qtz.

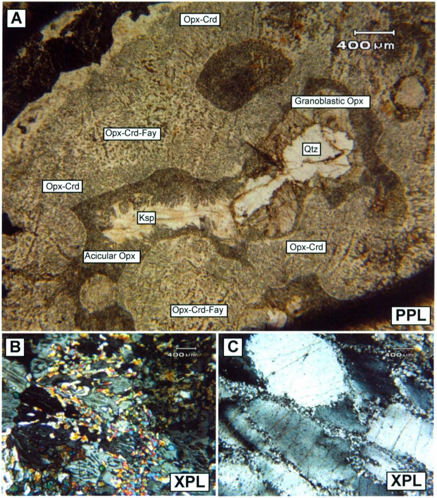

Figure 2-19. Photomicrographs of type D sample DL-85-96. (A) Fa-rich domain with fine-grained intergrowth of Opx-Crd and skeletal Fa with an Opx corona. The corona is granoblastic when adjacent to Qtz and acicular when adjacent to Ksp; (B) Opx-Crd intergrowth with skeletal Fa (highly birefringent mineral); (C) Mortar textured feldspathic region of quartzofeldspathic domain.

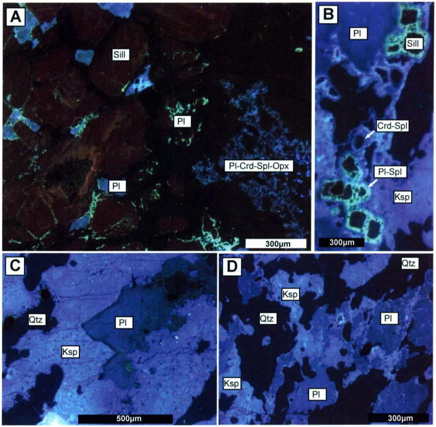

Figure 2-20. Cathodoluminescence images of type D sample DL-85-06. (A) Coarse Pl with dark rim in quartzofeldspathic domain; (B) Quartzofeldspathic domain, region rich in Pl and Qtz with xenomorphic Ksp; (C) Sill-rich domain with coarse anhedral to euhedral Sill with coronas of fine-grained intergrowth of Pl-Crd-Opx-Spl and interstitial medium- to coarse-grained Pl; (D) Sill with coronas of Pl-Spl and Crd-Spl intergrowths.

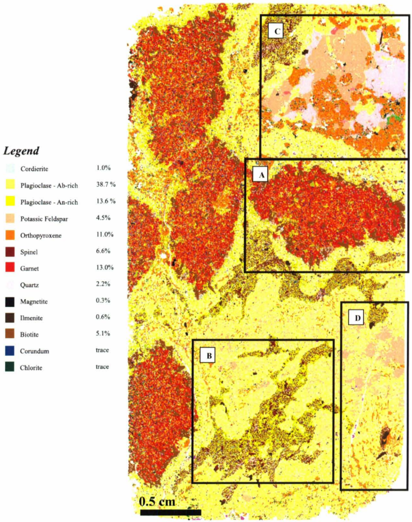

Figure 2-21. Mineralogical map of type E sample BR-85-621. (A) Garnetiferous domains composed of medium-grained Grt, Spl, Opx, Pl and Bt with coarse to medium-grained Bt and fine-grained Crd along the rims; (B) Spl-Pl domains with medium- to coarse-grained Ilm, Bt and Ksp throughout; (C) Coarse-grained Kfs-Qtz-Crd domain composed of coarse-grained Opx, Qtz and Ksp with subordinate medium-grained Pl; (D) Feldspathic matrix composed of Pl, xenomorphic Ksp pockets with subordinate Opx and coarse-grained Ilm with Bt corona.

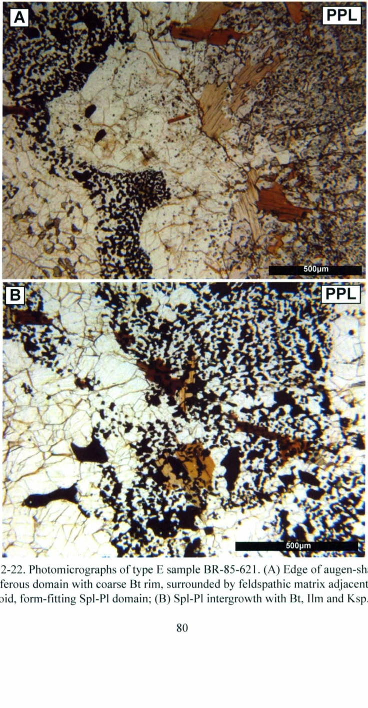

Figure 2-22. Photomicrographs of type E sample BR-85-621. (A) Edge of augen-shaped garnetiferous domain with coarse Bt rim, surrounded by feldspathic matrix adjacent to amoeboid, form-fitting Spl-Pl domain; (B) Spl-Pl intergrowth with Bt, Ilm and Ksp.

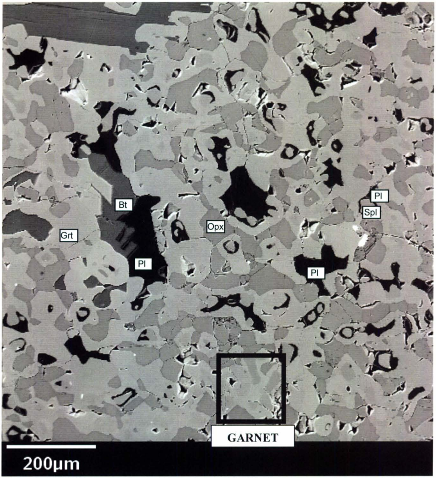

Figure 2-23. BSE image of type E sample BR-85-621. Back-scattered electron image of garnetiferous domain with Bt, Grt, Spl, Opx and Pl with fine-grained Pl coronas around Spl and Grt. Box shows different shades of garnet.

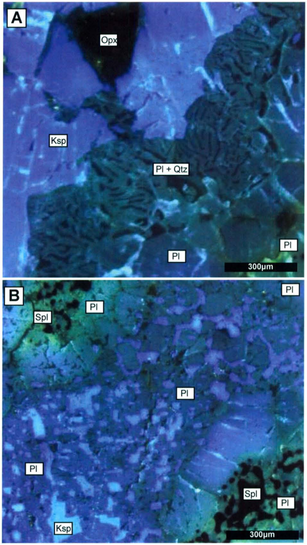

Figure 2-24. Cathodoluminescence images of type E sample BR-85-621. (A) Fine-grained rim of Pl-Qtz symplectite surrounding the coarse-grained Ksp-Opx domain; (B) Xenomorphic lobate pockets of Ksp between Pl grains with corroded rims along grain boundaries with Ksp.

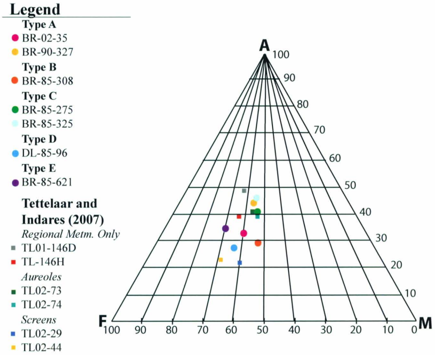

Figure 2-25. AFM diagram, projected from K-feldspar, showing plotting positions of samples from this study and from Tettelaar and Indares (2007).

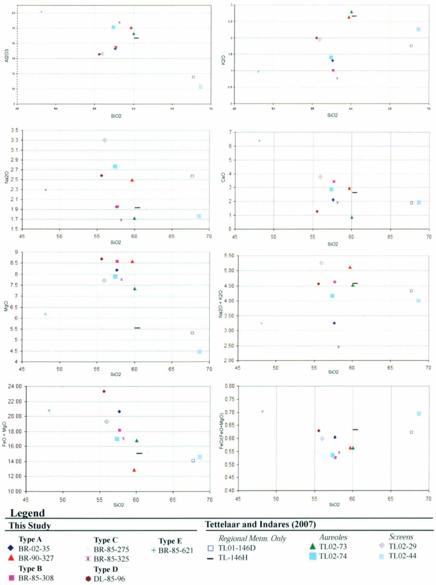

Figure 2-26. Variation diagrams (in mol%) of whole-rock compositions of samples from this study and 6 samples from Tettelaar and Indares (2007).

Table 2-1. Textural domains of sample Types A, B, C, D and E.

	A	B	C	D	E
	Domains (subdomains)				
(quartzo) Feldspathic	Mineralogically zoned (Ksp center/Pl rim; most prominent in Qtz-poor sample BR-90-327)	Mineralogically zoned domains (Ksp center/Pl Opx network rim); No Qtz		Mortar textured Ksp and Qtz, minor Pl	Mineralogically zoned (network of coarse to fine Ksp in center/Pl rim)
Pl-Opx	Surrounding Opx-Crd domains	Elongate network of Pl-Opx enclosing Ksp	Irregularly shaped pods and rimming Spl-Crd domains		Scattered anhedral Opx in Pl groundmass
Opx-Crd	Rounded Opx-Crd domains with by Opx(Pl) atoll	Elongate network of Opx-Crd enclosing Spl-Crd domains		Outer rim of fine grained Opx-Crd intergrowth surrounding Fay-Crd intergrowths	
Pl-Crd	Rounded Pl-Crd domains or rims along rounded Opx-Crd domains		Rounded Pl-Crd domains		
Spl-Crd	Elongate domains of Spl-Crd intergrowth with a monomineralic cordierite rim (Spl partially replaced by corundum)	Elongate domains of Spl-Crd intergrowth with a monomineralic cordierite rim	Elongate domains of Spl-Crd intergrowth with a monomineralic cordierite rim	Spl-Crd intergrowths as fine grained rims around Sill	
Fine-grained Ksp-Qtz-Crd-Opx			Subrounded to elongate domains rimmed by Pl-Ksp radial symplectite		
Coarse-grained Ksp-Qtz-Crd-Opx			Coarse grained Ksp-Qtz-Crd-Opx domain which aligns with (BR-85-275) and cross-cuts the main layering (BR-85-325)		
Garnet-rich					Coarse garnetiferous domains with Spl, Pl, Opx and Bt inclusions and a rim of coarse Bt
Spl-Pl				Spl-Pl intergrowths as fine grained rims around Sill	Amoeboid and form-fitting Pl-Spl intergrowths with An-rich Pl
Ksp-Qtz-Opx					Coarse grained Ksp-Qtz-Opx
Fayalite-rich				Fine grained Fay-Crd intergrowths (Fay locally with Spl inclusions) as core of coarse rounded region with a rim of an Opx-Crd intergrowth.	
Sill-Pl				Coarse grained subhedral to euhedral Sill rimmed by Pl	

Table 2-1. contd. Textural domains of sample Types A, B, C, D and E.

	A	B	C	D	E
Other Large Scale Features					
Geometric Crd-Qtz	Medium grained geometric Crd-Qtz intergrowth within quartzofeldspathic domains		Very fine to medium grained geometric intergrowth corroding coarse Ksp		
Fine microstructures involving quartzofeldspathic minerals					
Xenomorph-ic/interstitial pockets	Ksp (minor Qtz,Pl); <1-5mm wide; corrodes adjacent Pl	Large Ksp pockets; 2-5mm by 2-10mm; corrode adjacent and enclosed Pl	Ksp (minor Qtz, Pl); <1-5mm wide; corrode adjacent Pl	Ksp pockets within quartzofeldspathic domain; corrode adjacent and enclosed Pl	Ksp pockets within feldspathic domain; corrode adjacent Pl
Euhedral grains	Euhedral cordierite with film of Ksp, near and as inclusion in Pl (corroded against Ksp)				
Fine grained films	Films fo Ab-rich Pl (in contact with Pl) or ternary Fsp (in contact with Crd)	Pl rim around anhedral Opx all enclosed in large Ksp pockets		Dark (in BSE image) rims on Pl	Rim of Pl-Qtz symplectite around coarse grained Ksp-Qtz-Opx domain. Thin Pl coronas around Spl, Grt in garneiferous domain
In-filling of pods/cracks	Fine grained Pl-Qtz symplectite, Pl and/or Qtz; corrodes adjacent coarse perthitic Ksp	Pl fills fractures and corrodes surrounding Ksp	Fine grained Pl-Qtz symplectite, Pl and/or Qtz; corrodes surrounding coarse perthitic Ksp	Pl fills fractures and corrodes surrounding Ksp	Pl fills fractures and corrodes surrounding Ksp
Other					
Bt-Ilm	Medium grained Bt and Ilm (locally with Bt corona)	Medium grained Bt and Ilm (locally with Bt corona)	Medium grained Bt and Ilm (locally with radial Bt corona with Qtz exsolution at outer rim)	Medium grained Bt and Ilm (locally with biotite corona)	Medium to coarse grained Bt and Ilm (locally with biotite corona)
Deformation					
Relict regional structures	Overprinting of deformation textures (pressure shadows)	Coarse foliation defined by elongate domains	Coarse foliation defined by elongate domains		

Table 2-2. Plagioclase compositions in specific textural settings.

			Domains (subdomains)													Other Large Scale Features	Fine microstructures involving quartzofeldspathic minerals							Deformation	
			(quartzo) Feldspathic	Pl-Opx	Opx-Crd	Pl-Crd	Fine-grained Ksp-Qtz-Crd-Opx	Garnet-rich		Spl-Pl	Ksp-Qtz-Opx	Fayalite-rich	Sill-Pl			Geometric Crd-Qtz	Xenomorphic/interstitial pockets	Medium grained rims	Fine grained films		In-filling of pods/cracks			Relict regional structures	OVERALL
					Fine grained Pl within		*Ksp-Pl symplectic rims*	*Medium grained*	*Coronas on Spl and Grt*		*Fine grained Pl-Ksp symplectic rim*	*Rims on Opx coronas*	*Spl-Pl intergrowths around Sill*	*Coarse anhedral Pl*	*Spl-Crd-Opx-Pl intergrowth between domains*	*Fine grained Pl within*			*Albitic films along corroded rims*	*Ternary Fsp rims along corroded rims of Pl, in contact with Crd*	*Pl-Ksp symplectites*	*Pl-Qtz symplectites*	*Pl*	*Flanking Pl adjacent to Opx-Crd domains*	
Type A	BR-02-35	X_{An}	0.32-0.36		0.35-0.37	0.35-0.37													*0.01-0.07*	*~0.10*		0.34-0.35	0.33-0.35		**0.32-0.37**
		X_{Ab}	0.62-0.70		0.60-0.63	0.60-0.63													*0.85-0.91*	*~0.45*		0.65-0.66	0.63-0.68		**0.60-0.70**
		X_{Or}	0.01-0.03		0.02-0.04	0.02-0.03													*0.01-0.13*	*~0.45*		0.00-0.01	0.01		**0.01-0.04**
	BR-90-327	X_{An}	0.37-0.42		0.35-0.43	0.36-0.43																		0.36-0.40	**0.35-0.44**
		X_{Ab}	0.54-0.62		0.54-0.62	0.54-0.62																		0.57-0.61	**0.54-0.63**
		X_{Or}	0.01-0.05		0.02-0.04	0.02-0.04																		0.02-0.03	**0.01-0.05**
	Overall Range	X_{An}	**0.32-0.42**		**0.35-0.43**	**0.35-0.43**																**0.34-0.35**	**0.33-0.35**	**0.36-0.40**	***0.32-0.44***
		X_{Ab}	**0.54-0.70**		**0.54-0.63**	**0.54-0.63**																**0.65-0.66**	**0.63-0.68**	**0.57-0.61**	***0.54-0.70***
		X_{Or}	**0.01-0.05**		**0.02-0.04**	**0.02-0.04**																**0.00-0.01**	**0.01**	**0.02-0.03**	***0.01-0.05***
Type B	BR-85-308	X_{An}		0.35-0.39																					**0.35-0.39**
		X_{Ab}		0.57-0.64																					**0.57-0.64**
		X_{Or}		0.01-0.05																					**0.01-0.05**
Type C	BR-85-275	X_{An}		0.34-0.38		0.38-0.41	0.36-0.39									0.35-0.36	0.35-0.38	0.34-0.38			0.35-0.36				**0.34-0.41**
		X_{Ab}		0.57-0.64		0.57-0.60	0.60-0.63									0.63-0.64	0.61-0.65	0.57-0.64			0.63-0.64				**0.57-0.65**
		X_{Or}		0.02-0.05		0.02-0.03	0.00-0.01									0.01-0.02	0.00-0.01	0.02-0.05			0.01-0.02				**0.00-0.05**
	BR-85-325	X_{An}		0.37-0.42			0.35-0.39									0.37		0.36-0.39			0.34-0.40	0.37-0.38			**0.34-0.42**
		X_{Ab}		0.54-0.61			0.61-0.63									0.62		0.61-0.63			0.59-0.62	0.61-0.62			**0.54-0.63**
		X_{Or}		0.02-0.04			0.00-0.01									0.01		0.00-0.01			0.01-0.05	0.00-0.01			**0.00-0.05**
	Overall Range	X_{An}		**0.34-0.42**		**0.38-0.41**	**0.35-0.39**									**0.35-0.37**	**0.35-0.38**	**0.34-0.39**			**0.34-0.40**	**0.37-0.38**			***0.34-0.42***
		X_{Ab}		**0.54-0.64**		**0.57-0.60**	**0.60-0.63**									**0.62-0.64**	**0.61-0.65**	**0.57-0.64**			**0.59-0.64**	**0.61-0.62**			***0.54-0.65***
		X_{Or}		**0.02-0.05**		**0.02-0.03**	**0.00-0.01**									**0.01-0.02**	**0.00-0.01**	**0.00-0.05**			**0.01-0.05**	**0.00-0.01**			***0.00-0.05***
Type D	DL-85-96	X_{An}	0.29-0.32									0.34	0.75-0.88	0.31-0.32	0.38-0.40			0.07-0.34					0.33-0.36		**0.07-0.88**
		X_{Ab}	0.67-0.70									0.63	0.12-0.25	0.61-0.68	0.57-0.58			0.65-0.90					0.63-0.67		**0.12-0.90**
		X_{Or}	0.01-0.03									0.03	0.00-0.01	0.01-0.09	0.03-0.04			0.01-0.04					0.00-0.01		**0.00-0.09**
Type E	BR-85-621	X_{An}	0.35-0.66					0.59-0.68	0.84-0.89	0.43-0.75	0.33-0.36											0.35-0.36			**0.33-0.89**
		X_{Ab}	0.33-0.62					0.32-0.41	0.10-0.16	0.25-0.55	0.63-0.65											0.63-0.64			**0.10-0.65**
		X_{Or}	0.01-0.03					0.00-0.01	0	0.01-0.02	0.01-0.02											0.00-0.01			**0.00-0.03**

Table 2-3. K-feldspar compositions in specific textural settings

			Domains (subdomains)						Fine microstructures involving quartzofeldspathic minerals				OVERALL
				Fine-grained Ksp-Qtz-Crd-Opx			Opx-Qtz	Ksp-Qtz-Opx			In-filling of pods/cracks	Anti-perthite	
			(quartzo) Feldspathic	*Ksp-Pl symplectic rims*	*Ksp-Qtz-Crd-Opx intergrowth*	Coarse-grained Ksp-Qtz-Crd-Opx	*Fine grained Ksp*	*Fine grained Pl-Ksp symplectic rim*	Xenomorphic/interstitial pockets	Fine grained films	*Pl-Ksp symplectites*	*Exsolution lamellae*	
Type A	BR-02-35	X_{Or}	0.70-0.76						0.72-0.92				**0.70-0.94**
		X_{Ab}	0.21-0.28						0.07-0.25				**0.05-0.28**
		X_{An}	~0.03						0.01-0.08				**0.01-0.08**
	BR-90-327	X_{Or}	0.77-0.83				0.79-0.83		0.86-0.97				**0.77-0.97**
		X_{Ab}	0.15-0.19				0.15-0.18		0.03-0.12				**0.03-0.19**
		X_{An}	0.02-0.03				0.02-0.03		0.00-0.02				**0.00-0.03**
	Overall Range	X_{Or}	**0.70-0.83**				**0.79-0.83**		**0.72-0.97**				***0.70-0.97***
		X_{Ab}	**0.15-0.28**				**0.15-0.18**		**0.03-0.25**				***0.03-0.28***
		X_{An}	**0.02-0.03**				**0.02-0.03**		**0.00-0.08**				***0.00-0.08***
Type B	BR-85-308	X_{Or}	0.79-0.86									*0.94-0.97*	**0.79-0.86**
		X_{Ab}	0.12-0.18									*0.03-0.05*	**0.12-0.18**
		X_{An}	0.01-0.04									*0.00-0.01*	**0.01-0.04**
Type C	BR-85-275	X_{Or}		0.79-0.87	0.79-0.86	0.71-0.77			0.88-0.96	0.97-0.98	0.67-0.85	0.67-0.85	**0.67-0.98**
		X_{Ab}		0.12-0.20	0.16-0.19	0.21-0.25			0.04-0.11	0.02-0.03	0.14-0.22	0.14-0.22	**0.02-0.25**
		X_{An}		0.01-0.04	0.00-0.01	0.02-0.04			0.01-0.02	0.00	0.02-0.11	0.02-0.11	**0.00-0.11**
	BR-85-325	X_{Or}		0.77-0.88	0.81-0.85	0.78-0.86			0.88-0.89		0.83-0.85	0.83-0.85	**0.77-0.89**
		X_{Ab}		0.12-0.21	0.14-0.18	0.13-0.18			0.09-0.10		0.14-0.16	0.14-0.16	**0.09-0.21**
		X_{An}		0.00-0.03	0.00-0.01	0.01-0.04			0.00-0.01		0.00-0.01	0.00-0.01	**0.00-0.04**
	Overall Range	X_{Or}		**0.77-0.88**	**0.79-0.86**	**0.71-0.86**			**0.88-0.96**	**0.97-0.98**	**0.67-0.85**	**0.67-0.85**	***0.67-0.97***
		X_{Ab}		**0.12-0.21**	**0.14-0.19**	**0.13-0.25**			**0.04-0.11**	**0.02-0.03**	**0.14-0.22**	**0.14-0.22**	***0.02-0.25***
		X_{An}		**0.00-0.04**	**0.00-0.01**	**0.01-0.04**			**0.00-0.02**	**0.00**	**0.00-0.11**	**0.00-0.11**	***0.00-0.11***
Type D	DL-85-96	X_{Or}	0.75-0.85						0.86-0.89				**0.76-0.89**
		X_{Ab}	0.14-0.24						0.10-0.13				**0.10-0.24**
		X_{An}	0.00-0.01						0.00-0.01				**0.00-0.01**
Type E	BR-85-621	X_{Or}						0.75-0.88	0.91-0.96				**0.75-0.96**
		X_{Ab}						0.12-0.22	0.04-0.08				**0.04-0.22**
		X_{An}						0.00-0.03	0.00				**0.00-0.03**

Table 2-4. Cordierite compositions in specific textural settings.

		Domains (subdomains)								Other Large Scale Features	Fine microstructures		OVERALL
		Opx-Crd	Pl-Crd	Spl-Crd		Fine-grained Ksp-Qtz-Crd-Opx	Fayalite-rich	Sill-Pl		Geometric Crd-Qtz	Euhedral grains	Fine grained rims	
				Rim around Spl-Crd intergrowth	*Spl-Crd intergrowth*		*Opx (Fa)-Crd intergrowth*	*Spl-Crd-Opx-Pl intergrowth*	*Spl-Crd intergrowth around Sill*				
Type A	BR-02-35	0.37-0.39	0.41-0.42	0.40-0.42	0.38-0.40					0.40-0.41	0.40-0.41		**0.37-0.42**
	BR-90-327	0.39-0.43	0.39-0.44	0.44	0.40-0.43								**0.39-0.44**
	Overall Range	**0.37-0.43**	**0.39-0.44**	**0.40-0.44**	**0.38-0.43**					**0.40-0.41**	**0.40-0.41**		***0.37-0.44***
Type B	BR-85-308	0.36-0.38		0.36-0.38	0.36-0.38								**0.36-0.38**
Type C	BR-85-275		0.42-0.43	0.40-0.43	0.39-0.41	0.40-0.41				0.39-0.41			**0.39-0.43**
	BR-85-325		0.44	0.43	0.42	0.40-0.41				0.41-0.45			**0.40-0.45**
	Overall Range		**0.42-0.44**	**0.40-0.43**	**0.39-0.42**	**0.40-0.41**				**0.39-0.45**			***0.39-0.45***
Type D	DL-85-96	0.38-0.39					0.36-0.39	0.39-0.40	0.32-0.35			0.39-0.41	**0.32-0.41**
Type E	BR-85-621											0.33-0.34	**0.33-0.34**

Table 2-5. Orthopyroxene compositions in specific textural settings.

			Domains (subdomains)														Overall
			(quartzo) Feldspathic	Pl-Opx	Opx-Crd		Pl-Crd	Fine-grained Ksp-Qtz-Crd-Opx	Coarse-grained Ksp-Qtz-Crd-Opx	Garnet-rich	Opx-Qtz	Ksp-Qtz-Opx	Fayalite-rich				
					Opx-Crd intergrowths	Coarse Opx atolls	Fine grained within						*Opx-Crd-(Spl-Pl) intergrowths*	*Opx-(Fa)-Crd intergrowths*	*Acicular corona*	*Granoblastic corona*	
Type A	BR-02-35	X_{Fs}	0.60-0.62		0.61-0.63	0.60-0.61											0.60-0.63
		Al2O3 mol%	2.09-3.16		2.54-3.23	2.12-3.08											2.09-3.23
		Al4 Site	0.09-0.13		0.10-0.15	0.08-0.11											0.08-0.15
		Al6 Site	0.08-0.13		0.10-0.11	0.07-0.11											0.07-0.13
	BR-90-327	X_{Fs}	0.61-0.62		0.59-0.64						0.61-0.62						0.59-0.64
		Al2O3 mol%	3.06-3.69		2.73-3.51						2.91-3.12						2.73-3.51
		Al4 Site	0.13-0.17		0.12-0.17						0.14-0.16						0.12-0.17
		Al6 Site	0.10-0.12		0.10-0.14						0.07-0.10						0.07-0.14
	Overall Range	X_{Fs}	**0.60-0.62**		**0.59-0.64**	**0.60-0.61**					**0.61-0.62**						*0.59-0.64*
		Al2O3 mol%	**2.09-3.69**		**2.54-3.54**	**2.12-3.08**					**2.97-3.12**						*2.09-3.69*
		Al4 Site	**0.09-0.17**		**0.10-0.17**	**0.08-0.11**					**0.14-0.16**						*0.08-0.17*
		Al6 Site	**0.08-0.13**		**0.10-0.14**	**0.07-0.11**					**0.07-0.10**						*0.07-0.14*
Type B	BR-85-308	X_{Fs}		0.57-0.58	0.58-0.60												0.57-0.60
		Al2O3 mol%		2.60-3.47	2.98-3.50												2.60-3.50
		Al4 Site		0.10-0.13	0.12-0.14												0.10-0.14
		Al6 Site		0.10-0.13	0.11-0.13												0.10-0.13
Type C	BR-85-275	X_{Fs}		0.59-0.61			0.62-0.64	0.61	0.60-0.61								0.59-0.64
		Al2O3 mol%		2.88-3.33			3.14-3.20	2.10-3.31	2.61-2.90								2.10-3.33
		Al4 Site		0.10-0.14			0.12-0.13	0.07-0.13	0.10-0.13								0.07-0.14
		Al6 Site		0.11-0.14			0.11-0.13	0.09-0.13	0.09-0.11								0.09-0.14
	BR-85-325	X_{Fs}		0.6				0.61-0.62	0.62-0.65								0.60-0.65
		Al2O3 mol%		2.75-3.10				2.32-2.50	2.46-3.15								2.32-3.15
		Al4 Site		0.11-0.12				0.08-0.13	0.11-0.13								0.08-0.13
		Al6 Site		0.08-0.11				0.09-0.11	0.12-0.13								0.08-0.13
	Overall Range	X_{Fs}		**0.59-0.60**			**0.62-0.64**	**0.61-0.62**	**0.60-0.65**								*0.59-0.65*
		Al2O3 mol%		**2.75-3.33**			**3.14-3.20**	**2.10-3.31**	**2.46-3.15**								*2.10-3.33*
		Al4 Site		**0.10-0.14**			**0.12-0.13**	**0.07-0.13**	**0.10-0.13**								*0.07-0.14*
		Al6 Site		**0.08-0.14**			**0.11-0.13**	**0.09-0.13**	**0.09-0.13**								*0.08-0.14*
Type D	DL-85-96	X_{Fs}											0.59-0.60	0.57-0.58	0.58-0.60	0.58-0.61	0.57-0.61
		Al2O3 mol%											2.03-2.67	1.66-4.94	1.41-2.07	0.43-1.74	0.43-4.94
		Al4 Site											0.09-0.12	0.09-0.18	0.05-0.09	0.02-0.04	0.02-0.18
		Al6 Site											0.06-0.09	0.04-0.20	0.04-0.07	0.01-0.06	0.01-0.20
Type E	BR-85-621	X_{Fs}	0.55-0.61							0.51		0.64-0.66					0.51-0.66
		Al2O3 mol%	1.51-2.92							2.07-2.58		2.59-2.87					1.51-2.92
		Al4 Site	0.07-0.08							0.09-0.13		0.05-0.08					0.05-0.13
		Al6 Site	0.05-0.07							0.07-0.10		0.06-0.08					0.05-0.10

Table 2-6. Modal mineralogies and bulk compositions of all sample types.

		A		B	C		D	E
		BR-02-35	BR-90-327	BR-85-308	BR-85-275	BR-85-325	DL-85-96	BR-85-621
Mineral	**Plagioclase**	23.54	29.45	40.75	24.69	19.85	15.67	53.17
	K-Feldspar	14.37	24.52	9.62	16.84	10.68	25.05	6.50
	Quartz	4.55	1.04	0.09	4.88	5.80	10.34	2.26
	Cordierite	44.74	37.98	34.17	41.21	55.51	22.06	1.03
	Orthopyroxene	10.51	2.33	12.89	7.99	2.36	14.71	11.21
	Spinel	0.79	2.60	0.51	1.33	3.66	2.53	6.71
	Biotite	0.24	0.24	0.09	1.18	0.64	1.03	5.20
	Sillimanite	0.04	0.00	0.00	0.05	0.02	3.03	0.11
	Garnet	0.45	0.75	0.68	0.35	0.32	0.66	13.18
	Fayalite	0.00	0.00	0.00	0.00	0.00	4.29	0.00
	Ilmenite	0.77	1.09	1.20	1.46	1.17	0.62	0.63
TOTAL		**100.00**	**100.00**	**100.00**	**100.00**	**100.00**	**100.00**	**100.00**
Mol % Oxides	**SiO_2**	57.64	59.69	57.40	61.51	58.20	55.58	48.11
	Al_2O_3	15.27	18.08	15.34	16.12	18.73	14.49	20.19
	MgO	8.18	5.62	8.53	6.97	7.76	8.68	6.18
	FeO	12.46	7.26	9.46	8.27	9.32	14.61	14.62
	CaO	2.11	2.94	3.40	2.05	1.91	1.24	6.38
	Na_2O	1.95	2.49	3.59	1.90	1.68	2.58	2.29
	K_2O	1.30	2.63	0.99	1.55	0.77	1.98	0.97
	TiO_2	0.62	0.86	0.94	1.11	0.97	0.54	0.71
	H_2O	0.47	0.43	0.35	0.52	0.66	0.30	0.54
TOTAL		**100.00**	**100.00**	**100.00**	**100.00**	**100.00**	**100.00**	**100.00**
Wt% Oxides	**SiO_2**	51.96	52.58	52.06	55.23	51.71	49.99	41.86
	Al_2O_3	23.36	27.02	23.61	24.56	28.24	22.11	29.81
	MgO	4.95	3.32	5.19	4.20	4.63	5.24	3.61
	FeO	13.43	7.65	10.26	8.88	9.90	15.71	15.21
	CaO	1.78	2.42	2.88	1.72	1.58	1.04	5.18
	Na_2O	1.81	2.26	3.36	1.76	1.54	2.39	2.06
	K_2O	1.84	3.63	1.41	2.18	1.07	2.79	1.32
	TiO_2	0.74	1.01	1.13	1.33	1.15	0.65	0.82
	H_2O	0.13	0.11	0.09	0.14	0.18	0.08	0.14
TOTAL		**100.00**	**100.00**	**100.00**	**100.00**	**100.00**	**100.00**	**100.00**
X_{Fe}		**0.60**	**0.56**	**0.53**	**0.54**	**0.55**	**0.63**	**0.70**

Table 2-7. Bulk compositions in mol% oxides and AFM values, projected from K-feldspar, of samples from this study and from Tettelaar and Indares (2007).

	Mol % of oxides	SiO2	Al2O3	MgO	FeO	CaO	Na2O	K2O	TiO2	H2O	*A*	*F*	*M*
This Study													
A	BR-85-35	57.63	15.27	8.18	12.46	2.11	1.95	1.3	0.62	0.47	***0.32***	***0.60***	***0.40***
A	BR-90-327	59.69	18.08	5.62	7.26	2.94	2.49	2.63	0.86	0.43	***0.44***	***0.56***	***0.44***
B	BR-85-308	57.70	15.42	8.58	9.51	3.42	3.61	1.00	0.94	0.35	***0.29***	***0.53***	***0.47***
C	BR-85-275	61.50	16.12	6.97	8.27	2.05	1.90	1.55	1.11	0.52	***0.41***	***0.54***	***0.46***
C	BR-85-325	58.19	18.73	7.76	9.32	1.91	1.68	0.77	0.97	0.66	***0.46***	***0.55***	***0.45***
D	DL-85-96	55.58	14.49	8.68	14.61	1.24	2.58	1.98	0.54	0.30	***0.27***	***0.63***	***0.37***
E	BR-85-621	48.11	20.19	6.18	14.62	6.38	2.29	0.97	0.71	0.54	***0.34***	***0.70***	***0.30***
Tettellar & Indares 2007													
Regional Metm. Only	TL01-146d	61.55	18.48	3.23	8.76	1.66	1.92	3.28	0.75	0.15	***0.49***	***0.73***	***0.27***
Regional Metm. Only	TL-146H	60.42	16.68	5.54	9.49	2.63	1.93	2.65	0.66	unknown	***0.39***	***0.63***	***0.37***
Aureoles	TL02-73	60.04	17.28	7.34	9.47	0.85	1.72	2.79	0.51	unknown	***0.41***	***0.56***	***0.44***
Aureoles	TL02-74	57.37	18.12	7.89	9.10	2.87	2.77	1.40	0.47	unknown	***0.39***	***0.54***	***0.46***
Screens	TL02-29	56.03	14.63	7.72	11.58	3.79	3.30	1.95	1.00	unknown	***0.22***	***0.60***	***0.40***
Screens	TL02-44	68.76	10.31	4.46	10.08	1.91	1.76	2.25	0.48	unknown	***0.23***	***0.69***	***0.31***

CHAPTER 3: INTERPRETATION OF TEXTURES

3.1 Summary of Observed Textures

The five sample types display marked mineralogical and textural differences but also some similarities (see summary of petrology in Table 2-1). Sample types A (BR-02-35, BR-90-327), B (BR-85-308) and C (BR-85-275, BR-85-325) share several common features, whereas sample types D and E are more distinct. The most common feature in all sample types and textural domains is the presence of biotite and ilmenite. Ilmenite locally has a biotite corona with or without very fine-grained Bt–Qtz symplectic rims.

Common features in sample types A, B and C are:

(i) elongate Spl–Crd domains which have a monomineralic rim of cordierite (see Figures 2-1C, 2-2D, 2-3C, 2-8B);

(ii) Pl–Opx domains which only vary based on their shape and associations; and

(iii) (quartzo)feldspathic material, which in type A samples are concentrated into specific domains with mineralogical zoning of K-feldspar at the center and plagioclase along the rims and in type C samples are localized in interstitial narrow zones.

In addition, types A and B samples contain Opx–Crd domains varying only in their shape (see Figures 2-1A, 2-2B, 2-3A,B) and show a close association with Pl–Crd domains in type A samples (see Figures 2-2C, 2-4A).

Distinctive features in Type C samples are:

(i) Fine- and coarse-grained domains of Ksp–Qtz–Crd–Opx, with the latter locally crosscutting the other domains (see Figures 2-10, 2-11); and

(ii) rounded Pl–Crd domains not associated with Opx–Crd domains.

In addition, this type contains geometric Crd–Qtz symplectites (of the same type observed in type A sample BR-02-35; see Figures 2-5, 2-15, 2-16).

All three sample types have fine scale microstructures involving quartzofeldspathic minerals, primarily xenomorphic or interstitial monomineralic pockets and in-filling of pods and cracks in coarser minerals (see Figures 2-6, 2-9, 2-17). In addition, types A and B samples contain fine-grained rims of plagioclase against K-feldspar and/or fine-grained rims of ternary feldspar against cordierite; and sample type A contains euhedral cordierite surrounded by xenomorphic pockets of K-feldspar.

Sample type D is characterized by (see Figure 2-18):

(i) quartzofeldspathic domains dominated by mortar-textured K-feldspar with regions rich in quartz and plagioclase (see Figure 2-19C, 2-20A,B);

(ii) large rounded domains having a Fa–Crd intergrowth at the core and an Opx–Crd intergrowth around the rim (similar to Opx–Crd domains observed in sample types A and B; see Figure 2-19A,B); and

(iii) coarse sillimanite, locally with fine-grained coronae of Spl–Pl and Spl–Crd intergrowths, all rimmed by plagioclase (see Figure 2-20C,D).

This type also has the highest bulk X_{Fe} of the pelitic sample types.

Sample type E is distinct; primarily in its chemistry with very high CaO values, but also in its textural and mineralogical make-up. Similar to the other samples this type does contain feldspathic domains, however this domain is quartz-free and dominated by plagioclase with some scattered Opx throughout. Textures specific to this sample type include:

(i) large garnetiferous domains with complex microstructures involving spinel, orthopyroxene, garnet, biotite and plagioclase (see Figure 2-23);

(ii) amoeboid and formfitting Spl–Pl domains, similar to, but less planar than the Spl–Crd domains observed in sample types A,B and C and with An-rich plagioclase instead of Crd (see Figure 2-22); and

(iii) an isolated coarse-grained Ksp–Qtz–Opx domain (see Figure 2-21).

Some fine scale microstructures involving feldspars are similar to those observed in sample types A,B and C, including interstitial pockets of K-feldspar, fine rims of plagioclase or Pl–Qtz symplectites and plagioclase in-filling fractures in coarse K-feldspar.

Previous work (as discussed in Section 1.4.2) has shown that the different mineral associations and textural domains inherited from the contact metamorphism in the NPS aureoles were largely controlled by the coarse-grained and relatively dry regional metamorphic assemblage. Evidence for partial melting has also been found within the contact aureoles of the NPS by Tettelaar (2004) and Tettelaar and Indares (2007). The following section focuses mainly on:

(a) making links between the textural domains and mineral assemblages which formed during the contact metamorphism and those which formed during the regional metamorphism, based on the transitional transformation of porphyroblasts across aureoles, in areas where full aureoles are preserved (outside this study area, see Section 1.4.2); and

(b) textural evidence for partial melting during contact metamorphism; by comparison with pristine melt-related textures described and illustrated in the literature (see Section 1.6.2).

3.2 Sample Types A, B and C

3.2.1 Textural Domains Inherited From the Regional Metamorphism

Lee (1987) and Tettelaar and Indares (2007) observed a progressive transformation of sillimanite porphyroblasts that formed during regional metamorphism, to coronae and pseudomorphs of Spl–Crd symplectites surrounded by monomineralic rims of cordierite (see Figure 3-1). This progressive transformation as well as the elongate shape (see Figures 2-1C, 2-2D, 2-3C, 2-8B) give grounds for interpretation of the **Spl–Crd domains** as pseudomorphs after sillimanite in accordance with a two step reaction which also involved garnet, as inferred by Tettelaar and Indares (2007; see also White *et al.*, 2003). The cordierite rim is consistent with the continuous NaCKFMASH reaction [R1], which isolated the garnet and sillimanite from the surrounding matrix (Tettelaar & Indares, 2007; see Section 2.3.2.3 below for discussion on evidence for partial melting).

[R1] Grt + Sil + Qtz ± Pl → Crd + Liquid

Isolated from the matrix quartz, the garnet and sillimanite would react to form cordierite and spinel, consistent with the FMAS reaction [R2] (Tettelaar & Indares, 2007).

[R2] Grt + Sil → Crd + Spl

Lee (1987) and Tettelaar and Indares (2007) also observed a progressive transformation of garnet porphyroblasts, formed during regional metamorphism, to coronae of Opx–Crd symplectites and Opx–Crd pseudomorphs (see Figure 3-1). This progressive transformation, along with the rounded shape (see Figures 2-1A, 2-2B, 2-3A,B) of the **Opx–Crd domains**, supports the interpretation of these domains as pseudomorphs after garnet. Coarse orthopyroxene atolls and Opx–Crd symplectites along the rims of these domains are consistent with the reaction [R3] as inferred by Tettelaar and Indares (2007), based on the NaCKFMASH petrogenetic grid by Spear *et al.* (1999).

[R3] Grt + Bt + Qtz ± Pl → Crd + Opx + Ksp + Liquid

Evidence for the melt produced in this reaction is seen throughout these sample types and is discussed in Section 2.3.2.3. The radial symplectites in the center of these domains are consistent with [R4], which may occur once biotite has been consumed in the center of garnet domains that have been isolated from the matrix by [R3].

[R4] Grt + Qtz → Opx + Crd

Pl–Crd symplectites surrounding the Opx–Crd domains or forming rounded domains (see Figures 2-2C, 2-4A) are also interpreted to be linked to the breakdown of garnet based on this association and their rounded shape. Decreases in the X_{Fe} from core to rim within the cordierite in this domain are likely derived from former Fe-zoning in the garnet. Coarse plagioclase and Pl–Crd symplectites which flank Opx–Crd domains retain the shape of minerals originally formed in pressure shadows around garnet porphyroblasts, during regional metamorphism, based on their textural association with respect to Opx–Crd domains (garnet pseudomorphs).

Intergrown orthopyroxene and plagioclase within the **Opx–Pl domains** is observed throughout all three sample types, but particularly in rounded subdomains in Type B, and is consistent with reaction [R5] (Martignole & Martelat, 2003), in the absence of biotite.

[R5] Grt + Qtz → Opx + Pl

However, the large volume of plagioclase in this sample which is not in rounded subdomains, is not explained by the breakdown of garnet and quartz and is thus likely a remnant of matrix material formed during the regional metamorphism (see discussion of quartzofeldspathic material below). Orthopyroxene associated with this plagioclase may have originated by diffusion of Fe and Mg from nearby garnet breakdown. This diffusion pattern could also explain the Opx–Pl rims around rounded Opx–Crd domains in Type A samples.

According to Tettelaar (2004) and Tettelaar and Indares (2007), the quartzofeldspathic matrix formed during the regional metamorphism, in rocks contained in the MLP aureole, was generally fine-grained and progressively increased in grain size towards the interior of the aureole. Similarly, the **quartzofeldspathic domains** in sample types A and B are likely remnant from the quartzofeldspathic matrix observed in the regional assemblage, which has undergone coarsening during contact metamorphism. In addition, perthitic and anti-perthitic feldspars (see Figure 2-9A) give evidence for slow un-mixing or adjustments during contact metamorphism.

These quartzofeldspathic domains are mineralogically zoned with K-feldspar at the center and plagioclase at the rim (see Figures 2-2, 2-8 for best examples). The same mineralogical zonation is observed within regionally metamorphosed samples from Tettelaar and Indares (2007). This is illustrated in the mineralogical map of thin section TL01-146H from their study (see Figure 3-2). This type of mineralogical zonation with plagioclase separating Al-rich phases, such as aluminosilicates, from K-feldspar, has also been observed in other studies (O'Brien & Roetzler, 2003; Baldwin *et al.*, 2007; Guilmette *et al.*, 2010 and modeled by Stipska *et al.*, 2010) which attributed it to an Al-Si gradient between the Al-rich phases and the surrounding matrix. This organization of feldspars in the samples investigated here is thus likely remnant of this type of elemental diffusion which acted on nearby garnet and sillimanite porphyroblasts during the regional metamorphism.

The coarse **foliation,** formed during the regional assemblage, is preserved locally where the matrix and the Spl–Crd (sillimanite pseudomorphs) domains wrap around Opx–Crd (garnet pseudomorphs) domains (see Figure 2-2B).

The interwoven arrangement of the domains in type B sample BR-85-308 can be closely correlated to the arrangement of the regional mineral assemblage in sample TL01-146H, in which garnet and sillimanite form a single textural domain (see Figures 2-8, 3-2). This sample displays large elongate regions of coarse garnet porphyroblasts with interstitial coarse sillimanite alternating with regions having medium- to coarse-grained rounded garnets, which are both rimmed by plagioclase in a quartzofeldspathic matrix. In type B sample BR-85-308, Crd-rich domains are interpreted as elongate coarse garnet pseudomorphs (Opx–Crd) with interstitial sillimanite pseudomorphs (Spl–Crd). This Crd-rich domain is rimmed by Pl-rich domains, with Opx interpreted to be the result of Fe-Mg diffusion from the nearby garnet and rounded Opx–Pl domains interpreted as pseudomorphs after garnet. The coarse K-feldspar pods and a large part of the surrounding plagioclase are likely remnant from the matrix formed during regional metamorphism.

3.2.2 Textures Limited to Sample Type C

Fine-grained Ksp–Qtz–Crd–Opx domains, observed in type C samples only (see Figures 2-10d, 2-11d, 2-12, 2-13), are interpreted as the breakdown products after **osumilite,** consistent with the reaction [R6] (Spear *et al.,* 1999, see Section 1.6.3 for further discussion).

[R6] Osm ± Liquid → Ksp + Qtz + Crd + Opx

This same microstructure has been observed as coronae around osumilite in samples collected within the Nain region by J. Berg (see Figure 1-9). Due to the subrounded shape of these domains, it is possible that osumilite represents pseudomorphs after:

(a) garnet porphyroblasts from the regional assemblage; or

(b) Opx–Crd domains formed during an earlier pulse of contact metamorphism as pseudomorphs after garnet by [R3] and [R4], supported by the lack of rounded Opx–Crd domains in type C samples.

In addition, **Ksp–Pl symplectic coronae** around the fine-grained Ksp–Qtz–Crd–Opx domains (see Figure 2-12, 2-13) are interpreted to have crystallized from melt permeating from osumilite grain boundaries (see Section 1.6.2).

Coarse-grained Ksp–Qtz–Crd–Opx domains, observed in sample type C only (see Figures 2-10F, 2-11E, 2-14), are inferred, based on their cross-cutting relationship with the adjacent layers in BR-85-325, to represent coalesced, partly migrated, former melt-bearing domains. Coarse-grained quartz, orthopyroxene and K-feldspar is inferred to represent a pyroxene-bearing coalesced former melt. A similar interpretation may be valid for the **isolated coarse-grained Opx–Qtz domain** (sample type A, sample BR-90-327; see Figures 2-2F, 2-4B). Coarse, corroded, **perthitic K-feldspar** grains are interpreted as remnant matrix K-feldspar from the regional assemblage which have been corroded by contact with the melt.

3.2.3 Other Textures Related to Partial Melting

Sample types A, B and C also contain a wide range of fine scale textures that may be attributed to partial melting:

(i) Interstitial monomineralic **xenomorphic pockets** of feldspars and quartz are interpreted as pseudomorphs after melt (similar to microstructures discussed by Holness & Sawyer, 2008 and Holness *et al.,* 2011; see Section 1.4.2; see Figure 2-6A,C, 2-9B,C, 2-17). These former melt pockets represent the final pocket in which the melt crystallized and are pseudomorphed by the phase which had the greatest difficulty nucleating (Holness, 2008; Holness *et al.,* 2011). The dihedral angles in the corners of these pockets are lower than those expected for solid state mineral growth and likely represent the dihedral angles reminiscent of the melt-solid interface (Holness *et al.*, 2011). The surrounding rounded plagioclase grains give evidence that the dihedral angle is, however, progressively increasing towards that of solid-state equilibrium (Holness *et al.*, 2011);;

(ii) **Euhedral cordierite** within xenomorphic K-feldspar is interpreted as a peritectic phase crystallized within melt (see Figure 2-6D);

(iii) Thin **films** of albite-rich plagioclase represent the first composition crystallized from melt (see Figure 2-7);

(iv) **Fractures** within coarse perthitic K-feldspars are likely due to magmatic over-pressure due to the production of melt during contact metamorphism and were thus filled by melt and later pseudomorphed by plagioclase, Pl–Qtz symplectites and quartz (see Figure 2-6B, 2-9D, 2-17B); and

(v) **Bt–Qtz** symplectites rimming biotite coronae around ilmenite, similar to microstructures discussed by Waters (2001) are inferred as the product of melt crystallized during retrogression.

In addition, the fine- to coarse-grained **geometric Crd–Qtz intergrowths**, observed in types A and C samples only (see Figures 2-5, 2-15, 2-16), are consistent with the synchronous combination of reactions [R7] and [R8] inferred by Barbey *et al.* (1999) and Barbey (2003) for melt-present assemblages, as supported by the textures related to partial melting discussed above.

[R7] Bt + Melt1 → Crd + Melt2

[R8] Ksp + Pl + Melt2 → Qtz + Melt3

According to this interpretation, biotite, isolated from domains of garnet breakdown, would react in the presence of melt (M1), by [R7], producing cordierite together with an Al-poor and thus unstable melt (M2). Simultaneously, in order to adjust the composition of this melt, nearby feldspars dissolve by [R8] This leads to an excess of silica in the melt (M3) and promotes the crystallization of quartz. This interpretation accounts for both simultaneous crystallization of cordierite and quartz to form fine-grained more rounded symplectites while also allowing for the crystallization of minerals from and in the presence of melt, forming straight and euhedral grain boundaries. This combination would produce the geometric symplectite.

3.3 Sample Types D and E

In contrast to sample types A, B and C, sample types D and E have distinct mineralogies, the progressive development of which has not been observed in other aureoles in this region. The most distinctive features of type D samples are the presence of Fa-rich and Sil-rich domains (see Figure 2-18). The shape and ferromagnesian composition of the **Fa-rich** domains, implies the replacement of a singular ferromagnesian porphyroblastic phase and bears some similarity with the Opx–Crd domains, interpreted as pseudomorphs after garnet, in sample types A and B. The Fa-rich domains in type D samples are rimmed by Opx–Crd intergrowths, surrounded by orthopyroxene atolls (see Figure 2-19A,B), which are consistent with the reactions [R3] and [R4]. The fayalite at the core of the domain was likely formed as a replacement of orthopyroxene. In this context, spinel inclusions in fayalite are likely due to the excess of aluminum induced by the formation of an Al-free mineral (i.e. fayalite) in the orthopyroxene site.

K-feldspar and An-rich plagioclase in contact with the fayalite-rich domains are likely pseudomorphs after former melt, allowing for the crystallization of the acicular orthopyroxene atoll. In contrast, quartz in contact with these domains likely formed during solid-state reactions, limiting the adjacent orthopyroxene atoll to a granular habit. Rounded quartz inclusions within the K-feldspar mentioned above are likely remnant from the regional metamorphic assemblage.

Sil-rich domains are rimmed by **Spl–Pl** (calcic plagioclase) or **Spl–Crd** (see Figure 2-20D), which gives supporting evidence for the Spl–Pl and Spl–Crd pseudomorphs forming after sillimanite observed in other sample types discussed above. Coarse perthitic ternary K-feldspar in the **matrix** is a remnant of the regional K-feldspar, similar to that discussed above in sample types A, B and C, and contains fractures infilled with plagioclase pseudomorphs after former melt. **Xenomorphic K-feldspar** in the matrix (see Figure 2-20B) is compositionally close to ternary-orthoclase and are primarily surrounded by rounded plagioclase grains. These xenomorphic K-feldspar grains are interpreted as pseudomorphs after former melt pockets.

Sample type D is chemically similar to the paragneiss screens observed by Tettelaar and Indares (2007; as discussed above), but has a different mineralogy. The screens documented by Tettelaar and Indares (2007) are sillimanite-absent, quartz-poor and rich in spinel and biotite, whereas type D samples contain sillimanite and abundant quartz within the quartzofeldspathic domain, but are poor in biotite and spinel. The only textural similarity is the partial replacement of garnet by a Spl±Crd±Opx symplectic rim, which is similar to the Opx–Crd and Spl–Crd–Opx–Pl intergrowths surrounding the fayalite-rich domains, interpreted as pseudomorphs after garnet.

Type E samples are chemically distinct and consist of garnetiferous domains and Spl–Pl domains in a feldspathic matrix (see Figure 2-21). **Spl–Pl** domains (see Figure 2-22) are interpreted as sillimanite pseudomorphs representing a more advanced stage in the transformation of sillimanite than the Spl–Pl coronae observed in sample type D. **Garnetiferous domains** (see Figure 2-23) are likely pseudomorphs after garnet porphyroblasts formed during the Paleoproterozoic regional metamorphism and represent the only domains where garnet grew during contact metamorphism. The regional metamorphic protolith was likely quartz-free and was composed of a **feldspathic matrix**, which is preserved in this assemblage. Similar to other sample types, pockets of **xenomorphic K-feldspar** (see Figure 2-24B) are interpreted as pseudomorphs after former melt. The **coarse-grained Ksp–Qtz–Opx** domain (see Figure 2-21C) may represent a pocket of a pyroxene-bearing former melt.

3.4 Textural and Chemical Evidence for UHT Conditions

Round to elongate domains of fine-grained symplectic intergrowths of **Crd–Opx–Qtz–Ksp** within type C samples likely represent the breakdown of the UHT mineral **osumilite** (see Section 1.4.3; Carrington & Harley 1995; Kelsey, 2008). Several other typical textures observed in UHT assemblages, as described by Kelsey (2008), are observed in some samples within this study. These include:

(i) **Spl and Crd replacing Sil** in the presence of melt (Type A, B, C and D),

(ii) **Crd and Opx replacing Grt** in the presence of melt (Type A, B, C and D),

(iii) Spl and Qtz isolated by a Crd rim (Type A, C and D),

(iv) Spl and Opx replacing Grt (Type E),

(v) Grt and Opx (Type E),

(vi) Crn and Qtz (Type A, B and C).

Many UHT terrains have also reported **high-Al orthopyroxene** with y(opx) = 0.08 to >0.14 (Kelsey, 2008; McFarlane *et al.,* 2003; [y(opx) = number of Al6 cations in orthopyroxene]). Aranovich and Berman (1997) have developed a Grt–Opx thermometer which utilizes the solubility of Al in orthopyroxene. This is used for thermobarometry on sample BR-85-621 (see Section 3.2 below) because it contains orthopyroxene and garnet which appear to have formed together. However, most of the samples in this study do not contain garnet and orthopyroxene in equilibrium, which inhibits the traditional use of this thermobarometer. It is important to note that these samples do contain similarly high-Al orthopyroxenes as observed in previous studies (see Table 2-5). Type D sample DL-85-96 contains the highest y(opx) up to 0.20 at the core of the fayalite-rich domains. Type A, B and C samples have y(opx) = 0.10–0.12 and type E sample BR-85-621 has the lowest y(opx) = 0.07, but was likely formed with garnet and is discussed further in the following section. The samples in this study are all within the range of Al-content typical of UHT metamorphism.

There are many textures and minerals within these samples which are similar to those observed in known UHT terranes, making these contact aureoles good candidates for UHT contact metamorphism. In the next section the use of Ti-in-Qtz and Grt–Opx thermometry will be discussed in order to better constrain the temperature and pressure ranges of these assemblages.

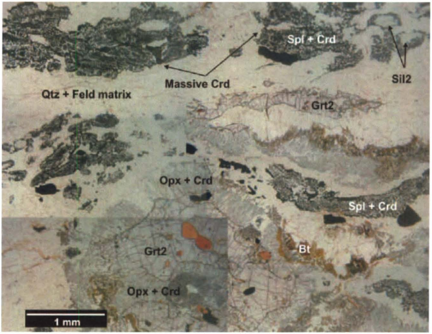

Figure 3-1. Photomicrograph of progressive transformation of Grt and Sill to Opx-Crd and Spl-Crd respectively (photo of sample TL02-77 from Tettelaar and Indares 2007; note that notation of Sil2 and Grt2 do not pertain to this study)

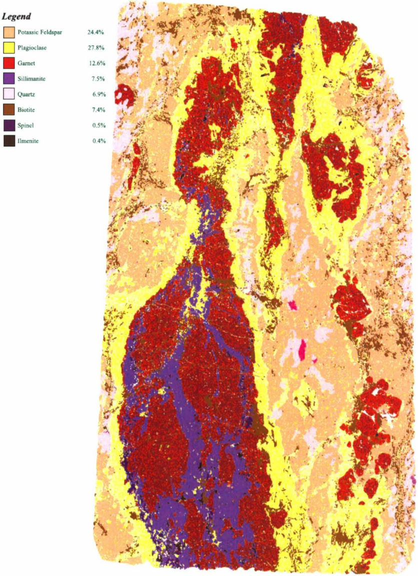

Figure 3-2. Mineralogical map of TL01-146H (this sample is part of a regional metamorphic subset investigated by Tettelaar and Indares 2007)

CHAPTER 4: Thermobarometry

4.1 Titanium in Quartz Thermobarometry

4.1.1 Introduction

The Titani-Q thermobarometer uses the relationship between the amount of titanium measured in quartz (expressed as $X^{qtz}{}_{Ti}$), and the activity of the system with respect to a coexisting TiO_2 mineral phase (rutile, ilmenite) to calculate either a temperature or pressure using the following equation, in combination with a second thermobarometer or an estimated pressure or temperature (Thomas *et al.* 2010).

$$\mathbf{R\,T\,ln(X^{qtz}{}_{Ti}) = -60952 + 1.520 \bullet T(K) - 1741 \bullet P(kbar) + R\,T\,ln(a_{TiO_2})}$$

where R = 8.3145 J/K, T = temperature (Kelvins), P = pressure (kbars),

a_{TiO2} = activity of TiO_2 in the system, $X^{qtz}{}_{Ti}$ = fraction of Ti in quartz

This thermobarometer was calibrated using experimental data measured at temperatures of 700–940°C and pressures of 5–20 kbars (Thomas *et al.,* 2010). An estimated pressure of 5 kbars was used for calculations for this study because it falls within both the experimental range used by Thomas *et al.* (2010) and the 3.5–5.5 kbar estimates of pressure for the Nain Plutonic Suite contact aureoles (Lee, 1987). Titanium (ppm) in quartz was analyzed for all quartz-bearing textural domains across all sample types, with the exception of the type B sample, BR-85-308, which is quartz-free.

Temperatures were calculated using the following equation, rearranged from the above equation by Thomas *et al.* (2010):

$$\mathbf{T(^{\circ}C) = \frac{a + cP}{b - R \bullet \ln(X^{qtz}{}_{Ti}) + R \bullet \ln(a_{TiO_2})} - 273.15}$$

where a = 60952 ± 3122, b = 1.520 ± 0.04 and c = 1741 ± 63

Details on the analytical methods used for collection of titanium data are given in Section 1.6.3. Titanium content in quartz ranges from 70–824 ppm. Titanium data and BSE images of the textural setting of spot locations are given in Appendix A.

4.1.2 Application of the Titani-Q Thermobarometer in this Study

Ilmenite, which typically has a_{TiO_2} = <1.0 (Thomas *et al.,* 2010), is the TiO_2-bearing mineral in the investigated rocks. However, the actual a_{TiO_2} value is difficult to determine as it represents the availability of titanium throughout the Qtz-bearing assemblage at the time of quartz crystallization. Individual grains of quartz are generally heterogeneous with respect to titanium content, but there is no general core-to-rim trend of titanium (ppm) values in quartz. There is a marked trend in titanium content (ppm) observed with respect to the proximity of spot analyses in quartz to ilmenite grains, on the order of an increase of ~250ppm (or ~70°C) within a ~1mm scale. This trend may be attributed to:

(i) the effect of diffusion;

(ii) a spatial difference in the activity of the system; or

(iii) a combination of both.

4.1.3 The Role of Diffusion

The diffusion coefficient of titanium in quartz at low temperatures (~150–200°C; geotherm value at 5kbar/~15km depth; Fowler, 2005) is extremely low, on the order of <0.08μm per million years (Cherniak *et al.,* 2007). Using this value, over the 1.2 Ga, history following cooling of the NPS, diffusion of titanium in quartz would have taken place over <100μm (<0.1mm). Therefore we can conclude that post-cooling diffusion does not account for the ~1mm scale trend in variation of titanium content in quartz.

Diffusion rates, however, increase experimentally with increasing temperature. The NPS evolved between 1350 and 1290 Ma (Ryan, 2000). If the analyzed segments of the Tasiuyak gneiss wedged between multiple plutons remained at high temperatures for the whole duration of the pluton emplacement, it is likely that significant diffusion would have occurred during this period. Diffusion rates at 800°C are 0.5mm per million years (Cherniak *et al.,* 2007). Therefore, in this scenario, over the 60 million years of emplacement of the plutons comprising the NPS, titanium would be able to diffuse across a maximum of 30 mm. There is no evidence for diffusion at this scale in the samples examined.

However, if rocks remained at high temperatures for closer to ~2 million years, the observed 1 mm scale gradient would be expected. However, this would be valid only for quartz that crystallized earlier than or at the beginning of this high temperature time period, and not for quartz associated with crystallization of the melt following the contact metamorphism.

Assuming that titanium trends associated with ilmenite are due to diffusion only, a first set of temperatures was calculated, with analyses within 1mm of ilmenite grains being removed from consideration. These temperatures were calculated using an average activity of 0.9, because TiO_2 activities of metapelites with respect to ilmenite are similar to that of rutile-saturated rocks (a=1.0, see Storm & Spear, 2009), but less than 1.0 (Wark & Watson, 2006). This set of data is summarized in Table 4-1 and Figure 4-1 and discussed below.

4.1.4 Potential Spatial Variation of a_{TiO_2} in the System

One alternative explanation of this titanium gradient is the possibility of a spatial variation of the activity of titanium in the system, i.e. the availability of titanium which can be incorporated into quartz throughout the surrounding rock at the time of quartz crystallization. This is a difficult parameter to quantify or spatially record. The rationale behind this interpretation is as follows. Quartz or other minerals crystallize around existing ilmenite grains, so those grains immediately surrounding the ilmenite would have the highest availability of titanium and would functionally cut off or impede the migration of titanium to other minerals in the rock. This would potentially result in the highest activity, near 1.0, immediately adjacent to the ilmenite grain, with activities decreasing farther away. This interpretation is empirical, experimentally untested and hypothetical; however, adjusting activities based on their apparent proximity to ilmenite essentially homogenizes the calculated temperatures within individual grains (see Figure 4-2). It is important to note however that these apparent distances only take into account two dimensions and do not account for any proximity to ilmenite in the third dimension. A second set of temperatures was calculated with this adjustment of the activity to compare and test the effectiveness of this method. This was done using the following activities based on their apparent proximity to ilmenite: <0.1mm → $a_{TiO_2} = 1.00$; 0.1–0.5mm → $a_{TiO_2} = 0.90$; 0.5–1.0mm → $a_{TiO_2} = 0.70$ and >1.0mm → $a_{TiO_2} = 0.50$. These estimations were made by adjusting the activities across the grains showing the clearest titanium gradient, such that temperatures calculated across the grain are equal to that calculated immediately adjacent to ilmenite with an activity of 1.0. These data are summarized in Table 4-2 and Figure 4-3.

The uncertainty involved in the input of an estimated pressure and the inability to directly calculate an activity, dictate that the temperatures calculated using the Titani-Q thermobarometer be used only to investigate general trends in specific textural settings. Uncertainties on temperatures are not cited in the discussion because such uncertainties are irrelevant when compared to the uncertainties associated with the previously mentioned estimations.

4.1.5 Results by Textural Setting and Inferred Origin of Quartz

Quartz grains and their corresponding calculated temperatures have been organized based on their textural setting and inferred origin. In terms of the latter, four main types of quartz are considered:

(a) relict grains from the regional metamorphism;

(b) relict grains from the regional metamorphism which have been recrystallized during the contact metamorphism;

(c) quartz primarily in the Crd–Qtz geometric intergrowths which are inferred to have formed during partial melting during contact metamorphism; and

(d) retrograde quartz, produced by the crystallization of melt and the breakdown of the unstable UHT mineral, osumilite during cooling after contact metamorphism.

Temperatures discussed below represent minimum/maximum and average temperatures (MIN–MAX; **AVE**) for which activities were adjusted based on their apparent proximity to ilmenite. Temperatures calculated based on the assumption of diffusion, as discussed above are noted in italics and in brackets (*MIN/MAX; AVE*).

4.1.5.1 Relict Quartz from the Regional Metamorphism

Quartz grains inferred to be relict from the regional metamorphism are observed in type A and D samples. In type A samples, inferred relict quartz grains occur as inclusions in plagioclase which show corrosion along K-feldspar xenomorphic former melt pockets. In type D samples, rounded grains included in and which show corrosion against K-feldspar xenomorphic former melt pockets are also interpreted as relict grains from the regional metamorphism. These grains give temperatures of 773–808; **802°C**. This temperature range is roughly consistent with granulite-facies conditions, as inferred for the regional metamorphism.

4.1.5.2 Quartz Recrystallized During the Contact Metamorphism

Quartz grains inferred to have recrystallized during the contact metamorphism are xenomorphic and are observed in the quartzofeldspathic domains of type A and D samples and in coarse-grained Ksp–Qtz–Crd–Opx domains in Type C samples. These grains yield temperatures of 789–878; **838°C** (*763–788; 775°C*) in type A samples, 781–831; **809°C** (*709–752; 733°C*) in Type E samples, and 768–981; **905°C** (*777–879; 835°C*) in type C samples, consistent with prograde coarsening and recrystallization observed by Tettelaar (2004; see Section 1.4.1).

4.1.5.3 Quartz Associated with Melt Production during the Contact Metamorphism

Quartz grains in the Crd–Qtz geometric intergrowths are interpreted as being associated with melt-producing reactions during the contact metamorphism, as discussed earlier (see Section 3.2.3) in conjunction with interpretations made by Barbey *et al.* (1999) and Barbey (2003). These yield temperatures of 723–911; **826°C** (*748–820; 777°C*) in type A samples and 759–950; **868°C** (*746–853; 810°C*) in type C samples.

4.1.5.4 Retrograde Quartz Associated with Melt Crystallization Following the Contact Metamorphism

The inferred crystallization of quartz from melt films and pockets and/or as Bt–Qtz symplectic rims along biotite coronae around ilmenite is ubiquitous across all quartz-bearing sample types. Temperatures inferred to represent the crystallization of melt are: 765–915; **835°C** (*779–823; 794°C*) in type A samples; 748–950; **875°C** (*730–854; 817°C*) in type C samples; 794–808; **802°C** (*719–732; 727°C*) in type D samples and 739–954; **812°C** (*701–885; 767°C*) in type E samples. Type C samples also yield cooling temperatures of 642–739; **707°C** from quartz associated with the fine-grained Ksp–Qtz–Crd–Opx breakdown products of the UHT mineral osumilite.

4.1.6 Discussion

The two sets of results, based on diffusion and spatial variations in the activity show similar patterns between different sample sets and between different textural settings. However, the temperatures calculated with varying activities are roughly 50°C higher than those based on the assumption that titanium has diffused. It remains unclear which absolute values are correct based on the large amount of uncertainty involved, thus the main points taken from these data sets are the following general trends and observations (see Figures 4-1 and 4-3):

(i) grains interpreted as regional relics record lower temperatures than quartz related to the contact metamorphism; 770–810°C which is consistent with granulite-facies conditions for the regional metamorphism

(ii) inferred recrystallized regional grains and grains associated with melt production and crystallization record the highest temperatures, primarily between 750 and 980°C (*700–930°C*);

(iii) in general, quartz in type C samples yielded the highest temperature estimates for all textural settings and inferred origins, followed by types A, E and D samples respectively; these ranges overlap with UHT conditions (>900°C, see Section 1.6.3)

(iv) quartz associated with the breakdown of osumilite yields the lowest temperatures, 640–740°C, consistent with the formation of quartz during cooling.

4.2 Grt–Opx Thermometer

The Grt–Opx thermometer used in this study is based on the equilibrium $Fe_3Al_2Si_3O_{12}$ (Alm) = 3 $FeSiO_3$ (Fs) + Al_2O_3 (Ok) from which Fe-Al orthopyroxene can be expressed in terms of components of ferrosilite (Fs) and orthocorundum (Ok; Arranovich & Berman, 1997). Temperatures are calculated using the equations given in Figure 4-4. Figure 4-5 outlines the locations of analyses used for calculation. Table 4-3 gives compositional parameters and calculated temperatures.

Temperatures were calculated for type E sample BR-85-621, using coexisting garnet and orthopyroxene at the rim and the core of an augen-shaped garnetiferous domain. However, it is important to note that the state of equilibrium within this domain is unknown. The origin of this texture is consistent with pseudomorphing of garnet grown during the regional metamorphism.

The rim of the garnetiferous domain yields 769°C and the core yields 799°C. Differences between core and rim temperatures may represent different degrees of resetting during cooling.

4.3 General Discussion

Thermobarometry on metamorphic minerals has traditionally been used for the calculation of peak P–T conditions or the investigation of a specific P–T path through time. The rocks in this study posed a particular challenge as most of the samples lacked equilibrium textures between combinations of minerals which are used in traditional thermobarometers. The presence of coexisting orthopyroxene and garnet in sample BR-85-621 allowed for temperature estimates of 769-799°C however due to a lack of a well understood history or state of equilibrium for the mineral grains used, little conclusion can be drawn from these results in terms of the temperature-time history of these rocks. However, recent advancements made in Ti-in-Qtz thermobarometry (Thomas *et al.*, 2010) allowed us to utilize the large proportion of quartz spreading many different textural settings across these samples. This allowed for multiple temperature estimates throughout the multi-stage history of these samples. Although the results are not as precise and determinant as other thermobarometric studies, these methods allowed us to at least peak at the thermal history of these complex polymetamorphic rocks.

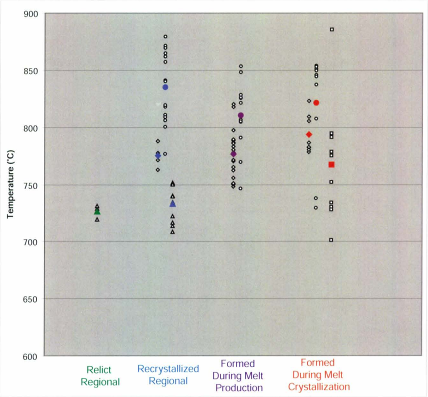

Figure 4-1. TitaniQ temperatures calculated using diffusion-based method. Sample Types: A (diamonds), C (circle), D (triangle) and E (square). Large coloured symbols represent mean temperatures.

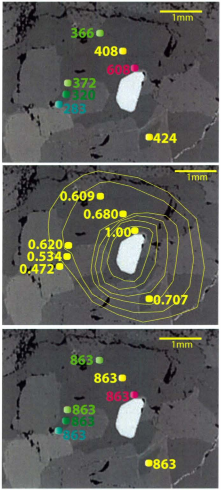

Figure 4-2. Sample BR-02-35. BSE image showing adjustment of activities in order to homogenize calculated temperatures of a single grain; (A) Ti content in quartz (ppm) surrounding Ilm (white grain); (B) chosen activities in order to homogenize temperatures; (C) homogenized temperatures.

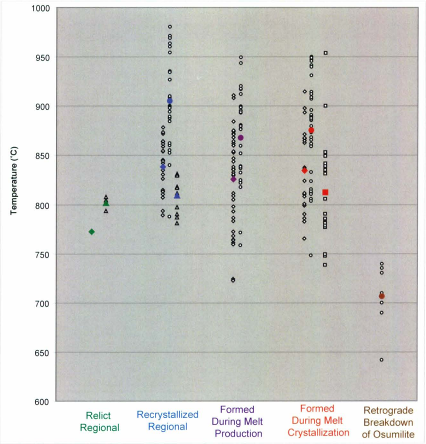

Figure 4-3. TitaniQ temperatures calculated using adjusted aTiO2 for quartz of different inferred origin. Sample types: A (diamonds), C (circle), D (triangle) and E (square). Large coloured symbols represent mean temperatures

$$T(\mathrm{K}) = \frac{-\Delta H_a^0 - 3H_{Fs}^x - H_{Ok}^x + H_{Alm}^x - P(\Delta V_a^0 - 3V_{Fs}^x - V_{Ok}^x + V_{Alm}^x)}{\mathrm{R}\ \ln K_a - \Delta S_a^0 - 3S_{Fs}^x - S_{Ok}^x + S_{Alm}^x}$$

with

$$K_a = \frac{X_{Fs}^3 X_{Ok}}{X_{Alm}^3}.$$

$\Delta H_a^0 = 72767$ J

$\Delta S_a^0 = 16.79$ J/K

$\Delta V_a^0 = 1.58$ J/bar

Ferrosilite (Fs)

$$H^x = -2600x_{En}^2 - 32398.4x_{Ok}^2 - 13120.4x_{En}x_{Ok}$$

$$S^x = -1.342x_{En}^2 - 1.342x_{En}x_{Ok}$$

$$V^x = -0.883x_{Ok}^2 - 0.497x_{En}x_{Ok}$$

Orthocorundum (Ok)

$$H^x = -21878.4x_{En}^2 - 32398.4x_{Fs}^2 - 51676.4x_{En}x_{Fs} + 26534.9x_{Fs}/(x_{Fs} + x_{En})$$

$$S^x = 1.342x_{En}x_{Fs} + 16.111x_{Fs}/(x_{Fs} + x_{En})$$

$$V^x = -0.386x_{En}^2 - 0.883x_{Fs}^2 - 1.269x_{En}x_{Fs} + 0.175x_{Fs}/(x_{Fs} + x_{En})$$

Almandine (Alm)

$$H^x = 5064.5(x_{Py}^2 - 2x_{Py}^2x_{Alm}) + 6249.1(x_{Alm}x_{Py} - 2x_{Py}x_{Alm}^2) - 66940x_{Gr}^2x_{Py} - 136560x_{Gr}x_{Py}^2 + 21951(x_{Gr}^2 - 2x_{Gr}^2x_{Alm}) + 11581.5(x_{Gr}x_{Alm} - 2x_{Gr}x_{Alm}^2) + 73298(x_{Gr}x_{Py} - 2x_{Gr}x_{Py}x_{Alm})$$

$$S^x = 4.11(x_{Py}^2 - 2x_{Py}^2x_{Alm}) + 4.11(x_{Alm}x_{Py} - 2x_{Py}x_{Alm}^2) - 18.79x_{Gr}^2x_{Py} - 18.79x_{Gr}x_{Py}^2 + 9.43(x_{Gr}^2 - 2x_{Gr}^2x_{Alm}) + 9.43(x_{Gr}x_{Alm} - 2x_{Gr}x_{Alm}^2) + 32.33(x_{Gr}x_{Py} - 2x_{Gr}x_{Py}x_{Alm})$$

$$V^x = 0.01(x_{Py}^2 - 2x_{Py}^2x_{Alm}) + 0.06(x_{Alm}x_{Py} - 2x_{Py}x_{Alm}^2) - 0.346x_{Gr}^2x_{Py} - 0.072x_{Gr}x_{Py}^2 + 0.17(x_{Gr}^2 - 2x_{Gr}^2x_{Alm}) + 0.09(x_{Gr}x_{Alm} - 2x_{Gr}x_{Alm}^2) + 0.281(x_{Gr}x_{Py} - 2x_{Gr}x_{Py}x_{Alm})$$

Figure 4-4. Equations used for Grt-Opx thermometer calculations from Arranovich and Berman (1997).

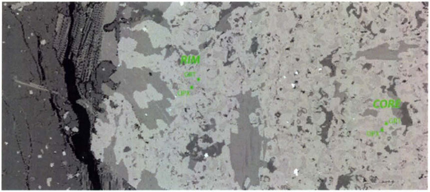

Figure 4-5. BSE image of locations of analyses for calculation of temperature using Grt-Opx thermometer (sample BR-85-621).

Table 4-1. Titanium in quartz minimum, maximum and average temperatures (˚C) of sample types A, C, D and E) with activity of aTiO2 = 0.90, Does not include values taken within 1mm of ilmenite grain. ND = all data collected were within 1mm of ilmenite and could not be used.

Inferred Qtz Types		A	C	D	E
Relict Regional	**MIN**	ND		719	
	MAX	ND		732	
	AVE	*ND*		*727*	
Recrystallized Regional	**MIN**	763	777	709	
	MAX	788	879	752	
	AVE	*775*	*835*	*733*	
Formed During Melt Production	**MIN**	748	746		
	MAX	820	853		
	AVE	*777*	*810*		
Formed During Melt Crystallization	**MIN**	779	730		701
	MAX	823	854		885
	AVE	*794*	*817*		*767*
Formed During Retrograde – Breakdown of Osumilite	**MIN**		ND		
	MAX		ND		
	AVE		*ND*		

Table 4-2. Titanium in quartz minimum, maximum and average temperatures (˚C) of sample types A, C, D and E across TiO2 activities of 0.50, 0.75 and 1.00 for different prograde and retrograde events. Temperatures listed under the "Adj" (=adjusted) activity refers to temperatures which were calculated with an activity based on its proximity to ilmenite (0-0.1mm => 1.0, 0.1-0.5mm => 0.90, 0.5-1.0mm => 0.70 and >1.0mm => 0.50)

Sample Type		Type A					Type C					Type D					Type E				
a_{TiO2}		0.5	0.7	0.9	1	Adj	0.5	0.7	0.9	1	Adj	0.5	0.75	0.9	1	Adj	0.5	0.75	0.9	1	Adj
Relict Regional	MIN	819	773	741	728	773						794	739	719	707	794					
	MAX	819	773	741	728	773						808	784	732	719	808					
	AVE	*819*	*773*	*741*	*728*	773						*802*	*758*	*727*	*714*	802					
Recrystalliz-ed Regional	MIN	844	796	763	750	789	835	788	755	742	788	781	739	709	697	781					
	MAX	992	930	888	872	878	981	921	879	863	981	831	784	752	739	831					
	AVE	*901*	*848*	*811*	*797*	838	*925*	*870*	*832*	*817*	905	*809*	*764*	*732*	*720*	809					
Formed During Melt Production	MIN	766	724	695	683	723	817	772	740	727	759										
	MAX	911	857	820	805	911	977	918	876	860	950										
	AVE	*858*	*809*	*775*	*761*	826	*897*	*845*	*808*	*794*	868										
Formed During Melt Crystallization	MIN	757	716	688	676	688	806	761	730	717	748						749	709	701	670	739
	MAX	915	861	823	808	915	1043	977	932	914	950						971	912	900	855	954
	AVE	*868*	*818*	*783*	*770*	*824*	*928*	*873*	*835*	*819*	875						*836*	*789*	*779*	*743*	812
Retrograde Breakdown of Osumilite	MIN						677	642	617	607	642										
	MAX						783	740	710	698	739										
	AVE						*751*	*711*	*683*	*671*	707										

Table 4.3. Grt-Opx Thermometer compositional values and calculated temperatures.

	X_{Fs}	X_{Ok}	X_{En}	X_{Alm}	X_{Grs}	X_{Py}	Temp °C
Rim	0.468	0.078	0.454	0.750	0.04	0.200	769
Core	0.462	0.095	0.442	0.750	0.04	0.190	799

CHAPTER 5: PHASE EQUILIBRIA MODELING

5.1 Introduction

P–T pseudosections were calculated for the following purposes:

(a) to constrain the peak pressure and temperature conditions for the regional metamorphism using sample TL01-146D from Tettelaar and Indares (2007);

(b) to evaluate the mineral assemblage that was stable at the peak of the regional metamorphism in the 6 contact metamorphosed samples (BR-02-35, BR-90-327, BR-85-308, BR-85-275, BR-85-325 and DL-85-96);

(c) and to compare the topologies within the high to ultra-high temperature-low pressure region of the P–T pseudosection, which corresponds to the P–T field of the contact metamorphism, with the minerals and textures observed.

Purpose (b) provides insight on the 'starting' mineralogy and textures from which the contact phases developed. This will allow for a better understanding of the control that the textural domains inferred to have formed during the regional metamorphism had on the metamorphic reactions, textures and mineral compositions as these textural domains recrystallized during contact metamorphism. Purpose (c) allows for an estimation of the degree of disequilibrium recorded by the samples. It is important to note that reactions which took place during contact metamorphism did so within specific textural micro-domains, which have specific bulk compositions; thus the equilibrium mineral assemblages predicted by P–T pseudosections, calculated with whole rock bulk compositions, will differ from the observed phases in the samples. Bulk compositions of specific microdomains were not used for the calculation of P–T pseudosections for the following reasons:

(a) clear microdomains are difficult to establish in these samples as they are primarily composed of very coarse grained pseudomorphs after previous porphyroblasts within a finer grained, texturally complex matrix; and

(b) even if specific microdomains could be well established, mineral reactions involve diffusion which is not necessarily confined within these microdomains. Therefore the calculated bulk composition for a specific microdomain would not represent the 'effective bulk composition' that would correspond to growth of mineral phases within.

The P–T pseudosections were calculated for the NCKFMASHTO system between 700–1100°C and 3.5–12 kbars using THERMOCALC 3.33 (Holland & Powell, 1998) and the internally consistent data set of Holland and Powell (data file tc-ds55; created in November 2003). The following a-x models were used: biotite (bi: White *et al.,* 2007), silicate melt (liq: White *et al.,* 2007), cordierite (cd: Holland *et al.,* 1998), garnet (g: White *et al.,* 2007), orthopyroxene (opx: White *et al.,* 2002), plagioclase (pl: Holland & Powell, 2003), K-feldspar (ksp: Holland & Powell, 2003), spinel (sp: White *et al.,* 2002), osumilite (osm: Holland *et al.,* 1996) and ilmenite (ilm: White *et al.,* 2000). For information on the calculation of bulk compositions see Section 1.7.4.

5.2 Sample TL01-146D

5.2.1 General Topologies

The P–T pseudosection calculated for sample TL01-146D (see Figure 5-1), which experienced regional metamorphism only, consists of two parts; a simpler high pressure region and a more complex low pressure region. The high pressure region, located above ~7 kbars, consists of topologies involving Grt–Sil–Ksp–Pl–Qtz±Bt ±Liquid and is characterized by two main phase boundaries with steep P/T gradients; the Bt-out line and the solidus, both at ~850°C. These lines are associated with biotite dehydration melting (see Section 1.6.1).

The low pressure region, located below 7 kbars is characterized by complex topologies with the addition of cordierite and orthopyroxene but not biotite. Phase boundaries of ferromagnesian minerals and sillimanite have shallow P/T gradients. The solidus retains its steep P/T gradient but is displaced to ~940°C. Partial melting in this low pressure region is the result of dry melting because there are no hydrous mineral phases stable near the solidus in this region (see Section 1.6.1) and as melt proportions increase, K-feldspar and quartz proportions decrease. Ksp- and Qtz-out lines have steep P/T gradients and are located at ultra-high, >1000°C, temperatures.

5.2.2 P–T Range of Regional Metamorphism

Tettelaar and Indares (2007) observed the mineral assemblage Grt–Sil–Ksp–Pl–Qtz±Bt (plus minor ilmenite and rutile) along with textures related to partial melting in sample TL01-146D. This is consistent with the narrow P–T field between the Bt-out line and solidus. The solidus and Bt-out lines are located at ~850°C and are ~3°C apart. Melt in pelitic rocks is produced primarily by the breakdown of biotite and muscovite (see Section 1.6.1), but the absence of muscovite within the investigated P–T range and the narrowness of this field, implies that significant melt loss from the sample had occurred during the regional metamorphism (White & Powell, 2002; Indares *et al.,* 2008; Guilmette *et al.,* 2010). Down-pressure the solidus and the Bt-out line are limited by the Crd-in line, at ~7.0 kbars.

Melt loss is also consistent with the overall preservation of the peak assemblage and the scarcity of retrograde textures observed in this sample (Tettelaar & Indares, 2007). The remaining melt crystallized at the solidus, causing the observed limited replacement of garnet rims by retrograde biotite and sillimanite, as the rock cooled. Therefore, the overall mineralogy present best represents the last stage of melt crystallization.

Biotite in this sample mainly occurs as a replacement product of garnet rims, and was thus likely absent at the thermal peak. Therefore it is likely that peak metamorphism reached temperatures above the Bt-out line (>850°C). Further constraints can be placed on the P–T conditions by mineral composition isopleths representing the grossular content of garnet. Garnet porphyroblasts in this sample are relatively homogeneous, with little Ca zoning and low grossular contents (~2 mol%; Tettelaar & Indares, 2007). This may be due to garnet growth at a constant grossular content, but is more likely the result of diffusional homogenization of garnet at high temperatures (Indares *et al.*, 2008). As a result, the location of the 2 mol% grossular isopleth in the P–T field up-temperature of the Bt-out line constrains the peak pressure conditions to 8.5–10.5 kbars (see Fig 5-1). In addition, the intersection of this grossular isopleth and the solidus constrains the P–T conditions of melt crystallization to **~8.3 kbars and ~850°C** (see Fig 5-1). These represent the minimum P–T conditions for the regional metamorphism and are consistent with granulite-facies conditions (as inferred by the observed mineral assemblages and melt-related textures).

The predicted modal mineralogy and mineral compositions (in terms of X_{Fe} and X_{Grs} of garnet, X_{An} of plagioclase and X_{Ab} of K-feldspar) for pressures of 7, 8 and 9 kbars, along the solidus and the Bt-out line, are given in Table 5-1. The predicted modal percentages at the P–T conditions of melt crystallization (~8.3 kbars and ~850°C) and the observed modal percentages (see Figure 5-2 for mineralogical map) in the sample are similar (within <10%). Plagioclase shows the most difference, with 9% less plagioclase in the observed assemblage compared to its computed abundance. Measured X_{Fe} and X_{Grs} in garnet and X_{An} in plagioclase are compatible with their predicted values.

5.2.3 Topologies at the P–T Range of the Contact Metamorphism

This P–T pseudosection for the bulk composition of sample TL01-146D also predicts the equilibrium mineral assemblage(s) in the inferred P–T range of the contact metamorphism (~3.5–5.5kbars, 850–1000°C). To the left (down-temperature) of the solidus Crd–Grt–Opx–Ksp–Pl–Qtz–Ilm are stable with garnet becoming unstable at pressures below ~4.3 kbars. To the right (up-temperature) of the solidus, garnet becomes unstable at higher pressures of less than 5kbars. The K-feldspar, quartz and to a lesser extent cordierite proportions decrease as the melt proportion increases with temperature. The melt proportion reaches 30% near the Ksp-out line. The modal mineralogy differs between the solidus and the Ksp-out line at ~4.5kbars and 950–1010°C, with Crd 18→14% Ksp 21→0%, Opx 20%→16%, Pl 20%→22%, Qtz 19%→9 and Liq 0%→37%. The lower temperature mineralogies are most similar to the observed mineralogy of the contact metamorphosed samples of types A, B and C, except for the absence of spinel and the presence of ample quartz.

5.3 Contact Metamorphic Samples

5.3.1 Introduction

P–T pseudosections calculated for the 6 contact metamorphosed samples share some general similarities with each other and with the P–T pseudosection of the regionally metamorphosed-only sample discussed above (see Figures 5-1 to 5-7). The type E sample BR-85-621, is not discussed, because of its rare non-pelitic composition and the large microdomains in the sample, a P–T pseudosection was not calculated. All P–T pseudosections are composed of two main regions: high and low pressure regions (above and below ~6.9–7.8 kbars). Once again, the high pressure region is the simpler and contains topologies involving Grt–Sil–Ksp–Pl–Qtz±Bt±Liq bounded by the steep solidus and Bt-out lines. These lines are important as they represent biotite dehydration melting (see Section 1.6.1). Partial melting occurs at the expense of biotite within the P–T field located between these two lines. This field is narrow (5–12°C wide) and occurs between ~845–898°C (see Figures 5-2 to 5-7). This narrowness is consistent with significant melt loss during the regional metamorphism, as in the case of the regionally metamorphosed sample TL01-146D discussed above, and with the interpretation that these rocks were dry prior to contact metamorphism. The displacement of these phase boundaries up-temperature and up-pressure, when compared to predictions for sample TL01-146D, is a function of the higher bulk X_{Mg} expanding the stability field of cordierite up-pressure and of biotite up-temperature.

The low pressure region is similarly the more complex region of these P–T pseudosections, particularly above the solidus. The topologies in this region lack Bt and involve Crd–Grt–Opx–Ksp–Pl–Qtz–Ilm±Spl. Phase boundaries of ferromagnesian minerals and sillimanite have, in most cases, shallow P/T gradients, whereas Qtz- and Ksp-out lines generally have steep P/T gradients and are located at high (>1000°C) temperatures. Also, as predicted from the regionally metamorphosed-only sample, the solidus in the low pressure region is displaced up-temperature to 900–970°C.

The main differences between the P–T pseudosections calculated for the 6 contact metamorphosed samples are:

(i) the predicted modal mineralogies and mineral compositions for the regional peak;

(ii) the degree of complexity of the low pressure region; and

(iii) the predicted equilibrium assemblages within the P–T range of the contact metamorphism.

It is important to note that the mineralogy, distribution of phases and mineral compositions of the regional metamorphic assemblages are inferred to have exerted a major control on the textural domains and mineral associations developed during the contact metamorphism. These differences are discussed for samples of types A, B, C and D below.

5.3.2 Sample type A

5.3.2.1 BR-02-35

5.3.2.1.1 Mineral Assemblage at the Regional Peak

The predicted modal mineralogy of the regional assemblage is: garnet 44%, sillimanite 8%, plagioclase 21%, K-feldspar 10%, quartz 12% and biotite 4% (see Table 5-1). These match closely the proportions of different domains observed in this sample (see Figure 2-1 for mineralogical map and Figure 5-3 for P–T pseudosection). Opx–Crd domains, interpreted to be the product of Grt–Bt–Qtz, make up ~50% of the rock (see Table 5-2). Predicted garnet, biotite and quartz proportions are consistent with this interpretation, for both garnet and quartz are involved in other mineralogical domains. Similarly Spl–Crd domains, interpreted to be the product of Sil–Grt, make up 15% (see Table 5-2), consistent with the predicted proportion of sillimanite and overlap of the garnet proportions with Opx–Crd domains. The quartzofeldspathic domains, along with other minor domains, make up the other ~35% of this sample (see Table 5-2), consistent with the predicted plagioclase, K-feldspar and overlapping quartz proportions.

Garnet, stable at the regional peak estimated for this bulk composition, has $X_{Fe} = 0.61$ and $X_{Grs} = 0.02$ (see Table 5-1). This X_{Fe} is among the highest in the modeled samples. Predicted X_{An} in plagioclase is within the range of plagioclase analyzed in the quartzofeldspathic domains of this sample ($X_{An} = 0.32$–037). X_{Ab} in the K-feldspar is predicted to be 0.30, ~0.03 higher than that of the analyzed coarse K-feldspar in this domain. This is consistent with the interpretation that the quartzofeldspathic matrix, although having been coarsened and recrystallized during contact metamorphism, is a remnant from the regional metamorphic assemblage.

5.3.2.1.2 Topologies at the PT range of the Contact Metamorphism

Within the high temperature-low pressure region representing the contact metamorphism (~3.5–5.5kbars, 850–1000°C), the topologies predict Grt–Crd–Opx–Ksp–Pl–Qtz–Ilm below the solidus, with garnet becoming unstable at pressures below ~4kbars. Above the solidus (910–950°C), garnet is unstable below ~4.5 kbars and quartz becomes unstable above 930–1000°C. Moving up-temperature at 4.5 kbars from the solidus, crossing the

Qtz-out line and up to the Ksp-out line at 1000°C, predicted modal mineralogies vary as follows: Crd 35→37→31%; Ksp 14→11→0%; Opx 18→24→22%; Pl 20→20→18%; Qtz 3→0→0%; Grt 9→0→0 and Liquid 0→6→28%. The observed modal mineralogies in this sample fall within predictions between the solidus and the Qtz-out line (see Table 5-2), although with ~10% less orthopyroxene and ~8% more cordierite than predicted. This sample has <1% spinel, however, spinel is not stable in the topologies of the investigated P–T range. The presence of this Si-free mineral within micro-domains, isolated by a rim of cordierite leads to an excess of silica outside of the domains, which is consistent with the 4.6% of quartz observed. The melt percentage which can be produced in an equilibrium assemblage reaches 20% in the pressure range of interest. Cordierite, quartz, orthopyroxene and plagioclase proportions decrease, as the melt proportion increases.

5.3.2.2 BR-90-327

5.3.2.2.1 Mineral Assemblage at the Regional Peak

The predicted modal mineralogy of the regional assemblage is: garnet 25%, sillimanite 13%, plagioclase 25%, K-feldspar 24%, quartz 6% and biotite 4% (see Table 5-1). These match closely to the arrangement of different domains observed in this sample (see Figure 2-2 for mineral map and Figure 5-4 for P–T pseudosection). Opx–Crd and Pl–Crd domains, interpreted to be the product of Grt–Bt–Qtz, make up ~21% (see Table 5-2), consistent with the predicted 25% garnet. Spl–Crd domains, interpreted to have formed at the expense of Sil–Grt make up ~26% (see Table 5-2), consistent with the predicted proportion of sillimanite and overlap of the garnet proportions with Opx–Crd domains. The quartzofeldspathic domain, along with other minor domains, makes up the other ~50% of this sample (see Table 5-2), consistent with the sum of the predicted 25% plagioclase, 24% K-feldspar and overlapping quartz proportions. This is consistent with the observed quartzofeldspathic matrix, which contains K-feldspar and plagioclase in roughly equal parts and minor (~1%) quartz, supporting the interpretation that the quartzofeldspathic domain from the regional assemblage was preserved.

Garnet, stable at the regional peak estimated for this bulk composition, has $X_{Fe} = 0.56$ and $X_{Grs} = 0.02$ (see Table 5-1). X_{An} in plagioclase is predicted within the range of plagioclase analyzed in the quartzofeldspathic domains of this sample ($X_{An} = 0.35–0.44$). X_{Ab} in K-feldspar is predicted to be 0.26; ~0.08 higher than X_{Ab} of the analyzed coarse K-feldspar observed in the quartzofeldspathic domains. The minor difference in the X_{Ab} of K-feldspar is consistent with the interpretation that the quartzofeldspathic matrix, although coarsened and recrystallized during contact metamorphism, is remnant from the regional metamorphic assemblage.

5.3.2.2.2 Topologies at the PT range of the Contact Metamorphism

The stable topology within the high temperature-low pressure region representing the contact metamorphism (~3.5–5.5kbars, 850–1000°C) below the solidus is Crd–Grt–Sil–Ksp–Pl–Ilm. This sample (as well as Type B sample BR-85-308, to be discussed in Section 5.3.3.1.2) has low predicted quartz proportions (<10%) in the regional metamorphic assemblage. This produces markedly different topologies in the low-P region of the P–T pseudosection compared to modeled samples with higher predicted quartz proportions. In particular:

(i) quartz is absent in the low-P region of the P–T pseudosection; the Qtz-out line has a shallow P/T gradient;

(ii) sillimanite and garnet are stable up to ultra-high temperatures (1050°C); Grt-out and Sil-out lines have steep P/T gradients; and

(iii) orthopyroxene is absent from all assemblages.

The modal mineralogy along the solidus at 4.5 kbars and 976°C is Crd 29%, Ksp 29%, Grt 13%, Pl 23%, Sil 4% and Ilm 2%. This assemblage is significantly different from the observed mineralogy (see Table 5-2). A better match occurs to the right of the Sil-out and Grt-out lines. The modal mineralogy along the Grt-out line at 4.5 kbars and 1058°C is Crd 26%, Ksp 6%, Pl 17%, Ilm 2% and Liq 49%. The observed modal mineralogy lies somewhere in between these two estimations and contains significantly less evidence for melt, as well as minor spinel, quartz and orthopyroxene. This is evidence for an extremely heterogeneous assemblage, in disequilibrium, controlled by the domainal pseudomorphing of large porphyroblasts of sillimanite and garnet.

5.3.3 Type B

5.3.3.1 BR-85-308

5.3.3.1.1 Mineral Assemblage at the Regional Peak

The predicted modal mineralogy of the regional assemblage is: garnet 36%, sillimanite 5%, plagioclase 44%, K-feldspar 4%, quartz 6% and biotite 3% (see Table 5-1). Based on interpretations and correlations with sample TL01-146H made in Section 2.3.2, observed domains match closely with this predicted modal mineralogy (see Figure 2-8 for mineralogical map and Figure 5-5 for P–T pseudosection). Opx–Crd domains and rounded Pl–Opx domains interpreted as garnet pseudomorphs make up ~40% of the sample (see Table 5-2), similar to the proportion of garnet predicted during the regional metamorphism. Predicted sillimanite is consistent with the ~5% of Spl–Crd domains observed (see Table 5-2). Quartzofeldspathic minerals are predicted to make up ~55%, similar to the combination of K-feldspar pods and the remaining Opx–Pl domains (~55%; see Table 5-2).

Garnet, stable at the regional peak estimated for this bulk composition, has a low X_{Fe} = 0.48 and X_{Grs} = 0.02 (see Table 5-1). This is the lowest estimated X_{Fe} in garnet for all P–T pseudosections, and is in accordance with the low bulk X_{Fe} of this sample (see Tables 5-1, 2-7). X_{An} in plagioclase is predicted to be less calcic (0.29) than the observed plagioclase (0.35–0.39). X_{Ab} in the K-feldspar is predicted to be 0.34; ~0.17 higher than X_{Ab} of the analyzed coarse K-feldspar observed in pods surrounded by Pl–Opx domains.

5.3.3.1.2 Topologies at the PT range of the Contact Metamorphism

The main topology, within the high temperature-low pressure region representing the contact metamorphism (~3.5–5.5kbars, 850–1000°C) below the solidus is Crd–Grt–Opx–Ksp–Pl–Ilm. At 950–1000°C and below 3.5–4.5 kbars, garnet becomes unstable above the solidus and below the Ksp-out line , along the steep P/T gradient, Grt-out line. This sample, as previously mentioned (and similar to sample BR-90-327), has low quartz proportions predicted for the regional metamorphic assemblage. This correlates to markedly different topologies in the low-P region of the P–T pseudosection compared to modeled samples with higher predicted quartz proportions. In particular:

(i) quartz is absent in the low-P region of the P–T pseudosection; Qtz-out line has a shallow P/T gradient; and

(ii) garnet is stable up to ultra-high temperatures (>900°C); Grt-out line has a steep P/T gradient.

The predicted modal mineralogy between the solidus and the Ksp-out line, at 4.5 kbars and 975–1018°C differs as follows: Crd 22→21%, Opx 17→24%, Ksp 5→0%, Pl 45→46%, Grt 8→0% and Liq 0→7%. The estimated assemblage differs from the observed assemblage primarily in terms of cordierite, where the observed assemblage has 12–13% more cordierite, which is not predicted to differ within this field (see Table 5-2). The estimated assemblages during both regional and contact metamorphism suggest that the plagioclase, K-feldspar and ilmenite were roughly constant between these two events and that there was little growth of these minerals during contact metamorphism.

5.3.4 Type C

5.3.4.1 BR-85-275

5.3.4.1.1 Mineral Assemblage at the Regional Peak

The predicted modal mineralogy of the regional assemblage is: garnet 31%, sillimanite 12%, plagioclase 20%, K-feldspar 12%, quartz 18% and biotite 5% (see Table 5-1). It is difficult to correlate the predicted modal percentages with the observed domains due to the complexity of the contact-related textures and domains in this section although some general similarities can be drawn (see Figure 2-10 for mineralogical map and Figure 5-6 for P–T pseudosection). Spl–Crd domains, interpreted as products of Grt–Sil make up ~20% of the sample consistent with the estimated sillimanite proportions (see Table 5-2). Pl–Crd domains and fine-grained Ksp–Qtz–Crd–Opx domains interpreted as products of the breakdown of garnet (or garnet pseudomorphs) make up ~30% of the sample, consistent with the predicted garnet proportions (see Table 5-2).

Garnet, stable at the regional peak estimated for this bulk composition, has $X_{Fe} = 0.55$ and $X_{Grs} = 0.02$ (see Table 5-1). Predicted X_{An} in plagioclase is within the range of plagioclase analyzed throughout the sample ($X_{An} = 0.34$–0.41). X_{Ab} in K-feldspar is predicted to be 0.29.

5.3.4.1.2 Topologies at the PT range of the Contact Metamorphism

Within the high temperature-low pressure region representing the contact metamorphism (~3.5–5.5kbars, 850–1000°C) below the solidus, the topologies contain Crd–Grt–Sil–

Opx–Ksp–Pl–Qtz–Ilm with sillimanite becoming unstable below ~5kbars, orthopyroxene becoming unstable above ~4.2 kbars and Grt becoming unstable below 3.7 kbars. Above the solidus the topologies contain Crd–Grt–Opx–Ksp–Pl–Qtz–Ilm–Liquid with orthopyroxene becoming unstable above 5 kbars and garnet becoming unstable below 4.5 kbars. Quartz and K-feldspar have steep P/T gradients and become unstable at 980–1010°C.

The modal mineralogy predicted at the solidus, crossing the Qtz-out line, up to the Ksp-out line at 4.5 kbars and 942–1006°C, has estimated modal mineralogies of Crd 46→43→42%, Opx 8→6→5%, Pl 19→18→17%, Ksp 17→3→0%, and Qtz 8→0→0% and Liq 0→28→34%. The observed assemblage matches closest between the solidus and the Qtz-out line, but differs slightly with less estimated plagioclase and quartz (see Table 5-2). Pseudomorphs after osumilite are an important characteristic of type C samples; however, osumilite is not stable in this P–T pseudosection. This is consistent with growth within isolated microdomains with effective bulk composition different than the bulk composition of the whole rock. Spinel is not stable in the topologies of the investigated P–T range; however, this sample has ~1% spinel. The presence of the Si-free mineral spinel within microdomains, isolated by a rim of cordierite, leads to an excess of silica outside of this domain. This is consistent with the 10.8% quartz observed. The coarse-grained Ksp–Qtz–Crd–Opx domains (~30%), interpreted as coalesced, partly migrated, former melt-bearing domains, makes up the >30% liquid portion estimated at >1000°C. Thus, ignoring the isolated osumilite pseudomorphs and isolated spinel within the sillimanite pseudomorphs, this mineral estimation is consistent with the remainder of the surrounding matrix containing primarily cordierite with plagioclase, orthopyroxene and ilmenite.

5.3.4.2 BR-85-325

5.3.4.2.1 Mineral Assemblage at the Regional Peak

This P–T pseudosection represents the half of the thin section rich in osumilite pseudomorphs and the coarse-grained Ksp–Qtz–Crd–Opx domain (see Figure 2-11 for mineralogical map and Figure 5-7 for P–T pseudosection). The other half, primarily composed of sillimanite pseudomorphs represents a more isolated layer, previously rich in garnet and sillimanite, likely residuum.

The predicted modal mineralogy of the regional assemblage is: garnet 23%, sillimanite 10%, plagioclase 29%, K-feldspar 9%, quartz 23% and biotite 4% (see Table 5-1). Due to the complexity of the contact-related textures and domains in this section it is difficult to correlate the estimated modal percentages with the observed domains and their interpretations, however some general similarities can be drawn. In this half of the sample ~20% is composed of Spl–Crd domains, interpreted as the product of Grt–Sil (see Table 5-2). This is consistent with the sillimanite predicted for this half of the sample. Pl–Crd domains and fine-grained Ksp–Qtz–Crd–Opx domains, interpreted as products of the breakdown of garnet (or garnet pseudomorphs) make up ~20% of this sample, consistent with the predicted garnet proportion (see Table 5-2).

Garnet, stable at the regional peak estimated for this bulk composition, has $X_{Fe} = 0.55$ and $X_{Grs} = 0.02$ (see Table 5-1). X_{An} in plagioclase is predicted within the range of plagioclase analyzed throughout the sample. X_{Ab} in the K-feldspar is predicted to be 0.29, ~0.04 higher than the most sodic K-feldspar in this sample.

5.3.4.2.2 Topologies at the PT range of the Contact Metamorphism

Within the high temperature-low pressure region representing the contact metamorphism (~3.5–5.5kbars, 850–1100°C), below the solidus, the topologies involve Crd–Grt–Opx–Ksp–Pl–Qtz–Sil–Spl–Ilm with orthopyroxene becoming unstable above 4.2 kbars, sillimanite becoming unstable below 5.2 kbars, spinel becoming unstable below 5 kbars and garnet becoming unstable below 3.8 kbars. The topologies above the solidus, at ~940°C, contain Crd–Grt–Opx–Ksp–Pl–Qtz–Spl–Ilm–Liquid with orthopyroxene becoming unstable above 4.8 kbars and spinel becoming unstable below 4.8 kbars. This is the only sample with both spinel and quartz stable in the topologies of the P–T pseudosection. The Grt-out line has a shallow P/T gradient at ~4.2 kbars up to 970°C and has a steep gradient from 970–1020°C. The Ksp-out line has a steep P/T gradient at ~1000°C and the Qtz-out line has a steep P/T gradient at ~1080°C.

The modal mineralogy at the solidus, crossing the Ksp-out line and up to the Qtz-out line, at 4.5 kbars, and 937–1077°C is Crd 36→34→27%, Pl 28→28→14%, Qtz 14→8→0%, Opx 5→5→<1%, Ksp 12→0→0%, Grt 2→0→0% and Liq 0→23→57%. The estimated assemblage differs from the observed assemblage primarily in the 55.2% observed cordierite (see Table 5-2). As discussed above, pseudomorphs after osumilite are an important characteristic of type C samples; however, osumilite is not stable in the P–T pseudosection. This is consistent with growth within isolated microdomains with effective bulk composition different that the bulk composition of the whole rock. The presence of the Si-free mineral spinel (~4%) within micro-domains, isolated by a rim of cordierite, leads to an excess of silica outside of this domain which is consistent with the ~5.8% quartz observed. The coarse-grained Ksp–Qtz–Crd–Opx domain, interpreted as coalesced, partly migrated, former melt-bearing domains, makes up the 23–57% liquid portion estimated at 991–1100°C. Thus, ignoring the isolated osumilite pseudomorphs and isolated spinel within the sillimanite pseudomorphs, this mineral estimation becomes more consistent with the remainder of the surrounding matrix containing primarily cordierite with plagioclase and minor orthopyroxene and ilmenite.

5.3.5 Type D

5.3.5.1 DL-85-96

5.3.5.1.1 Mineral Assemblage at the Regional Peak

The predicted modal mineralogy of the regional assemblage is: garnet 51%, sillimanite 3%, plagioclase 17%, K-feldspar 22%, quartz 3% and biotite 3% (see Table 5-1). Estimated modal percentages closely match the arrangement of different domains observed in this sample (see Figure 2-18 for mineralogical map and Figure 5-8 for P–T pseudosection). The 5% sillimanite observed in this sample is consistent with the sillimanite predicted for the regional assemblage (see Table 5-2). The Fa-rich domains, interpreted as pseudomorphs after garnet, make up ~50% of the sample, consistent with the predicted garnet (see Table 5-2). The quartzofeldspathic domains make up ~45% of the sample and are consistent with the sum of the Ksp, Pl and Qtz predicted (42%; see Table 5-2).

Garnet stable at the regional peak, estimated for this bulk composition has the highest predicted $X_{Fe} = 0.63$ and the lowest $X_{Grs} = 0.01$ consistent with the highest bulk X_{Fe} (see Table 5-1). Predicted X_{An} in plagioclase is less calcic than the analyzed plagioclase in the quartzofeldspathic domain by ~0.12. X_{Ab} in the K-feldspar is predicted to be 0.39; ~0.17 higher than X_{Ab} of the analyzed coarse K-feldspar observed in the quartzofeldspathic domains.

5.3.5.1.2 Topologies at the PT range of the Contact Metamorphism

The topologies within the high temperature-low pressure region representing the P–T range of the contact metamorphism (~3.5–5.5kbars, 850–1000°C), below the solidus, involve Crd–Grt–Opx–Spl–Ksp–Pl–Ilm with spinel becoming unstable above ~5kbars and garnet becoming unstable below ~4kbars. The topologies above the solidus, contain Crd–Grt–Opx–Spl–Ksp–Pl–Ilm–Liquid with garnet becoming unstable below ~5kbars and K-feldspar becoming unstable at ~1040°C. The topologies in this region, above the solidus, are more complex than in previously discussed P–T pseudosections. The location and arrangement of the Crd-out and Qtz-out lines differ with the Qtz-out line having a shallow P/T gradient at ~5.5kbars and the Crd-out line having a steep P/T gradient at

~980–1070°C. This P–T pseudosection is also the only one to contain topologies where spinel is stable and quartz is not, in contrast to the observed 10.2% quartz and minor 2.5% spinel.

The modal mineralogy between the solidus and the Crd-out line, at 4.5 kbars and 932–1043°C is Crd 18→0%, Opx 34→28%, Ksp 27→1%, Spl 6→12%, Pl 14→15% and Liq 0→44%. This differs from the observed assemblage greatly with the lack of sillimanite and the presence of quartz (see Table 5-2). K-feldspar, spinel, plagioclase, cordierite and ilmenite proportions and the minor evidence for partial melting are most similar to the lower temperature end of the region.

5.3.6 Summary

Phase equilibria modeling predicts similar regional mineral assemblages for all sample types, but with differences in mineral proportions and compositions. For all sample types a regional assemblage of Grt+Sil+Ksp+Pl+Qtz±Bt±Liq bounded by a steep solidus and Bt-out line is predicted in the high-P region of the P–T pseudosections. The low pressure regions of all the calculated P–T pseudosections have the most complex topologies, lack biotite and involve Crd+Grt+Opx+Ksp+Pl+Qtz+Ilm±Spl±Liq. Regarding the regional metamorphism, the field bounded by the solidus and Bt-out line and its narrowness is consistent with biotite dehydration melting and significant melt loss, implying that these rocks which subsequently underwent contact metamorphism would have had anhydrous bulk compositions. This is supported by the high to ultra-high temperature, steep P/T gradients of Ksp-out and Qtz-out lines with the increasing melt proportion up-temperature.

In several cases, the proportion of garnet, sillimanite and quartzofeldspathic minerals closely matches the percentage of specific microdomains inferred to be the pseudomorphing regional metamorphic minerals.

Low quartz proportions predicted for the regional metamorphic assemblage correlate with markedly different low-P region topologies in the two quartz-poor samples (BR-85-308 and BR-90-327). These P–T pseudosections have:

(i) low-P topologies in which quartz is absent and Qtz-out lines have shallow P/T gradients;

(ii) sillimanite and/or garnet are stable up to ultra-high temperatures (900–1050°C) and Sil-out and/or Grt-out lines with steep P/T gradients; and

(iii) a lack of orthopyroxene in all topologies (BR-90-327 only)

Osumilite is not stable within any of the calculated P–T pseudosections. In type C, however, fine-grained Ksp–Qtz–Crd–Opx domains, interpreted as pseudomorphs after osumilite, are observed. The growth of osumilite, interpreted to be pseudomorphs after garnet (or garnet pseudomorphs), and the proportion of these domains is consistent with the predicted proportions of garnet in the regional metamorphic assemblage.

Spinel occurs in the topologies of the P–T pseudosections of only two samples: type C sample BR-85-325 and in type D sample DL-85-96 (which has the highest bulk X_{Fe} of all the samples considered). Type C sample BR-85-325 contains topologies having both spinel and quartz stable, whereas type D sample DL-85-96 contains topologies having spinel, but not quartz, stable. This Si-free mineral is primarily observed within microdomains, isolated by a rim of cordierite. These Si-undersaturated domains lead to an excess of silica outside of these domains which in most samples is consistent with larger than predicted proportions of quartz.

TL01-146D

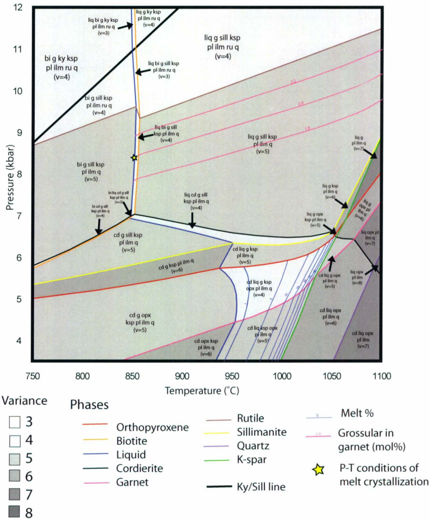

H2O	SiO2	Al2O3	CaO	MgO	FeO	K2O	Na2O	TiO2	O	XFe
0.15	67.75	11.49	1.86	5.31	8.77	1.75	2.57	0.40	0.1	0.73

Figure 5-1. P-T Pseudosection of TL01-146D (sample from Tettelaar & Indares, 2007)

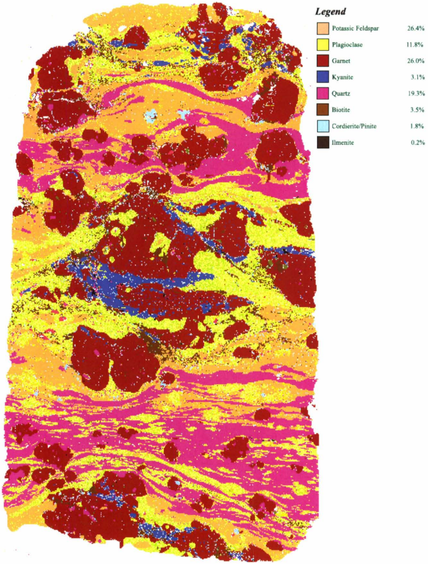

Figure 5-2. Mineralogical map of sample TL01-146D. The petrographic attributes of this sample were investigated by Tettelaar and Indares (2007), and the map shown here was generated from a thin section provided by A. Indares.

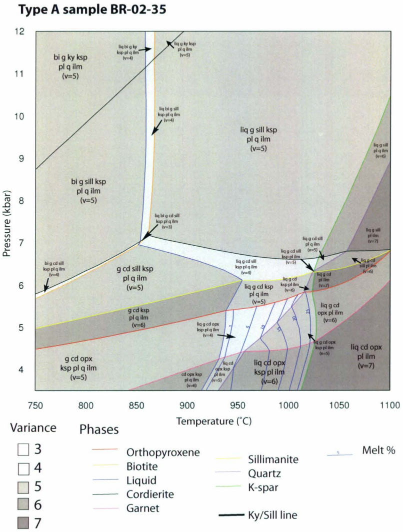

H2O	SiO2	Al2O3	CaO	MgO	FeO	K2O	Na2O	TiO2	O	XFe
0.47	57.63	15.27	2.11	8.18	12.46	1.30	1.95	0.62	0.1	0.60

Figure 5-3. P-T Pseudosection of type A sample BR-02-35

Type A sample BR-90-327

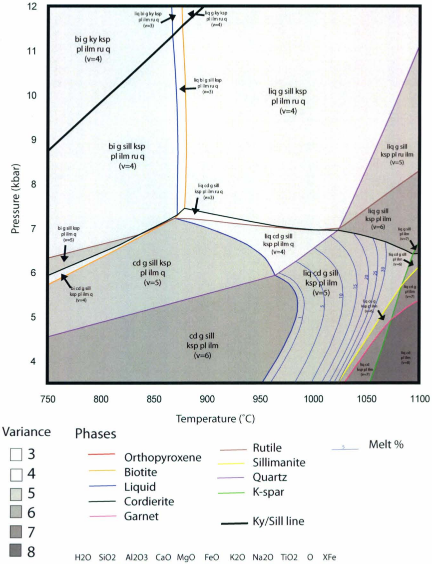

H2O	SiO2	Al2O3	CaO	MgO	FeO	K2O	Na2O	TiO2	O	XFe
0.43	59.69	18.08	2.94	5.62	7.26	2.63	2.49	0.86	0.1	0.56

Figure 5-4. P-T Pseudosection of type A sample BR-90-327

Type B sample BR-85-308

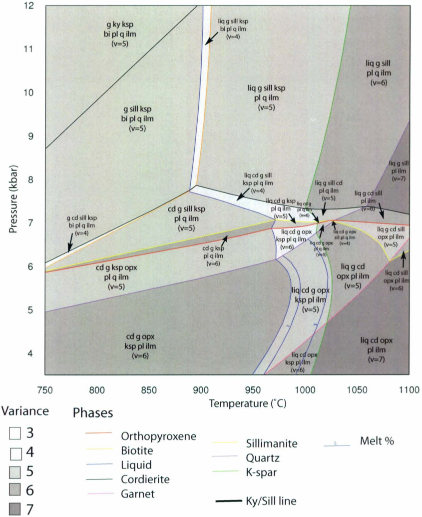

H2O	SiO2	Al2O3	CaO	MgO	FeO	K2O	Na2O	TiO2	O	XFe
0.35	57.70	15.42	3.42	8.58	8.51	1.00	3.61	0.94	0.1	0.53

Figure 5-5. P-T Pseudosection of type B sample BR-85-308

Type C sample BR-85-275

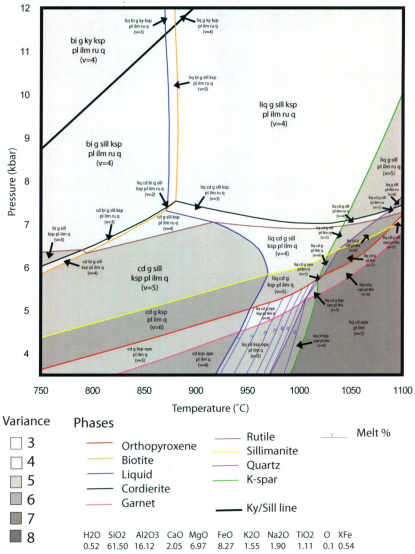

Figure 5-6. P-T Pseudosection of type C sample BR-85-275

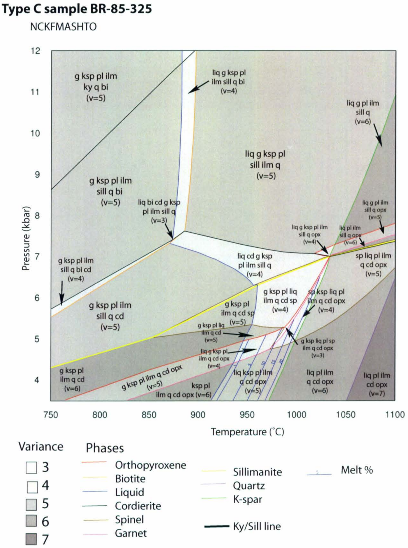

H2O	SiO2	Al2O3	CaO	MgO	FeO	K2O	Na2O	TiO2	O	XFe
0.45	64.83	14.87	2.79	5.42	6.88	1.25	2.43	1.09	0.1	0.55

Figure 5-7. P-T Pseudosection of type C sample BR-85-325. Bulk composition estimated for halfof thin section rich in osumilite-pseudomorphs and coarse grained minerals.

Type D sample DL-85-96

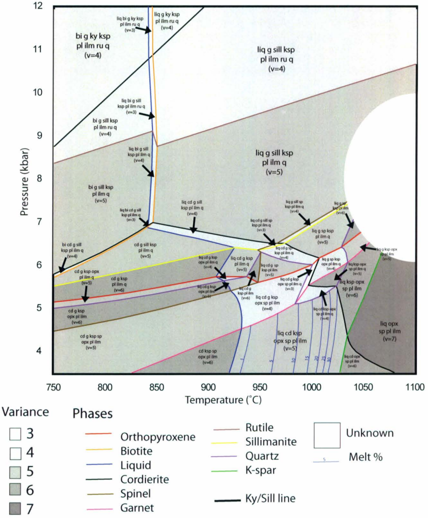

H2O	SiO2	Al2O3	CaO	MgO	FeO	K2O	Na2O	TiO2	O	XFe
0.30	55.58	14.49	1.29	8.68	14.61	1.98	2.58	0.54	0.1	0.63

Figure 5-8. P-T Pseudosection of type D sample DL-85-96.

Table 5-1. Predicted modal mineralogy and mineral compositions based on P-T pseudosections

					Mineral Compositions (molar fractions)				Modal %					
			P	T	X(Grs) in Grt	X(Fe) in Grt	X(An) in Pl	X(Ab) in Ksp	Bt	Grt	Sill	Pl	Ksp	Qtz
Type A	BR-85-35	Solidus	7.00	853.4	0.02	0.61	0.33	0.30	4.31	43.97	7.51	20.88	9.93	12.16
Type A	BR-85-35	Solidus	8.00	856.4	0.02	0.61	0.32	0.30	4.32	44.13	7.60	20.66	9.88	12.18
Type A	BR-85-35	Solidus	9.00	858.1	0.02	0.61	0.32	0.31	4.33	44.32	7.71	20.38	9.83	12.21
Type A	BR-85-35	Bt-Out	7.00	860.4	0.02	0.59	0.35	0.29		46.95	7.01	19.20	11.98	9.95
Type A	BR-85-35	Bt-Out	8.00	863.9	0.02	0.59	0.34	0.29		47.13	7.12	18.95	12.11	10.10
Type A	BR-85-35	Bt-Out	9.00	866.1	0.02	0.59	0.33	0.29		47.33	7.25	18.64	12.23	10.23
Type A	BR-90-327	Solidus	7.00	870.9	0.02	0.56	0.41	0.26	4.04	25.22	12.84	25.34	24.39	6.43
Type A	BR-90-327	Solidus	8.00	875.1	0.02	0.56	0.41	0.26	4.05	25.32	12.90	25.27	24.28	6.45
Type A	BR-90-327	Solidus	9.00	878.0	0.03	0.56	0.40	0.26	4.06	25.44	12.97	25.17	24.17	6.46
Type A	BR-90-327	Bt-Out	7.00	880.5	0.02	0.52	0.42	0.26		27.95	12.33	24.03	25.89	4.24
Type A	BR-90-327	Bt-Out	8.00	885.4	0.02	0.52	0.42	0.26		28.07	12.41	23.94	25.96	4.38
Type A	BR-90-327	Bt-Out	9.00	889.0	0.02	0.52	0.41	0.25		28.20	12.50	23.82	26.01	4.51
Type B	BR-85-308	Solidus	7.00	884.5	0.01	0.48	0.29	0.35	3.40	35.48	4.80	44.11	4.09	6.22
Type B	BR-85-308	Solidus	8.00	890.1	0.01	0.48	0.29	0.34	3.40	35.56	4.84	44.03	4.01	6.23
Type B	BR-85-308	Solidus	9.00	894.5	0.02	0.48	0.29	0.34	3.41	35.67	4.90	43.90	3.96	6.25
Type B	BR-85-308	Bt-Out	7.00	890.0	0.01	0.46	0.30	0.34		37.74	4.34	42.43	5.88	4.41
Type B	BR-85-308	Bt-Out	8.00	895.9	0.01	0.46	0.30	0.34		37.84	4.42	42.36	5.93	4.53
Type B	BR-85-308	Bt-Out	9.00	900.7	0.02	0.46	0.29	0.34		37.96	4.49	42.25	5.97	4.63
Type C	BR-85-275	Solidus	7.00	871.6	0.02	0.55	0.36	0.29	4.90	30.35	12.53	19.86	12.47	18.05
Type C	BR-85-275	Solidus	8.00	873.1	0.02	0.55	0.35	0.29	4.87	31.07	12.45	19.71	12.42	17.90
Type C	BR-85-275	Solidus	9.00	873.5	0.02	0.56	0.34	0.29	4.85	31.59	12.44	19.50	12.39	17.81
Type C	BR-85-275	Bt-Out	7.00	878.4	0.02	0.52	0.38	0.28		34.34	11.76	18.03	14.51	15.27
Type C	BR-85-275	Bt-Out	8.00	880.7	0.02	0.53	0.37	0.28		34.90	11.75	17.86	14.68	15.33
Type C	BR-85-275	Bt-Out	9.00	881.8	0.02	0.53	0.36	0.28		35.36	11.80	17.63	14.82	15.41
Type C	BR-85-325**	Solidus	7.00	871.8	0.02	0.55	0.35	0.30	4.25	23.09	10.11	29.08	8.58	22.70
Type C	BR-85-325**	Solidus	8.00	876.3	0.02	0.55	0.35	0.29	4.26	23.17	10.16	29.02	8.51	22.71
Type C	BR-85-325**	Solidus	9.00	879.5	0.02	0.55	0.35	0.29	4.27	23.26	10.21	28.92	8.44	22.73
Type C	BR-85-325**	Bt-Out	7.00	882.3	0.01	0.51	0.37	0.29		25.96	9.57	27.42	10.43	20.42
Type C	BR-85-325**	Bt-Out	8.00	887.6	0.02	0.51	0.36	0.29		26.05	9.64	27.36	10.52	20.56
Type C	BR-85-325**	Bt-Out	9.00	891.6	0.02	0.51	0.36	0.29		26.16	9.72	27.26	10.59	20.69
Type D	DL-85-96	Solidus	7.00	841.6	0.01	0.63	0.19	0.40	2.72	51.34	3.04	17.11	21.71	2.91
Type D	DL-85-96	Solidus	8.00	844.4	0.01	0.63	0.18	0.39	2.73	51.46	3.11	17.06	21.56	2.93
Type D	DL-85-96	Solidus	9.00	845.4	0.02	0.63	0.17	0.39	2.73	51.59	3.18	16.99	21.40	2.95
Type D	DL-85-96	Bt-Out	7.00	845.6	0.01	0.62	0.20	0.39		53.24	2.73	15.63	23.50	1.59
Type D	DL-85-96	Bt-Out	8.00	848.4	0.01	0.62	0.19	0.39		53.37	2.81	15.51	23.50	1.68
Type D	DL-85-96	Bt-Out	9.00	849.3	0.02	0.62	0.18	0.39		53.67	2.86	15.37	23.48	1.71
Tettelaar and Indares (2007)	TL01-146D	Solidus	7.00	847.9	0.02	0.62	0.28	0.33	1.36	30.96	2.08	22.45	17.94	24.24
Tettelaar and Indares (2007)	TL01-146D	Solidus	8.00	850.9	0.02	0.62	0.27	0.33	1.37	31.06	2.14	22.42	17.80	24.26
Tettelaar and Indares (2007)	TL01-146D	Solidus	9.00	852.6	0.02	0.62	0.26	0.33	1.37	31.18	2.21	22.34	17.66	24.27
Tettelaar and Indares (2007)	TL01-146D	Bt-Out	7.00	851.1	0.02	0.61	0.28	0.33		31.91	1.92	21.83	18.70	23.56
Tettelaar and Indares (2007)	TL01-146D	Bt-Out	8.00	854.3	0.02	0.61	0.27	0.33		32.01	1.99	21.79	18.62	23.61
Tettelaar and Indares (2007)	TL01-146D	Bt-Out	9.00	856.2	0.02	0.61	0.27	0.33		32.14	2.06	21.71	18.53	23.66

** Represents finer grained, spinel poor half of thin section

Table 5-2. Observed modal percentage of minerals and the percentage of textural domains visually estimated from SEM mineralogical maps.

		Observed Modal Minerals									Percentage of Textural Domains		
		Ksp	**Qtz**	**Pl**	**Crd**	**Opx**	**Spl**	**Grt**	**Bt**	**Ilm**	***Grt Pseudomorphs***	***Sill Pseudomorphs***	***Quartzofeldspathic***
A											Opx-Crd	Spl-Crd	Qtzfsp
	BR-02-35	14	5	25	45	11	1	<1	<1	1	50	15	35
											Opx-Crd/Pl-Crd	Spl-Crd	Qtzfsp
	BR-90-327	25	1	41	38	2	3	1	<1	1	21	26	50
B											Opx-Crd/Rounded Opx-Pl	Spl-Crd	Ksp Pods/Opx-Pl
	BR-85-308	10	<1	41	34	13	<1	1	<1	1	40	5	55
C											Pl-Crd/Fine grained Ksp-Qtz-Crd-Opx	Spl-Crd	
	BR-85-275	17	5	25	41	8	1	<1	1	1	30	20	
											Pl-Crd/Fine grained Ksp-Qtz-Crd-Opx	Spl-Crd	
	BR-85-325	11	6	20	56	2	4	<1	1	1	20	20	
D											Fa-Opx-Crd	Sill	Qtzfsp
	DL-85-96	22	10	16	22	15	3	1	1	1	50	5	45

CHAPTER 6: DISCUSSION AND CONCLUSIONS

6.1 Discussion on the Approach of this Study

The Tasiuyak paragneiss adjacent to the NPS displays a rare combination of features as it was metamorphosed under granulite-facies conditions twice, once during regional metamorphism and later during contact metamorphism. Moreover, the portion of the Tasiuyak paragneiss located near the Anaktalik Brook locally lies in direct contact with multiple intrusions. Contact metamorphic mineral assemblages developed in specific micro-domains, controlled by the coarse-grained and anhydrous regional metamorphic assemblage, leading to the formation of complex disequilibrium textures. This contact metamorphism also led to dry partial melting and the development of the UHT mineral osumilite and a wide range of complex microstructures.

Evaluation of the partial melting history of migmatites is an ongoing challenge in the field of metamorphic petrology (see Brown *et al.* 2010), although significant advances have been made in the application of thermobarometry and phase equilibria modeling on migmatites over the past 10 years (e.g., Holland *et al.,* 1996, White and Powell, 2002, Kriegsman and Alvarez-Velero, 2009, White and Powell, 2010, Brown *et al.,* 2010 and references therein). Much of this work has focussed on equilibrium assemblages, whereas melt-producing and melt-consuming reactions commonly form disequilibrium (or reaction) microstructures (symplectites, coronae and partial pseudomorphs, etc; Vernon *et al.* 2008, Kriegsman and Alvarez-Valero 2009) and this heterogeneity makes thermodynamic modeling of these rocks more challenging. The rocks in this study are no exception and contain a multitude of complex, reaction microstructures. This study focussed on detailed documentation of these microstructures and their interpretation based on petrography, relevant thermometric methods and phase equilibria modeling.

The textures were documented using a range of techniques in addition to optical microscopy. This approach was paramount for this thesis, as it allowed for the imaging of complex textures involving colourless minerals such as plagioclase, K-feldspar, quartz and cordierite, the distribution of which is difficult or even impossible to evaluate by 'normal' optical microscopy. The textures at the thin-section scale and the distribution of phases and micro-domains was imaged using an SEM with MLA software. In addition, fine-grained melt-related microstructures and osumilite pseudomorphs were best imaged by cathodoluminescence and BSE imaging.

Even though the use of thermobarometry in this study did not result in a typical quantitative analysis of peak P–T conditions, it allowed for further investigation of the use of the recently published Titani-Q thermobarometer. It also permitted an examination of the effect diffusion and activity coefficients have on calculated temperatures in granulite-facies rocks.

Phase equilibria modeling is traditionally used to evaluate the P–T range of equilibrium mineral assemblages. This approach was not applicable to these samples. Instead phase equilibria modeling was used to address two main issues:

(i) to constrain the precursor regional assemblage in the contact metamorphosed rocks, which allowed for a better understanding of how the regional metamorphic mineral associations and compositions affected the development of different contact metamorphic minerals. Comparison between the modal percentages of minerals predicted by the P–T pseudosections for the regional metamorphic assemblage with a visual estimate of the percentages of different microdomains, inferred to represent pseudomorphs of former regional porphyroblasts, has provided a unique picture of the regional metamorphic assemblage prior to contact metamorphism; and

(ii) to compare the observed mineral associations with the equilibrium mineral assemblages predicted by the P–T pseudosections for the P–T range of contact metamorphism, and thus provide insight into the degree of disequilibrium in the contact metamorphosed samples.

6.2 Summary of the Petrography

Samples collected were subdivided into five different types based textures and mineralogy:

(i) type A samples contain Crd–Pl–Ksp–Qtz–Opx–Spl–Bt–Ilm±Grt and are composed of rounded domains of Opx–Crd intergrowths and elongate domains of Spl–Crd intergrowths interpreted as pseudomorphs after garnet and sillimanite, respectively, and a quartzofeldspathic domain;

(ii) the type B sample contains Crd–Pl–Ksp–Opx–Spl–Ilm–Bt–Grt and is composed of interwoven plagioclase-rich and cordierite-rich domains;

(iii) type C samples are the most complex and contain Crd–Pl–Ksp–Qtz–Opx–Spl–Ilm–Bt–Grt and are composed of elongate Spl–Crd intergrowths interpreted as pseudomorphs after sillimanite, rounded Pl–Crd domains, interstitial Pl–Opx domains, very fine grained intergrowths of Ksp–Qtz–Crd–Opx interpreted as pseudomorphs after osumilite and coarse grained domains of Ksp–Qtz–Crd–Opx, that locally crosscut the rest and are inferred to represent coalesced partly migrated former melt bearing domains;

(iv) the type D sample contains Ksp–Crd–Pl–Opx–Qtz–Fa–Sil–Spl–Bt–Grt–Ilm and are composed of fayalite-rich domains inferred to represent pseudomorphs after garnet and sillimanite-rich domains in a quartzofeldspathic matrix;

(v) the type E sample, which is chemically distinct with a relatively high CaO content, consists of Pl–Grt–Opx–Spl–Ksp–Bt–Qtz–Crd–Ilm and is composed of garnetiferous domains, amoeboid Spl–Pl domains and a coarse grained Ksp–Qtz–Opx domain enclosed in a feldspathic matrix.

Microstructural evidence of partial melting is widespread in all samples and includes:

a. Fine-grained monomineralic xenomorphic pockets of Ksp, Pl or Qtz;
b. Euhedral cordierite within xenomorphic K-feldspar;
c. Thin films of Ab-rich plagioclase;
d. In-filling of fractures in Ksp by Pl, Pl–Qtz symplectites and Qtz;
e. Bt–Qtz symplectites rimming Bt coronae around Ilm; and

f. Very-fine- to medium-grained geometric intergrowth of Crd–Qtz (types A and C samples only).

6.3 Discussion

The rocks, located near Anaktalik Brook (sample Types A, B and C primarily) are a unique and beautiful subset of the contact aureole rocks surrounding the NPS. The progressive transformation of garnet and sillimanite to Opx-Crd and Spl-Crd in this sample set is congruous with observations made in other studies of these contact aureoles (Berg, 1977a; Lee, 1987; Ryan, 1991; MacFarlane *et al.*, 2003; Tettelaar & Indares, 2007); however, what makes these rocks stand out is the multitude of complex microstructures and the extensive evidence for partial melting and UHT conditions. The most marked examples of this are the texturally complex type C samples BR-85-275 and BR-85-325, containing the most extensive evidence for partial melting and the presence of pseudomorphs after the UHT mineral osumilite. This complexity is likely due to the close proximity (<1km) of multiple intrusions (leuconorite and ferrodiorite, see Figure 1-4). Multiple thermal pulses would allow for more heating pulses over a more extended period of time, allowing for the slower and more extensive production of melt and for the overlapping of multiple reaction textures. This is supported by the proposed two-step production of osumilite and the multiple melt-producing reactions observed in these rocks (i.e. melting during the breakdown of garnet and sillimanite and secondly, melting during the production of geometric intergrowths of Crd–Qtz).

The rocks of Anaktalik Brook also bear some similarities with the contact aureoles of the Rogaland anorthosite complex in southwestern Norway (Westphal *et al.,* 2003). The contact aureoles described by Westphal *et al.* (2003) comprise anhydrous charnockitic migmatites with evidence for fluid absent melting of biotite and the presence of osumilite in Ksp–Qtz–Grt–Opx–Crd assemblages. A temperature range of 700–1000°C is estimated for across the contact aureoles. These aureoles are best explained by two thermal pulses or magmatic episodes; the first resulting in a 750–600°C thermal gradient and the second resulting in UHT metamorphism and the production of high temperature minerals such as osumilite (see Westphal *et al.*, 2003 for conductive heating models). A similar model could be applied to the Anaktalik Brook rocks where the transformation of garnet and sillimanite are the result of a first magmatic event and the extensive melting and production of osumilite and Crd-Qtz geometric intergrowths are the result of a second magmatic event. The proximity of mainly one pluton to types A and B samples coupled with the lack of UHT minerals, Crd–Qtz geometric intergrowths (except locally in BR-85-35) and extensive melting would support this model.

Evidence for partial melting during contact metamorphism in the Anaktalik Brook rocks is primarily provided by pristine fine-scaled melt-related microstructures. Evidence for the larger scale coalescence and mobility of melt is however, also observed; primarily the abundance and locally cross-cutting arrangement of coarse grained orthopyroxene-bearing quartzofeldspathic domains throughout types A and C samples.

Type E sample, BR-85-621, is quite distinct, despite being located within the Tasiuyak paragneiss, in the Anaktalik Brook region proximal to both the ferrodiorite and leuconorite (which also surrounds type C samples). Texturally this sample is distinct as it is the only sample which shows production rather than breakdown of garnet. Chemical evidence suggests this sample is derived from an intermediate plutonic rock, which was perhaps emplaced in the Tasiuyak paragneiss.

Finally, the type E sample, DL-85-96, located away from the rest of the sample set, adjacent to the Cabot Lake ferrodiorite intrusion, is distinct in the replacement of orthopyroxene by olivine in the core of garnet pseudomorphs. This replacement was also observed by Lee (1987) elsewhere in the contact aureole along the border of this ferrodiorite intrusion. This unique texture is likely due to the conditions (temperature and timing) of the emplacement of this intrusion because of its correlation with the border of the intrusion and the lack of olivine observed in other NPS contact aureoles.

6.4 Main Conclusions

The following conclusions can be drawn from this study:

(i) Growth of minerals during the contact metamorphism was controlled by the mineral assemblage and microstructures formed during the previous regional metamorphism. This is evident because the textural arrangement of minerals and their textural interpretations in the contact metamorphic rocks can be closely linked with mineral assemblage estimations (based on phase equilibria modeling of bulk compositions) for the regional metamorphism.

(ii) Several lines of evidence suggest that the contact metamorphism near Anaktalik Brook, locally reached UHT conditions. These include:

a. The extensive microstructural evidence for contact-related partial melting, coupled with the predicted location of the solidus at >900°C in the calculated P–T pseudosections;
b. The local presence of pseudomorphs after the UHT mineral osumilite;
c. The temperatures of up to 980°C, estimated by titanium in quartz thermobarometry for the contact metamorphism;
d. The high aluminum content of orthopyroxene;
e. The presence of Zn- and Cr- bearing spinel; and
f. The presence of common UHT textures:
    i. Spl–Qtz isolated by a Crd rim (Type A and C)
    ii. Spl and Opx replacing Grt (Type E)
    iii. Spl and Crd replacing Sil (Type A, B and C)
    iv. Crd and Opx replacing Grt (Type A, B and C)
    v. Grt and Opx (Type E)
    vi. Crn and Qtz (Type A, B and C)

6.5 Future Research

The intricacies of these rocks are numerous and varied and have required a multi-disciplinary approach in order to unfold even a portion of their complex history. This particular and limited sample set has provided many insights into this complex history; however, there is much more to be understood about this region and more specifically about the occurrence of UHT mineral assemblages and partial melting in contact aureoles in general and the effect multiple intrusive events have on those contact aureoles.

The following are suggestions for future research:

(i) Transmission Electron Microscopy (TEM) analysis along grain boundaries within melt-related microstructures to search for quenched melt or microscale minerals which could further the understanding on melt-related reactions

(ii) More extensive titanium in quartz analysis with a more statistically viable data set coupled with an experimental study on the activity coefficients of Ti in rock systems with respect to ilmenite.

(iii) Collection of samples along transects of different contact aureoles to better understand the effect of different and multiple intrusions

(iv) Use of different thermobarometers and sample collection focussed on the use of these thermobarometers

(v) Geochronology of different metamorphic and melt-related events.

REFERENCES

Arranovich, L.Y., and Berman, R.G. 1997. A new garnet-orthopyroxene thermometer based on reversed Al_2O_3 solubility in FeO-Al_2O_3-SiO_2 orthopyroxene. American Mineralogist, 82: 345-353.

Ashwal, L.D. 1993. Anorthosites. Minerals and Rocks Series, 21. Spring-Verlag, Berlin.

Baldwin, J.A., Powell, R., Williams, M.L. and Goncalves, P. 2007. Formation of eclogite, and reaction during exhumation to mid-crustal levels, Snowbird tectonic zone, western Canadian Shield. Journal of Metamorphic Geology. 25: 953-974.

Barbey, P. 2003. Diffusion-controlled biotite breakdown reaction textures at the solid/liquid transition in the continental crust. Contributions to Mineralogy and Petrology. 154: 707-716.

Barbey, P., Marignac, C., Montel, J.M., Macaudiére, J., Gasquet, D., and Jabbori, J. 1999. Cordierite growth textures and the conditions of genesis and emplacement of crustal granitic magmas: the Velay granite complex (Massif Central, France). Journal of Petrology. 40: 1425-1441.

Berg, J.H. 1977a. Dry granulite mineral assemblages in the contact aureoles of the Nain Complex, Labrador. Contributions to Mineralogy and Petrology. 64: 33-52.

Berg, J.H. 1977b. Regional geobarometry in the contact aureoles of the anorthositic Nain Complex, Labrador. Journal of Petrology. 18: 399-430.

Berg, J.H., and Wheeler, E.P. 1976. Osumilite of deep-seated origin in the contact aureole of the anorthositic Nain Complex, Labrador. American Mineralogist. 61: 29-37.

Berg, J.H., and Wiebe, R.A.1985. Petrology of a xenolith of ferro-aluminous gneiss from the Nain complex. Contributions to Mineralogy and Petrology. 90: 226-235.

Bertrand, J.M., Roddick, J.C., van Kranendonk, M.J., and Ermanovics, I. 1993. U-Pb geochronology of deformation and metamorphism across a central transect of the early Proterozoic Torngat Orogen, North River map area, Labrador. Canadian Journal of Earth Science. 30: 1470-1489.

Bridgwater, D., Watson, J. and Windley, B.F. 1973. The Archean craton of the North Atlantic region. Phil. Trans. R. Soc. London. A258: 41-51.

Brown, M. 2008. "Ch. 6: Granites, Migmatites and Residual Granulites: Relationships and Processes", *Mineralogical Association of Canada Short Course* 38, Quebec City, Quebec, 97-144.

Brown, M, White, R.W., and Sandiford, M. 2010. On the importance of minding one`s Ps and Ts: metamorphic processes and quantitative petrology. Journal of Metamorphic Geology. 28: 561-567.

Carrington, D.P, and Harley, S.L. 1995. The stability of osumilite in metapelitic granulites. Journal of Metamorphic Geology. 13: 613-625.

Cherniak, D.J., Watson, E.B. and Wark, D.A. 2007. Ti diffusion in quartz. Chemical Geology. 236: 65-74.

Droop, G.T.R. 1987. A general equation for estimating Fe^{3+} concentrations in ferromagnesion silicates and oxides from microprobe analyses, using stoichiometric criteria. Mineralogical Magazine. 51: 431-435.

Ellis, D.J., Sheraton, J.W., England, R.N., and Dallwitz, W.B. 1980. Osumilite-sapphirine-quartz granulites from Enderby Land Antarctica – Mineral assemblages and reactions. Contributions to Mineralogy and Petrology. 72: 123-143.

Emslie, R.F. 1975. Pyroxene megacrysts from anorthositic rocks: New clues to the sources and evolution of the parent magmas. Canadian Mineralogist. 13: 138-145.

Emslie, R., Hamilton, M. and Theriault, R. 1994. Petrogenesis of a Mid-Proterozoic anorthosite-mangerite-charnockite-granite (AMCG) Complex: Isotopic and chemical evidence from the Nain Plutonic Suite. Journal of Geology. 102: 539-558

Ermanovics, I.F., and van Kranendonk, M. 1998. Geology of the Archean Nain province and Paleoproterozoic Torngat orogen in a transect of the North River-Nutak map areas, Newfoundland (Labrador) and Quebec. Geological Survey of Canada. Bulletin 497: 156

Fowler, C.M.R. 2005. The Solid Earth: And introduction to Global Geophysics. 2nd edition. Cambridge University Press, Cambridge, UK.

Goldstein, J.L., Newbury, D., Joy, D., Lyman, C., Echlin, P., Lifshin, E., Sawyer, L., and Michael, J. 1981. Scanning electron microscopy and x-ray analysis. Plenum Press, Chapter 8: 435.

Grew, E.S. 1982. Osumilite in the sapphirine-quartz terrane of Enderby Land, Antarctica: implications for osumilite petrogenesis in the granulite facies. American Mineralogist. 67: 762-787.

Guilmette, C., Indares, A. and Hébert, R. 2010. High-pressure anatectic paragneisses from the Namche Barwa, Eastern Himalayan syntaxis: Textural evidence for partial melting, phase equilibria modeling and tectonic implications. Lithos. 124: 66-81.

Harley, S.L., and Thompson, P. 2004. The influence of cordierite on melting and mineral-melt equilibria in ultra-high-temperature metamorphism. Transactions of the Royal Society of Edinburgh: Earth Sciences. 95(Parts 1-2): 87-98.

Harley, S.L. 2006. The hottest crust. Goldschmidt Conference Abstracts. A230.
Holland, T.J.B., and Powell, R. 1998. An internally consistent thermodynamic data set for phases of petrological interest. Journal of Metamorphic Geology. 16: 309-343.

Holland, T.J.B., and Powell, R. 2003. Activity-composition relations for phases in petrological calculations; an asymmetric multicomponent formulation. Contributions to Mineralogy and Petrology. 145: 492-501.

Holland, T.J.B., Babu, E.V.S.S.K., and Waters, D.J. 1996. Phase relations of osumilite and dehydration melting in pelitic rocks: a simple thermodynamic model for the KFMASH system. Contributions to Mineralogy and Petrology. 124: 383-394.

Holland, T.J.B., Baker, J.M. and Powell, R. 1998. Mixing properties and activity-composition relationships of chlorites in the system MgO-FeO-A12O3-SiO2-H2O. European Journal of Mineralogy. 10: 395-406.

Holness, M.B. 2008. "Ch. 4: Decoding Migmatite Microstructures", *Mineralogical Association of Canada Short Course 38*, Quebec City, Quebec, 57-76.

Holness, M.B. and Sawyer, E.W. 2008. On the pseudomorphing of melt-filled pores during the crystallization of migmatites. Journal of Petrology. 49. 1343-1363.

Holness, M.B., Cesare, B. and Sawyer, E.W. 2011. Melted rocks under the microscope: Microstructures and their interpretation. Elements. 7: 247-252.

Indares, A., White, R. W. and Powell, R. 2008. Phase equilibria modelling of kyanite-bearing anatectic paragneisses from the central Grenville Province. Journal of Metamorphic Geology. 26: 815-836.

Jenkins, R. and Devries, J. 1970. Worked examples in x-ray analysis. Macmillan Press.

Kelsey, D.E. 2008. On ultrahigh-temperature crustal metamorphism. Gondwana Research. 13: 1-29

Kreigsman, L.M., and Alvarez-Valero, A.M. 2009. Melt-producing versus melt-consuming reactions in pelitic xenoliths and migmatites. Lithos. 116: 310-320.

Kretz, R. 1983: Symbols for rock-forming minerals. *American Mineralogist,* 68: 277-279.

Lee, D.V. 1987. Geothermobarometry and petrologic history of a contact metamorphosed section of the Tasiuyak Gneiss, west of Nain, Labrador. B.Sc. Honours thesis, Memorial University of Newfoundland, St. John's, Nfld.

McFarlane, C.R.M., Carlson, W.D., and Connelly, J.N. 2003. Prograde, peak, and retrograde P–T paths from aluminum in orthopyroxene: High-temperature contact metamorphism in the aureole of the Makhavinekh Lake Pluton, Nain Plutonic Suite, Labrador. Journal of Metamorphic Geology. 21: 405-423.

Martignole, J., and Martelat, J.E. 2003. Regional-scale Grenvillian-age UHT metamorphism in the Mollendo-Camana block (basement of the Peruvian Andes). Journal of Metamorphic Geology. 21: 99-120.

Motoyoshi, Y., Hensen, B.J. and Arima, M. 1993. Experimental study of the high-pressure stability limit of osumilite in the system K_2O-MgO-Al_2O_3-SiO_2: implications for high-temperature granulites. European Journal of Mineralogy. 5: 439-445.

O'Brien, P.J. and Roetzler, J., 2003. High-pressure granulites; formation, recovery of peak conditions and implications for tectonics. Journal of Metamorphic Geology. 21: 3–20.

Powell, R. and Holland, T. J. B., 1988. An internally consistent thermodynamic dataset with uncertainties and correlations: application, methods, worked examples and a computer program. Journal of Metamorphic Geology, 6: 173–204.

Ribe, N.M. 1987. Theory of melt segregation – A review. Journal of Volcanology and Geothermal Research. 33: 241-253.

Rivers, T., Mengel, F., Scott, D.J., Campbell, L.M., and Goulet, N. 1996. Torngat Orogen – a Paleoproterozoic example of a narrow doubly-vergent collisional orogen. *In* Precambrian crustal evolution in the North Atlantic region. *Edited by* T.S. Brewer. Geological Society (of London), Special Publication. 112: 117-136.

Robinson, B.W. 1998. "Chapter 6: Modern electron-microprobe trace-element analysis in mineralogy" *Mineralogical Association of Canada short course 27*. Ottawa, Ontario.

Ryan, B. 1991. Makhavinekh Lake Pluton, Labrador, Canada; geological setting, subdivisions, mode of emplacement, and a comparison with Finnish rapakivi granites. Precambrian Research. 54: 193-225.

Ryan, B. 2000. The Nain-Churchill Boundary and the Nain Plutonic Suite: A regional perspective on the geologic setting of the Voisey's Bay Ni-Cu-Co Deposit. Economic Geology. 95: 703-724.

Ryan, B., and Emslie, R.F. 1994. Pre-Elsonian mafic magmatism in the Nain Igneous complex, Labrador: the Bridges layered intrusion - comment. Precambrian Research. 68: 179-181.

Ryan, B. and Lee, D. 1989: Geological map of the Makhavinekh Mountain area (14D/1). Department of Mines and Energy, Geological Survey Branch, Open File, 89-17. Scale 1:50 000.

Sajeev, K. and Osanai, Y. 2004. Osumilite and spinel + quartz from Sri Lanka: Implications for UHT conditions and retrograde P-T path. Journal of Mineralogical and Petrological Sciences. 99: 320-327.

Sawyer, E.W. 1999. Criteria for the recognition of partial melting. Physics and Chemistry of the Earth. 24: 269-279

Shaw, R.K., and Arima, M. 1998. A corundum–quartz assemblage from the Eastern Ghats Granulite Belt, India: evidence for high P–T metamorphism? Journal of Metamorphic Geology. 16: 189–196.

Spear, F.S., Kohn, M.J., and Cheney, J.T. 1999. P–T paths from anatectic pelites. Contributions to Mineralogy and Petrology. 134: 17-32.

Stipska, P., Powell, R., White, R.W., and Baldwin, J.A. 2010. Using calculated chemical potential relationships to account for coronae around kyanite; an example from the Bohemian Massif. Journal of Metamorphic Geology. 28: 97-116.

Storm, L.C., and Spear, F.S. 2009. Application of the titanium-in-quartz thermometer to pelitic migmatites from the Adirondack Highlands, New York. Journal of Metamorphic Geology. 27: 479-494.

Tettelaar, T.A. 2004. Emplacement history of the Pearly Gates Anorthosite pluton and spatially related Tessiarsuyungoakh Intrusion, and metamorphic petrology of the adjacent Tasiuyak paragneiss, northern Labrador. M.Sc. thesis, Memorial University of Newfoundland, St. John's, Nfld.

Tettelaar, T., and Indares, A. 2007. Granulite-facies regional and contact metamorphism of the Tasiuyak paragneiss, northern Labrador: textural evolution and interpretation. Canadian Journal of Earth Sciences. 44: 1413-1437.

Thomas, J.B., Watson, E.B., Spear, F.S., Shemella, P.T., Nayak, S.K., and Lanzirotiti, A. 2010. TitaniQ under pressure: the effect of pressure and temperature on the solubility of Ti in quartz. Contributions to Mineralogy and Petrology. 160: 743-759.

Vernon, R.H. 2004. "Ch. 4: Microstructures of Metamorphic Rocks", *A Practical Guide to Rock Microstructure*, Cambridge University Press, 284-293.

Vernon, R.H., White, R.W., and Clarke, G.L. 2008. False metamorphic events inferred from misinterpretation of microstructural evidence and P–T data. Journal of Metamorphic Geology. 26: 437–449.

Wardle, R.J., James, D.T., Scott, D.J., and Hall, J. 2002. The southeastern Churchill Province: synthesis of a Paleoproterozoic transpressional orogen. Canadian Journal of Earth Sciences. 39: 639-663.

Wark, D.A., and Watson, B.E. 2006. Titani-Q: a titanium-in-quartz geothermometer. Contributions in Mineralogy and Petrology. 152: 743-754.

Waters, D.J. 2001. The significance of prograde and retrograde quartz-bearing intergrowth microstructures in partially melted granulite-facies rocks. Lithos, 56: 97-110.

Westphal, M., Schumacher, J.C. and Boschert, S. 2003. High-temperature metamorphism and the role of magmatic heat sources at the Rogaland Anorthosite Complex in southeaster n Norway. Journal of Petrology. 44: 1145-1162.

White, R.W., and Powell, R. 2002. Melt loss and the preservation of granulite facies mineral assemblages. Journal of Metamorphic Geology. 20: 621-632.

White, R.W., and Powell, R. 2010. Retrograde melt-residue interaction and the formation of near-anhydrous leucosomes in migmatites. Journal of Metamorphic Geology. 28: 579-597.

White, R.W., Powell, R., Holland, T.J.B., and Worley, B.A. 2000. The effect of TiO2 and Fe2O3 on metapelitic assemblages at greenschist and amphibolite facies conditions: Mineral equilibria calculations in the system K_2O-FeO-MgO-Al_2O_3-SiO_2-H_2O-TiO_2-Fe_2O_3. Journal of Metamorphic Geology. 18: 497-511.

White, R.W., Powell, R., and Clarke, G.L. 2003. Prograde metamorphic assemblage evolution during partial melting of metasedimentary rocks at low pressures: migmatites from Mt. Stafford, central Australia. Journal of Petrology. 44: 1937-1960.

White, R.W., Powell, R., and Holland, T.J.B. 2007. Progress relating to calculation of partial melting equilibria for metapelites. Journal of Metamorphic Geology. 25: 511-527.

Whitmeyer, S.J. and Karlstrom, K.E. 2007. Tectonic model for the Proterozoic growth of North America. Geosphere. 3: 220-259.

Ziebold, T. 1967. Precision and sensitivity in electron microprobe analysis. Analytical Chemistry. 39: 858-861.

APPENDIX A:

See attached DVD-RW disc for spot locations, mineral compositions data and titanium in quartz data for all sample types.